

**POLITECNICO DI MILANO**

School of Industrial and Information Engineering

Master of Science in Materials Engineering and Nanotechnology



**SCANNING TUNNELING MICROSCOPY AND  
SPECTROSCOPY OF TITANIUM OXIDE  
NANOSTRUCTURES ON THE Au(111) SURFACE**

Supervisor: Prof. Andrea Li Bassi

Co-supervisor: Dr. Paolo Carrozzo

Master Thesis of:  
Luca Mascaretti  
782005

Academic Year 2013-2014

*Solo una crescente efficacia nello spiegare consente infatti  
una crescente capacità di capire.*

(Piero Angela)

# Abstract

This thesis work reports an experimental analysis of  $\text{TiO}_x$  nanostructures and ultrathin films on the Au(111) surface by means of Scanning Tunneling Microscopy (STM) and Scanning Tunneling Spectroscopy (STS). The  $\text{TiO}_x/\text{Au}(111)$  system is obtained with the electron-beam evaporation technique at low and high coverage, namely 0.3 ML and 1.5 ML of titanium, followed by oxidation. The STM analysis shows the formation of five different  $\text{TiO}_x$  phases, in agreement with previous observations, whose structural and morphological features are discussed thanks to atomically resolved STM images and the results of Low Energy Electron Diffraction (LEED) measurements. The STS analysis, on the other hand, allows to investigate the electronic properties of the  $\text{TiO}_x$  phases and it shows their peculiar individual features around the Fermi energy. The examined system represents a model system for the study of morphological, structural and electronic properties of nanostructured  $\text{TiO}_x$  films, which, thanks to their high surface/volume ratio, are highly regarded in the research on photovoltaic and photocatalytic applications.

## Sommario

Il presente elaborato di tesi riporta un'analisi sperimentale della crescita di nanostrutture e film ultrasottili di  $\text{TiO}_x$  su Au(111) tramite microscopia a effetto tunnel (STM, *Scanning Tunneling Microscopy*) e spettroscopia a effetto tunnel (STS, *Scanning Tunneling Spectroscopy*). Il sistema  $\text{TiO}_x/\text{Au}(111)$  è stato ottenuto con la tecnica di evaporazione da fascio elettronico a basso ed alto coverage di titanio, principalmente 0.3 ML e 1.5 ML, seguita da ossidazione. L'analisi STM mostra la formazione di cinque diverse fasi di  $\text{TiO}_x$ , in accordo con le precedenti osservazioni, le cui caratteristiche strutturali e morfologiche sono discusse grazie alle immagini STM a risoluzione atomica e i risultati ottenuti dalla diffrazione elettronica a basse energie (LEED, *Low Energy Electron Diffraction*). L'analisi STS, invece, consente di investigare le proprietà elettroniche delle diverse fasi e mostra le peculiari caratteristiche di ciascuna di esse nell'intorno dell'energia di Fermi. Il sistema esaminato rappresenta un sistema modello per lo studio delle proprietà morfologiche, strutturali ed elettroniche dei film nanostrutturati di  $\text{TiO}_x$ , i quali, grazie al loro elevato rapporto superficie/volume, sono considerati di grande interesse nell'ambito della ricerca su dispositivi per applicazioni fotovoltaiche e di fotocatalisi.

# Contents

<b>Abstract</b>	<b>iii</b>
<b>Sommario</b>	<b>iv</b>
<b>Contents</b>	<b>v</b>
<b>List of Figures</b>	<b>vii</b>
<b>List of Tables</b>	<b>ix</b>
<b>List of Symbols and Acronyms</b>	<b>x</b>
<b>Introduction</b>	<b>1</b>
<b>1 Scanning tunneling microscopy and spectroscopy</b>	<b>4</b>
1.1 Scanning tunneling microscopy . . . . .	5
1.1.1 Operating principles . . . . .	5
1.1.2 Elementary theory of scanning tunneling microscopy . . . . .	6
1.1.3 Bardeen theory . . . . .	8
1.1.4 Theoretical models for STM imaging: the Tersoff-Hamann model	11
1.1.5 Theoretical models for STM imaging: the Chen model . . . . .	12
1.2 Scanning tunneling spectroscopy . . . . .	12
1.2.1 Theory of STS: the WKB approximation . . . . .	13
1.2.2 Normalization methods . . . . .	15
<b>2 Thin films of metal oxides on metallic surfaces</b>	<b>17</b>
2.1 The surface of Au(111) . . . . .	17
2.1.1 Morphology and structure . . . . .	17
2.1.2 Electronic structure . . . . .	19
2.2 Monocrystalline titanium dioxide . . . . .	20
2.2.1 Morphology and structure . . . . .	20
2.2.2 Electronic structure . . . . .	23
2.3 Fundamentals of nucleation and growth of thin films . . . . .	24
2.4 Metal oxide ultrathin films on (111) metal surfaces . . . . .	27

2.4.1	TiO <sub>x</sub> /Pt(111) . . . . .	27
2.4.2	VO <sub>x</sub> /Pd(111) . . . . .	30
2.5	Growth of TiO <sub>x</sub> /Au(111) . . . . .	32
2.6	Thesis objectives . . . . .	39
<b>3</b>	<b>Experimental results</b>	<b>41</b>
3.1	Experimental procedure . . . . .	41
3.2	Morphology and structure . . . . .	42
3.2.1	LEED analysis . . . . .	42
3.2.2	Atomic structure of TiO <sub>x</sub> phases . . . . .	44
3.2.3	Adsorbates . . . . .	54
3.2.4	Defects on the Au(111) surface . . . . .	54
3.3	Electronic properties of the TiO <sub>x</sub> /Au(111) system . . . . .	57
3.3.1	Data collection and analysis procedures . . . . .	57
3.3.2	Au(111) . . . . .	60
3.3.3	Honeycomb . . . . .	61
3.3.4	Pinwheel . . . . .	63
3.3.5	Triangular . . . . .	66
3.3.6	Row . . . . .	69
3.3.7	Final comparisons . . . . .	70
3.4	Discussion . . . . .	73
<b>4</b>	<b>Conclusions and perspectives</b>	<b>75</b>
<b>Appendix A</b>	<b>Experimental details</b>	<b>77</b>
A.1	Vacuum system . . . . .	77
A.2	STM-STS apparatus . . . . .	79
A.2.1	STM measurements . . . . .	79
A.2.2	STS measurements and lock-in amplifier . . . . .	81
A.3	Tip preparation method . . . . .	82
A.4	Surface and sample preparation facilities . . . . .	83
A.5	Low energy electron diffraction (LEED) . . . . .	85
A.6	Auger electron spectroscopy (AES) . . . . .	87
<b>Bibliography</b>		<b>88</b>
<b>Ringraziamenti</b>		<b>91</b>

# List of Figures

1	Nanostructured TiO <sub>2</sub> thin films . . . . .	2
1.1	Schematic diagram of a scanning tunneling microscope . . . . .	5
1.2	Operating modes of a scanning tunneling microscope . . . . .	6
1.3	Schematic model of the tunnel effect with monodimensional rectangular potential barrier . . . . .	7
1.4	Scheme of the energy levels involved in tunneling for a metallic sample .	10
1.5	Scheme of the energy levels involved in tunneling for a semiconductor sample . . . . .	10
1.6	Schematic picture of tunneling geometry . . . . .	11
1.7	Schematic picture of the tunneling junction in the WKB approximation	14
2.1	Model of $(22 \times \sqrt{3})$ reconstruction . . . . .	18
2.2	STM images of Au(111) from Ref. [39] . . . . .	19
2.3	$dI/dV$ curves and map of Au(111) from Ref. [42] . . . . .	20
2.4	LDOS of Au(111) calculated with the extended KP potential from Ref. [44]	21
2.5	Bulk structures of rutile and anatase . . . . .	21
2.6	STM image of anatase (101) . . . . .	22
2.7	Rutile (110) crystal structure (STM image and model) . . . . .	22
2.8	Absorption and emission spectra of TiO <sub>2</sub> (110) surfaces . . . . .	23
2.9	STS measurements on the TiO <sub>2</sub> (110) surface . . . . .	24
2.10	Atomic processes involved in film growth . . . . .	25
2.11	Schematic illustration of the basic growth modes . . . . .	26
2.12	Schematic representation of homoepitaxial and heteroepitaxial structures	26
2.13	STM images of $k$ -TiO <sub>x</sub> phase and structural model . . . . .	28
2.14	STM images and structural model of the $z$ -TiO <sub>x</sub> /Pt(111) phase . . . . .	29
2.15	STM images of $w$ -TiO <sub>x</sub> /Pt(111) phase . . . . .	29
2.16	Moiré pattern of $w$ -TiO <sub>x</sub> /Pt(111) phase . . . . .	30
2.17	STM image of low coverage VO <sub>x</sub> /Pd(111) . . . . .	31
2.18	STM images of TiO <sub>x</sub> /Au(111) from Ref. [11] . . . . .	32
2.19	STM images of TiO <sub>x</sub> /Au(111) from Ref. [10] . . . . .	33
2.20	STM image and structural models of TiO <sub>x</sub> /Au(111) from Ref. [12] . . . .	34
2.21	TiO <sub>x</sub> /Au(111) - coverage evolution from Ref. [13] . . . . .	37

2.22	Atomic resolution and structural model of pinwheel phase from Ref. [13]	38
2.23	Atomic resolution STM image of the honeycomb phase from Ref. [13]	38
2.24	STM image of a triangular island from Ref. [13]	39
2.25	High resolution STM image of the row phase from Ref. [13]	40
3.1	LEED patterns of the $\text{TiO}_x/\text{Au}(111)$ system at increasing coverage	43
3.2	Simulated LEED for the honeycomb phase	43
3.3	Simulated LEED of the pinwheel phase	44
3.4	STM images of $\text{TiO}_x/\text{Au}(111)$ at low and high coverage	45
3.5	Atomic structure of the honeycomb phase	47
3.6	Atomic structure of the pinwheel phase	49
3.7	STM images of the triangular phase	51
3.8	STM images of the row phase	52
3.9	STM images of the needle phase	53
3.10	STM images of the adsorbates on the pinwheel and honeycomb phases	55
3.11	STM images of Pd on $\text{SiO}_2$ on Mo(112) from Ref. [74]	56
3.12	STM images of defects on the Au(111) surface at low coverage	56
3.13	Example of the data collection and analysis procedures	59
3.14	STS of Au(111) at low coverage	60
3.15	STS of Au(111) at high coverage	61
3.16	STS of the honeycomb phase	62
3.17	STS of the honeycomb phase with W tip at 1.1 MLE	63
3.18	STS of the pinwheel phase at low coverage	64
3.19	STS of the pinwheel at high coverage	65
3.20	STS of the pinwheel phase at high coverage – comparison between Cr and W tips	66
3.21	STS of the triangular phase at low coverage	67
3.22	STS of the triangular phase at high coverage	68
3.23	STS of the row phase	69
3.24	STS of the row phase with W tip at 1.3 MLE	70
3.25	STS spectra of the different $\text{TiO}_x$ phases	71
A.1	STM apparatus	77
A.2	STM sample stage	79
A.3	Scheme of tip path	80
A.4	Scheme of a W tip production	82
A.5	Production of a bulk Cr tip	83
A.6	External view of the ion gun and thermal evaporator	84
A.7	Thermal evaporator	85
A.8	Mean free path of electrons in solids as a function of their energy	86
A.9	Inner view of the LEED apparatus	86
A.10	Scheme of the Auger process	87

# List of Tables

2.1	Summary of the $\text{TiO}_x$ phases on Pt(111) . . . . .	31
3.1	Summary of the structural analysis on the $\text{TiO}_x/\text{Au}(111)$ phases . . . . .	53
3.2	Summary of the STS data on the $\text{TiO}_x/\text{Au}(111)$ phases . . . . .	72

# List of Symbols and Acronyms

AFM	atomic force microscopy
ALD	atomic layer deposition
AES	Auger electron spectroscopy
CVD	chemical vapor deposition
$\Delta$	energy amplitude between the two main peaks around the Fermi energy
DFT	density functional theory
DOS	density of states
$E_c$	bottom of the conduction band
$E_F$	Fermi energy
$E_g$	energy gap
FCC	face-centered cubic
HCP	hexagonal close-packed
HAS	helium atom scattering
LEED	low-energy electron diffraction
LDOS	local density of states
MFM	magnetic force microscopy
MBE	molecular beam epitaxy

$n$	number of single spectra by which a STS curve is made up
$o_x$	peak in the occupied states for the phase $x$
$o_h$	peak in the occupied states for the honeycomb phase
$o_r$	peak in the occupied states for the row phase
$o_p$	peak in the occupied states for the pinwheel phase
$o_t$	peak in the occupied states for the triangular phase
PVD	physical vapor deposition
PLD	pulsed laser deposition
RLAD	reactive-layer-assisted deposition
RT	room temperature
SEM	scanning electron microscope
SNOM	scanning near-field optical microscopy
SPM	scanning probe microscopy
STM	scanning tunneling microscopy
STS	scanning tunneling spectroscopy
SP-STM	spin-polarized scanning tunneling microscopy
SP-STs	spin-polarized scanning tunneling spectroscopy
UHV	ultra-high vacuum
$u_x$	peak in the unoccupied states for the phase $x$
$u_h$	peak in the unoccupied states for the honeycomb phase
$u_p$	peak in the unoccupied states for the pinwheel phase
$u_r$	peak in the unoccupied states for the row phase
$u_t$	peak in the unoccupied states for the triangular phase
WKB	Wentzel-Kramers-Brillouin
XPD	X-ray photoelectron diffraction
XPS	X-ray photoelectron spectroscopy

# Introduction

The main topic of the thesis work presented here deals with the study of titanium oxide nanostructures and ultrathin films, grown on the Au(111) surface, by means of scanning tunneling microscopy (STM) and scanning tunneling spectroscopy (STS). The titanium deposition on the gold substrate is performed by electron-beam evaporation, followed by oxidation in order to obtain titanium oxide. The analysis is aimed to extend the basic knowledge of titanium oxide surfaces and nanostructures, mainly focusing on their structural and electronic properties at the nanoscale.

Titanium dioxide (titania) is one of the most relevant strategic materials in many technological applications; some examples are heterogeneous catalysis<sup>[1]</sup>, photo-assisted oxidation<sup>[2]</sup>, optical<sup>[3]</sup> and photovoltaic<sup>[4]</sup> devices, self-cleaning surfaces and water splitting<sup>[5]</sup>. Nanostructured TiO<sub>2</sub>, in addition, such as in the form of ultrathin supported films<sup>[6]</sup>, nanoparticles<sup>[1]</sup> and hierarchical nanostructures<sup>[7]</sup>, exhibits surface-mediated structural, chemical and electronic properties different from their bulk counterparts. As an example, Figure 1 shows two examples of scanning electron microscope (SEM) images of nanostructured TiO<sub>2</sub> films, which can be applied as photoanodes in the so-called dye-sensitized solar cells (DSSC). Their high surface/volume ratio, indeed, provides an outstanding surface area available for the adhesion with photosensible molecules (*dye*), producing an efficiency increase of the device.

On the other hand, a growing interest is recently developing in oxide ultrathin films on metals, since their properties are determined by the combination of the ones of both the substrate and the overlayer; for example, they may find application as templates for cluster growth, molecular sieves, promoters of the activation of supported particles on specific defects and for the formation of charged clusters on their surface<sup>[8]</sup>.

These examples illustrate the importance of a deep knowledge of structural and electronic properties, with high spatial resolution, of nanostructured TiO<sub>2</sub> films. This purpose can be achieved by realizing and characterizing the so-called *model systems*, in which titanium oxide clusters or thin films are deposited onto a suitable surface. Indeed, although monocrystalline TiO<sub>2</sub> is one of the most studied systems in the whole surface science<sup>[9]</sup>, only few research works concerns the study of titanium oxide 2D nanostructures, which, generally speaking, exhibit different properties from the same

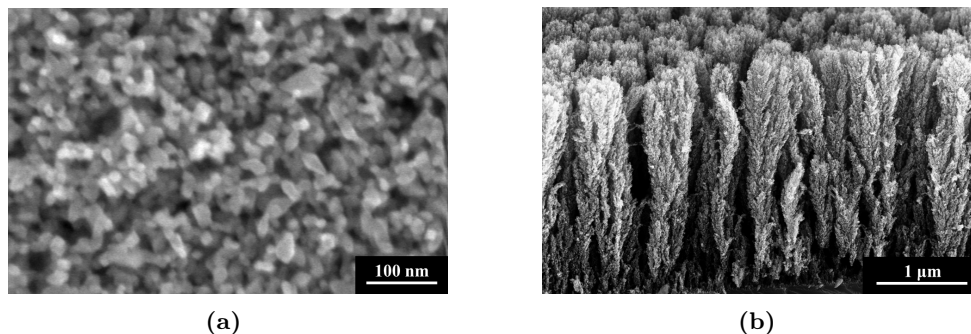


**Figure 1:** (a) SEM image of a mesoporous  $\text{TiO}_2$  film<sup>[4]</sup>. (b) SEM image of hierarchical  $\text{TiO}_2$  nanostructures obtained with pulsed laser deposition (PLD)<sup>[7]</sup>.

bulk material, due to the confinement in size and the interaction with the substrate.

As a model substrate surface for this kind of study, the Au(111) one represents a suitable choice, since it is well-known in surface science, it is chemically inert towards oxygen and it shows a peculiar surface reconstruction, known as *herringbone reconstruction*, which can provide preferential sites for the nucleation of clusters<sup>[10]</sup> and, thus, can act as a template. These features demonstrate the Au(111) significance as a substrate for the growth of metal oxide nanostructures.

In order to study the physical properties of the aforementioned titanium oxide nanostructures, the STM and STS techniques appear as suitable choices thanks to their remarkable spatial resolution, which is mandatory for a study at the nanoscale of surfaces. Indeed, the invention of scanning tunneling microscope represents a milestone in the experimental study of metallic and semiconductive surfaces and it is presently employed in several studies in the extended field of nanotechnology.

For all the aforementioned reasons, this thesis work aims to realize and characterize titanium oxide nanostructures on the Au(111) surface by means of STM and STS techniques, studying their evolution with an increasing coverage. This kind of analysis is reported in few papers<sup>[10-12]</sup> and, indeed, it has been undertaken in a previous thesis work<sup>[13]</sup>, which concerned mainly the morphological characterization of  $\text{TiO}_x/\text{Au}(111)$  phases; in addition, it also discussed the morphological and electronic properties of the Ti/Au(111) system. For this reason, the present work is focused on the electronic properties of the  $\text{TiO}_x$  phases, which had not been investigated previously. This thesis is divided into four chapters and an appendix:

- **Chapter 1 – Scanning tunneling microscopy and spectroscopy:** the STM and STS techniques are introduced. First, the basic principles of STM are described, followed by theoretical models on the tunneling phenomenon; afterwards, the STS technique is described and, also in this case, the most relevant theoretical models are highlighted, as well as the main normalization methods.
- **Chapter 2 – Thin films of metal oxides on metallic surfaces:** some relevant examples of metal oxides thin films on metallic surfaces are highlighted. The chapter opens with a description of the Au(111) surface, followed by a highlight on the properties of monocrystalline titanium dioxide; thereafter, the growth of metal oxide ultrathin films on metallic surfaces is considered; afterwards, the state

---

of the art of the study on  $\text{TiO}_x/\text{Au}(111)$  system is reviewed in more detail and, eventually, the thesis objectives are more specifically clarified.

- **Chapter 3 – Experimental results:** the results obtained in this work are illustrated and discussed. In the first section, the morphological and structural properties are considered, whereas in the second one the electronic properties are described.
- **Chapter 4 – Conclusion and perspectives:** the main results are resumed, in regard to the preset goals; in addition, future perspectives of this thesis work are outlined.
- **Appendix A – Experimental details:** the experimental techniques and facilities employed in this thesis activity are explained in detail.

The STM and STS measurements on the  $\text{TiO}_x/\text{Au}(111)$  have been performed and analyzed in the Micro and Nanostructured Materials Laboratory (Nanolab) of Politecnico di Milano. I personally worked on all these activities, with the exception of the analysis of STS data at low coverage, which I partially contributed to. Low-energy electron diffraction (LEED) measurements have also been performed in the same laboratory and they are presented in this document, although I did not personally worked on them; the reason of that will be conveniently clarified.

# Scanning tunneling microscopy and spectroscopy

Surface science takes advantage of several instruments in order to unveil the physical and chemical properties of surfaces, such as the stylus, optical and electron microscopes, *et cetera*. However, the interest in an atomic-scale knowledge on surfaces led to the invention of the Scanning Tunneling Microscope (STM) in 1982 by Binnig *et al.*<sup>[14]</sup>, which represents the “progenitor” of the family of scanning probe microscopy (SPM) techniques. These techniques are generally based on the interaction between a very sharp tip and the sample surface, where the former scans the latter similarly as the stylus, but they are able to provide information about its local properties at the atomic scale. Depending on the kind of interaction between probe and sample, different techniques have developed, apart from STM, such as atomic force microscopy (AFM), magnetic force microscopy (MFM) and scanning near-field optical microscopy (SNOM). On the other hand, spectroscopic measurements have also been implemented to the scanning tunneling microscope, giving rise to the scanning tunneling spectroscopy (STS) technique, which is able to provide information about the local density of states (LDOS) of the sample. Today STM and STS techniques are employed in many research facilities and they can be crucial for the most advanced studies on the surfaces of materials and nanotechnology, mainly thanks to their outstanding spatial resolution.

In this chapter the fundamentals of STM and STS techniques will be discussed. First, the STM technique is described (Section 1.1), starting with its operating principles (Sub-section 1.1.1) and considering different theoretical models for the tunneling phenomenon (Sub-sections 1.1.2 to 1.1.5); second, the STS technique is highlighted (Section 1.2), considering the so-called WKB approximation (Sub-section 1.2.1) and the normalization methods (Sub-section 1.2.2).

## 1.1 Scanning tunneling microscopy

### 1.1.1 Operating principles

The basic principle and operation of an STM is conceptually rather simple, as illustrated in Figure 1.1: a sharp metal tip, typically made of W or Pt-Ir, is brought in close proximity ( $5\text{--}7\text{ \AA}$ ) to the sample surface. At this separation length, an overlap occurs between tip and sample wave functions, decaying exponentially into the junction gap. The most widely used convention of the polarity of bias voltage is that the tip is virtually grounded, so that  $V_b$  is the sample voltage. Thanks to the quantum mechanical effect of tunneling, a small current within the nanoampere range, called tunneling current ( $I_t$ ), arises; if  $V_b > 0$ , the electrons tunnel from the occupied states of the tip into the empty states of the sample, while if  $V_b < 0$  electrons flow from the occupied states of the sample into the unoccupied states of the tip. In the simplest design of the STM, a tip is raster-scanned across the surface, for example using three orthogonal piezoelectric transducers, as shown in Fig. 1.1. Since the tunneling current  $I_t$  depends exponentially on the distance  $z$  between the tip and the surface, current variations are detected as the tip is scanned across the corrugated surface. In particular, the tunneling current tends to increase (decrease) as the separation between the tip and the sample decreases (increases).

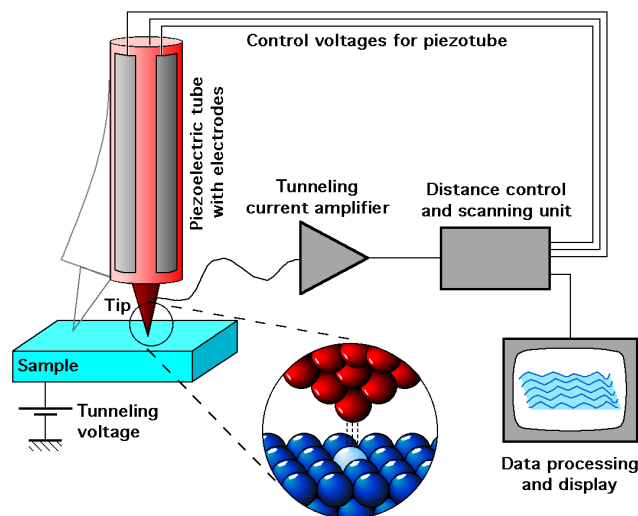


**Figure 1.1:** Schematic diagram of a scanning tunneling microscope<sup>[15]</sup>.

Normally, the STM is operated in the constant-current mode (Fig. 1.2(a)), in which the measured  $I_t$  is compared with a preset constant value  $I_0$ , typically  $0.1\text{--}10\text{ nA}$ , in a feedback circuit. The feedback signal, proportional to the difference between  $I_t$  and  $I_0$ , provides a correction to the  $z$  transducer and thus causes the distance  $z$  between the tip and the surface to change when an atom or, in more general terms, a protrusion is traversed. Recording the feedback signal or  $z$  displacement as a function of the lateral tip position during raster scanning yields a  $xy$  map of the surface topography. On the contrary, in constant height mode (Fig. 1.2(b)) the feedback circuit is turned off and the tip-sample distance  $z$  is kept constant; in this case, the tunneling current signal as a function of the  $(x, y)$  position of the tip is acquired and imaged. The constant height STM image, thus, represents the trend of the  $I_t(x, y)$  function on the analyzed surface

for a given bias  $V_b$ . In this way, a faster acquisition is achievable, but the images are less suitable to a quantitative analysis of the sample's morphological features.

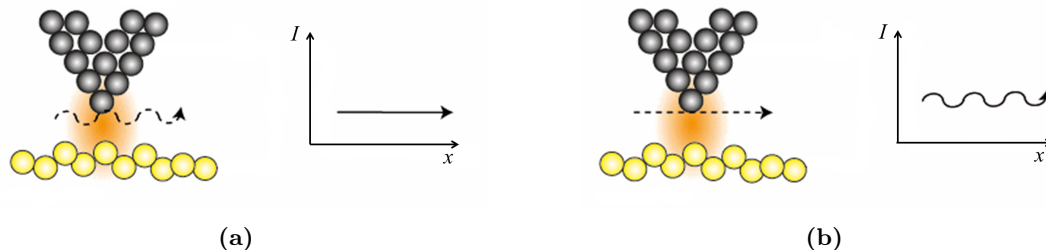


**Figure 1.2:** Operating modes of a scanning tunneling microscope. (a) Constant current mode. (b) Constant height mode.

Since the tunneling current behaves exponentially with  $z$  (see Section 1.1.2, Eq. (1.8)), the interaction area of the tip is limited to a few atoms of the tip apex, thus providing a nano-sized probe by which atomically resolved images of a surface can be obtained. The mechanical design of an STM has the inherent complication that the tip-to-sample distance has to be stabilized on a sub-Ångstrom scale by construction elements with dimensions in the centimeter range<sup>[16]</sup>. This mismatch over nine orders of magnitude is a major difficulty since construction elements such as tip, scan unit, sample, sample holder and interconnecting base systems are affected by vibrations and thermal drift. In particular, to achieve atomic resolution, vibration isolation is essential. This can be achieved by making the STM unit as rigid as possible and by reducing the influence of environmental vibrations by decoupling the STM units from the other parts of the instrument.

As a final remark, during STM measurements the condition of ultra-high vacuum (UHV) is usually preferred, since it prevents the contamination of the sample surface by gases or other impurities (for a deeper explanation, see Appendix A.1); however, STM measurements can also be performed in air, water and various other liquid or gas ambients<sup>[17]</sup>.

### 1.1.2 Elementary theory of scanning tunneling microscopy

From the theoretical point of view, the problem of quantum tunneling can be approached in different ways. Some of them are based on single-particle models, where the potential barrier is described by a function  $U(\mathbf{r})$ . The tunneling current, then, is calculated by applying the current density operator to the solutions of the Schrödinger equation for the stationary states of the system in consideration. In this framework, one of the simplest models is the monodimensional rectangular potential barrier, as illustrated in Figure 1.3.

The potential barrier is described as

$$U(z) = \begin{cases} U_0 & \text{if } z \in (0, z_0) \\ 0 & \text{elsewhere} \end{cases} \quad (1.1)$$

On the other hand, the electron, with wave function  $\psi(z)$ , must obey the Schrödinger equation. If one is interested in a complete description of the tunneling phenomenon,

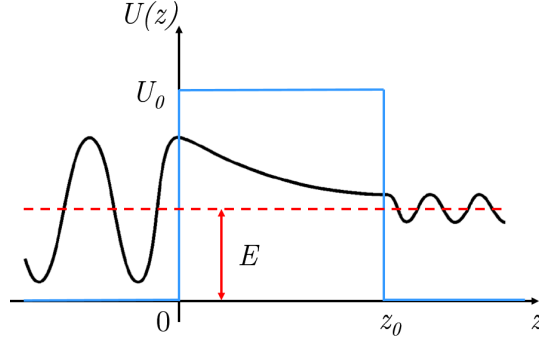


**Figure 1.3:** Schematic model of the tunnel effect with monodimensional rectangular potential barrier. The depicted oscillating function represents the real part of the wave function of an electron with energy  $E$ , which passes through the barrier (having width  $z_0$  and height  $U_0$ ).

a time-dependent treatment should be performed, since tunneling is a non-stationary quantum phenomenon; however, this kind of dissertation is not needed in order to find the transmission and reflection probabilities, so that the Schrödinger equation for the stationary states can be considered:

$$\left[ -\frac{\hbar^2}{2m} \frac{d^2}{dz^2} + U(z) \right] \psi(z) = E\psi(z) \quad (1.2)$$

where  $E$  is the total energy of the electron. Henceforth we consider the case  $E < U_0$ , that is to say, the electron has a lower energy than the potential barrier (which means that it would be anyhow classically reflected); in this case, the solution of the Schrödinger equation can be written as

$$\psi(z) = \begin{cases} A_1 e^{ik_1 z} + B_1 e^{-ik_1 z} & \text{if } z < 0 \\ A_2 e^{-k_2 z} + B_2 e^{k_2 z} & \text{if } z \in (0, z_0) \\ A_3 e^{ik_1 z} + B_3 e^{-ik_1 z} & \text{if } z > z_0 \end{cases} \quad (1.3)$$

where:

$$k_1 = \sqrt{\frac{2mE}{\hbar^2}} \quad (1.4)$$

$$k_2 = \sqrt{\frac{2m(U_0 - E)}{\hbar^2}} \quad (1.5)$$

Considering the example depicted in Fig. 1.3, where the electron reaches the barrier from the left, the transmitted wave in the region  $z > z_0$  propagates along the positive  $z$  direction, so that  $B_3$  can be set equal to zero ( $B_3 = 0$ ). The boundary conditions of the problem under consideration are the continuity of the wave function  $\psi(z)$  and of its first derivative in the  $z = 0$  and  $z = z_0$  points. By applying them, one can express the constants in Equation (1.3) by means of the incident wave amplitude  $A_1$ ; finally, by applying the current density operator to the wave function  $\psi(z)$ , the current density can be calculated with the following expression:

$$\mathbf{J} = \frac{i\hbar e}{2m} (\psi^* \nabla \psi - \psi \nabla \psi^*) \quad (1.6)$$

Therefore, the transmission coefficient  $T$  can be obtained, which is the ratio between the incident current and the transmitted one; in the approximation  $k_2 z_0 \gg 1$ , which means that the barrier is relatively “large” (i.e. several nanometers), the transmission coefficient can be written as

$$T \approx 16 \frac{k_1^2 k_2^2}{(k_1^2 + k_2^2)^2} e^{-2k_2 z_0} \quad (1.7)$$

and this equation can be rewritten using (1.4) and (1.5), obtaining

$$T \approx \frac{16E(U_0 - E)}{U_0^2} e^{-2k_2 z_0} \quad (1.8)$$

As evident, the transmission coefficient is proportional to  $e^{-2k_2 z_0}$ , which contains the electron energy ( $E$ ) and the height of the potential barrier ( $U_0$ ), both through the constant  $k_2$ , and the width of the potential barrier ( $z_0$ ). As already mentioned, the exponential dependence on  $z_0$  is the main reason of the extreme vertical resolution of STM measurements.

As illustrated by this simple example, tunneling phenomenon is described in terms of the eigenstates of the system; this represents one of the limits of the single particle stationary models, since they do not allow to describe the tunnel effect in terms of transitions between the tip electron states and sample electron states. Consequently, employing this kind of formalism, it is not possible to show the tunneling current dependence on the sample electronic features, which in turn is one of the main purposes of a theoretical model to interpret STM/STS measurements.

### 1.1.3 Bardeen theory

Bardeen theory<sup>[18]</sup> allows to describe the tunnel effect in terms of transitions between the electron states of the two electrodes, using the so-called *transfer Hamiltonian* (TH) formalism, based on time dependent perturbation theory. In this model, the tunneling interaction between the two sub-systems (tip and sample) is represented as a perturbation of the unperturbed system, which is made of the two isolated sub-systems. In mathematical terms, the Hamiltonian operator of the unperturbed system can be written as the sum between the two Hamiltonians corresponding to the isolated sub-systems:

$$\hat{H}_0 = \hat{H}_s + \hat{H}_t \quad (1.9)$$

where  $\hat{H}_s$  is the sample Hamiltonian operator and  $\hat{H}_t$  the tip one. Approaching the tip to the sample, tunnel effect arises and the Hamiltonian operator of the overall system is:

$$\hat{H} = \hat{H}_0 + \hat{H}' \quad (1.10)$$

where  $\hat{H}'$  is the perturbed Hamiltonian operator (also called perturbation operator) which represents the interaction between the two sub-systems. In the approximation of “small” perturbation, the first order time dependent perturbation theory can be applied. In this framework, the transition probability per unit time between the eigenstates of the unperturbed system is given by the Fermi golden rule:

$$\tilde{P}_{a,b} = \frac{2\pi}{\hbar} |M_{a,b}|^2 \delta(E_a - E_b) \quad (1.11)$$

where  $E_a$  and  $E_b$  are respectively the energies of the tip and sample states involved in the transition, while  $M_{a,b}$  is the matrix element of the perturbation operator, defined as

$$M_{a,b} = \langle b | \hat{H}' | a \rangle \quad (1.12)$$

Even though the Bardeen model can be treated in a more general way, using many-particle states, in this dissertation, for the sake of simplicity, the transfer Hamiltonian formalism will be applied to single-particle states. This approximation has been employed in several important literature papers<sup>[19–22]</sup>. The fundamental hypothesis which allows to describe the problem in terms of single-particle states is that electrons can be considered as independent particles. Hereinafter, not only the electron-electron interactions will be neglected, but also the spin coordinate; however, it should be noted that this approximation is not permitted if this model must be applied to spin-polarized scanning tunneling microscopy (SP-STM) or spin-polarized scanning tunneling spectroscopy (SP-SSTS), where the electron spin plays a fundamental role. In addition, in order to obtain an explicit expression of the matrix element in Eq. (1.12), the so-called *exact separability* hypothesis is applied: if one supposes to split the system into two regions  $\Omega_t$  and  $\Omega_s$ , including respectively the tip and the sample, we assume that the eigenstates of the overall system correspond to the single-particle eigenstates of the isolated tip into  $\Omega_t$  and the ones of the isolated sample into  $\Omega_s$ . This hypothesis allows to find an expression for the matrix element of the perturbation operator without defining it explicitly. The result which is obtained, in the case of transitions from the sample to the tip, is given by

$$M_{\nu,\mu} = -\frac{\hbar^2}{2m} \int_{\Sigma} (\phi_{\mu}^* \nabla \psi_{\nu} - \psi_{\nu} \nabla \phi_{\mu}^*) \cdot \mathbf{n} d\sigma \quad (1.13)$$

where  $\psi_{\nu}$  is a state of the sample,  $\phi_{\mu}$  is a state of the tip and  $\Sigma$  is an arbitrary surface into the barrier separating the two regions  $\Omega_s$  and  $\Omega_t$ . Considering tip-to-sample transitions, the matrix element  $M_{\mu,\nu}$  can be obtained exchanging  $\phi_{\mu}$  with  $\psi_{\nu}$  in (1.13). Substituting the expression (1.13) in Eq. (1.11), the tunneling current can be calculated by summing over all the possible electron states transitions from the tip to the sample, accounting for their occupancy probability, given by the Fermi-Dirac distribution. In addition, if a voltage bias  $V$  is applied between the tip and the sample (conventionally,  $V > 0$  if the sample is positively biased with respect to the tip), the net tunneling current, if  $k_B T \ll eV$ , is given by the following expression:

$$I = \frac{4\pi e}{\hbar} \int_0^{eV} \sum_{\mu,\nu} |M_{\mu,\nu}|^2 \delta(E_{\nu} - E) \delta(E_{\mu} + eV - E) dE \quad (1.14)$$

In this approximation the Fermi-Dirac distribution functions can be approximated with Heaviside functions. It should be noted that the tunneling current depends, through the matrix element  $M_{\mu,\nu}$ , on the involved electron states and that, thanks to the Pauli exclusion principle, these states are included into the energy interval from 0 to  $eV$ , where 0 is chosen as sample Fermi level. This situation is schematically illustrated in Figure 1.4: the sample is positively biased with respect to the tip and electrons make a transition from the tip occupied states to the sample empty states, within the energy interval  $(0, eV)$ . On the other hand, if the applied bias is negative, electrons move from the sample occupied states to the tip empty states.

It should be noted that the schematic drawing in Fig. 1.12 illustrates the particular case in which the sample is a metal. However, STM technique allows to study also the

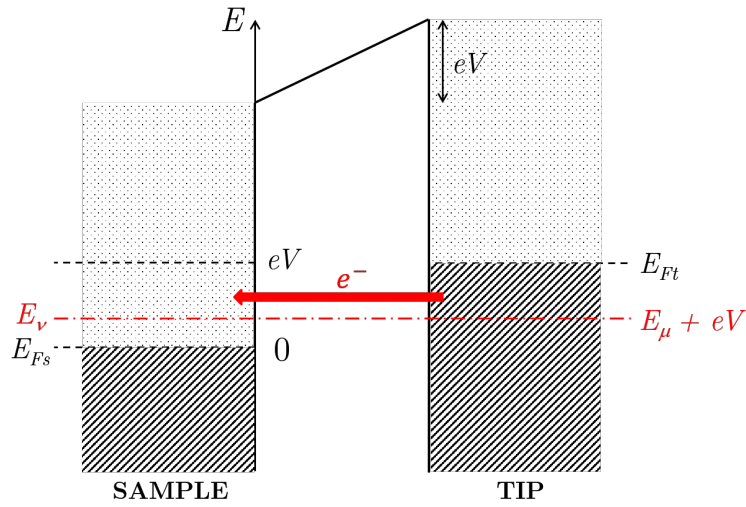


**Figure 1.4:** Scheme of the energy levels involved in tunneling between the tip and the sample. The sample is positively biased with respect to the tip and electrons perform a transition from the tip occupied states to the sample empty states within the energy interval  $(0, eV)$ .

semiconductor surfaces, such as silicon or some metal oxides. In this case, a schematic picture of the energy levels involved in the tunneling phenomenon must take into account the energy gap exhibited by the semiconductor material between the valence band and the conduction band. This is illustrated in Figure 1.13; since a forbidden energy region is present, in which no available states for tunneling are present, one can more easily understand the importance of the applied voltage in order to arise the tunneling current. Moreover, this suggests the bias dependence of the STM imaging, which, indeed, is one of the major factor to be taken into account in the interpretation of the STM measurements.

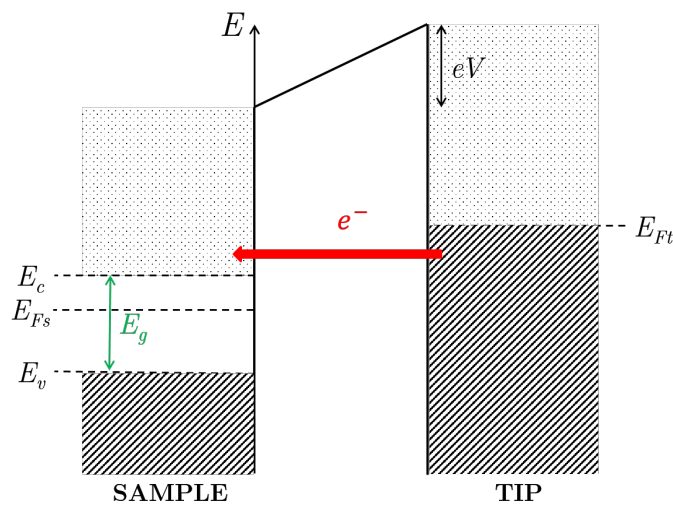


**Figure 1.5:** Scheme of the energy levels involved in tunneling for a semiconductor sample. The positive applied bias is high enough to let electrons pass from the tip occupied states to the empty states in the conduction band of the sample.

### 1.1.4 Theoretical models for STM imaging: the Tersoff-Hamann model

The first interpretative model for STM measurements was developed by Tersoff and Hamann<sup>[19,20]</sup> and it makes use of the transfer Hamiltonian perturbative approach. Referring to Figure 1.6, the Tersoff-Hamann model assumes that the tip apex has a local spherical shape and that, as a consequence, only  $s$ -symmetrical tip wave functions are considered to take part into the tunneling process. The matrix element in Eq. (1.13), thus, is calculated for a generic sample state  $\psi_\nu$  making use, as a tip state, of a wave function of the form

$$\phi_\mu(\mathbf{r}) \propto \frac{e^{-k_t|\mathbf{r}-\mathbf{r}_0|}}{k_t|\mathbf{r}-\mathbf{r}_0|} \quad (1.15)$$

where  $\mathbf{r}_0$  is the center of curvature of the tip and  $1/k_t$  is the decay length of the wave function. In the limit of low temperature and low applied bias, the expression for the tunneling current in Eq. (1.14) can be approximated as

$$I \approx \frac{4\pi e^2 V}{\hbar} \sum_{\mu,\nu} |M_{\mu,\nu}|^2 \delta(E_\nu - E_F) \delta(E_\mu - E_F) \quad (1.16)$$

where  $E_F$  is the sample Fermi energy, which can be set as equal to the tip's in this approximation. Substituting in Eq. (1.16) the matrix element calculated for  $s$  wave functions, the following result is obtained<sup>[19]</sup>:

$$I \propto V \rho_t(E_F) \rho_s(E_F, \mathbf{r}_0) \quad (1.17)$$

where  $\rho_t(E_F) = \sum_\mu \delta(E_\mu - E_F)$  is the tip density of states at the Fermi energy. The quantity

$$\rho_s(E_F, \mathbf{r}_0) = \sum_\nu |\psi_\nu(\mathbf{r}_0)|^2 \delta(E_\nu - E_F) \quad (1.18)$$

is the local density of states (LDOS) of the sample at the Fermi energy and in correspondance of the center of curvature. Hence, according to the Tersoff-Hamann model, STM images acquired at low bias and constant current represent the surface level of the sample LDOS at the Fermi energy.

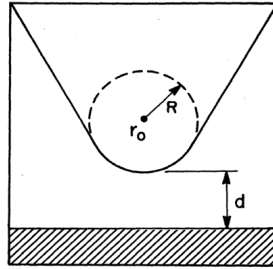


**Figure 1.6:** Schematic picture of tunneling geometry. Probe tip has an arbitrary shape but it is assumed locally spherical with radius of curvature  $R$ , where it approaches nearest the surface (shaded). Distance of nearest approach is  $d$ . The tip center of curvature is labeled as  $\mathbf{r}_0$ <sup>[19]</sup>.

Nevertheless, the Tersoff-Hamann model is unable to explain the atomic resolution (2.5–3 Å) obtained in STM observations of highly packed metallic surfaces. Indeed, approximating the tip with a  $s$  spherical symmetry waveform, the spatial resolution expected on metallic surfaces is greater than 6 Å<sup>[20]</sup>.

### 1.1.5 Theoretical models for STM imaging: the Chen model

Typical STM tips are realized using transition metals, such as tungsten (W). Ohnishi and Tsukada<sup>[23,24]</sup> showed that a real W-tip, ending with a single W-atom, will have a  $d_{z^2}$ -like electron state at its apex atom, located energetically just below the Fermi level of the tip. The level is expected to have a band-width in the order of 1 eV<sup>[25]</sup>. Doyen *et al.*<sup>[26]</sup> showed that such a  $d$ -type state can also exist at the Fermi level, rather just below it. This means that for W tips with a single atom at the apex, the tip LDOS near the Fermi level is dominated by a  $d$ -like state protruding from the apex. If the energy band associated with the tip state crosses the Fermi level of the tip, the  $d$ -like state is important for both empty and filled states imaging.

In order to take into account these effects, Chen<sup>[21,22]</sup> proposed a model of tunneling that consider also tip wave function with angular moment  $l \neq 0$ . Developing the tip wave functions in spherical harmonics, it is possible to write the matrix element  $M_{\nu\mu}$  of Eq. (1.13) for the case of wave functions with the axial symmetry of the tip ( $s$ ,  $p_z$  and  $d_{z^2}$ ):

$$M_{s,\nu} \propto \frac{1}{k_t} \psi_\nu(\mathbf{r}_0) \quad (1.19)$$

$$M_{p_z,\nu} \propto \frac{1}{k_t} \frac{\partial}{\partial z} \psi_\nu(\mathbf{r}_0) \quad (1.20)$$

$$M_{d_{z^2},\nu} \propto \frac{1}{k_t} \left[ \frac{\partial^2}{\partial z^2} - \frac{1}{3} k_s^2 \right] \psi_\nu(\mathbf{r}_0) \quad (1.21)$$

where  $k_s$  and  $k_t$  are the sample and tip inverse decay lengths respectively.

This formulation provides the so-called *derivative rule*:  $M_{\nu\mu}$  is proportional to the first derivative of the sample wave function for a  $p_z$  tip state, and to the second derivative for a  $d_{z^2}$  state, both calculated in the center of curvature of the tip. In general, if the tip-state is predominantly  $p$ - or  $d$ -like, the tunnel matrix element is no longer proportional to  $|\psi_\nu(\mathbf{r}_0)|^2$ . Rather, it becomes proportional to one of the spatial derivatives of  $\psi_\nu(\mathbf{r}_0)$  for  $p_x$ ,  $p_y$  or  $p_z$  states, or to second derivatives of  $\psi_\nu(\mathbf{r}_0)$  for  $d$ -like states<sup>[17]</sup>. This can have several effects on atomically resolved images, including an enhancement of atomic corrugation or an inversion of contrast<sup>[17]</sup>. Therefore, compared to the Tersoff-Hamann theory, the Chen model is instead capable to correctly explain the origin of atomic resolution in closed packed metals<sup>[21]</sup>, thus revealing as a more adequate scheme for interpreting STM constant current imaging experiments.

## 1.2 Scanning tunneling spectroscopy

With an STM it is also possible to perform a surface electron spectroscopy by analyzing the behavior of the tunneling current with respect to the applied voltage. More precisely, the signal that carries the most direct information connected to the sample LDOS is the differential conductivity,  $dI/dV$ . With the aim of acquiring such signal, two possible modes are available, namely *point spectroscopy* and *dI/dV maps*. In the former, the feedback loop is interrupted on a specific surface location to keep the tunneling gap constant and a voltage ramp to the tunneling junction is applied as a function of bias (usually the voltage ramp is symmetrical with respect to zero). In this way, the tunneling current  $I$  is acquired as a function of  $V$ . Its derivative with respect to  $V$  can be

numerically calculated or acquired by means of a *lock-in* amplifier. In the latter, the  $dI/dV$  signal is acquired (again with a lock-in amplifier) while the tip is scanning onto the surface in constant current mode. In this way, differential conductance  $xy$  maps ( $dI/dV$  maps) at the imposed bias  $V_b$  are obtained. The theoretical details of these two methods will be described in this section; on the other hand, more information regarding the working function of the lock-in amplifier is reported in Appendix A.2.2.

### 1.2.1 Theory of STS: the WKB approximation

In Section 1.1, two theories have been presented for the interpretation of the constant current images. However, both those theories are valid within the low bias approximation and are, therefore, inadequate to describe the tunneling spectroscopy, where a finite bias is applied instead. Analyzing the Tersoff-Hamann theory, we notice that the applied bias voltage enters in Eq. (1.16) through the summation of states which can contribute to the tunneling current. Additionally, a finite bias can lead to a distortion of the tip and the sample surface wave functions, as well as to a modification of the energy eigenvalues. The derivation of the perturbed wave functions and eigenvalues is, however, a quite problematic issue. Therefore, as a first approximation, undistorted zero-voltage wave functions are usually taken. Instead, the effects of the applied bias  $V$  can be easily taken into account considering the shifting of the Fermi level of the tip and the sample of a quantity  $eV$  and by the distortion of the potential barrier inside the vacuum gap. The simplest description of the tunneling at finite bias is obtained considering Eq. (1.16) in the continuum limit, so that:

$$I = \frac{4\pi e}{\hbar} \int_0^{eV} \sum_{\mu} \delta(E_{\mu} - E + eV) \sum_{\nu} |M_{\mu,\nu}|^2 \delta(E_{\nu} - E) dE \quad (1.22)$$

where the convention of assuming  $E_F = 0$  is made. The simplest possibility to treat Eq. (1.22) is to consider the problem of tunneling in a one dimensional geometry. In such way, no distinctions hold between the concept of density of states (DOS) and local density of states (LDOS). Nevertheless, a treatment for the matrix element  $M_{\mu,\nu}$  is necessary. One of the most successful approach is obtained through the application of the Wentzel-Kramers-Brillouin (WKB) approximation, in which the electrons are considered as semi-classical particles. The probability of tunneling is therefore described by:

$$T(E, V, z_0) = \exp \left\{ -\frac{2}{\hbar} \int_0^{z_0} \sqrt{2m[U(z) - E]} dz \right\} \quad (1.23)$$

where the interval  $(0, z_0)$  delimits the barrier region (tip-sample distance) and  $T(E, V, z_0)$  is the transmission coefficient of the vacuum gap that depends on the shape of the potential barrier  $U(z)$  inside the gap. To evaluate the integral in Equation (1.23), in the scheme of the Figure 1.7, the linear trend of the potential barrier is substituted by a constant value equal to  $\Phi + eV/2$ , where  $\Phi$  is an average of the sample and tip work functions (effective work function). We therefore obtain:

$$T(E, V, z_0) = \exp \left[ -\frac{2z_0}{\hbar} \sqrt{2m \left( \Phi + \frac{eV}{2} - E \right)} \right] \quad (1.24)$$

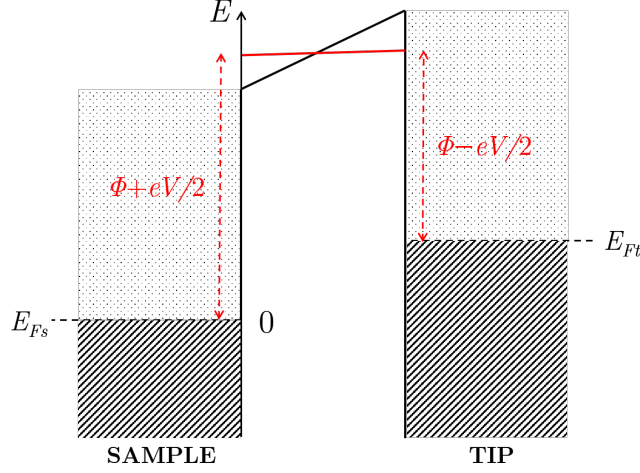


**Figure 1.7:** Schematic picture of the tunneling junction in the WKB approximation: the potential barrier is approximated as an effective rectangular one, with constant height  $\Phi + eV/2$ , where  $\Phi$  is the average work function between the tip and the sample.

In this way, a direct relation between the tunneling current and the LDOSs of the tip ( $\rho_t$ ) and the sample ( $\rho_s$ ) is obtained<sup>[27,28]</sup>:

$$I = A \int_0^{eV} T(E, V, z_0) \rho_s(E) \rho_t(E - eV) dE \quad (1.25)$$

where  $A$  is a proportionality dimensional coefficient which includes the numerical constants and the tip-sample interaction area.

From Equation (1.25) it is possible to obtain an expression for the differential conductivity  $dI/dV$ , which is, together with  $I(V)$ , the other quantity measured in STS experiments:

$$\frac{dI}{d(eV)} = A \left\{ T(eV, V, z_0) \rho_s(eV) \rho_t(0) + \int_0^{eV} \rho_s(E) \frac{d[T(E, V, z_0) \rho_t(E - eV)]}{d(eV)} dE \right\} \quad (1.26)$$

We see that two different terms contribute to the differential conductivity. The quantity of interest, namely the sample LDOS at the energy selected by the applied bias,  $\rho_s(eV)$ , is contained in the first term of the right-hand side in Eq. (1.26). The second one is a *background* term that arises from the voltage dependence of the transmission coefficient as well as from a non-constant tip LDOS. Since the second term has usually a smooth behavior, it is common to neglect it, identifying the  $dI/dV$  with the sample LDOS. However, this is usually possible as far as a narrow interval around the Fermi energy is considered (i.e. between  $-1$  V and  $+1$  V). For wider voltage ranges, the role of the second term together with the exponential energy behavior introduced by  $T$  in the first term cannot be neglected anymore. Therefore, in many experimental situations, the general problem of an STS experiment is to properly extract the sample LDOS contained in a non trivial way in the differential conductivity, as evident in Eq. (1.26); this procedure is called *normalization*.

### 1.2.2 Normalization methods

A number of methods have been proposed to face the crucial issue of normalization<sup>[29–31]</sup>. Historically, the first one is due to Strosio *et al.*<sup>[29]</sup>, who argued about the possibility of removing the effects of the voltage dependence of the tunneling coefficient normalizing the differential conductivity to the total conductivity  $I/V$ . Interpreting this procedure with the present 1D-WKB description leads to the expression:

$$\frac{dI/dV}{I/V} = \frac{T(eV, V, z_0)\rho_s(eV)\rho_t(0) + \int_0^{eV} \rho_s(E) \frac{d[T(E, V, z_0)\rho_t(E - eV)]}{d(eV)} dE}{\frac{1}{eV} \int_0^{eV} T(E, V, z_0)\rho_s(E)\rho_t(E - eV) dE} \quad (1.27)$$

From Equation (1.27) it is clear that such normalized differential conductivity is not simply related to the sample LDOS. However, in many experimental situations, especially in the case of semiconducting surfaces, this method leads to results that are qualitatively in agreement with surface LDOS simulated or measured with other spectroscopy techniques. For this reason, even if this treatment lacks of strong theoretical foundation, it has become a very common tool for presentation and interpretation of STS data.

A first refinement has been provided in the work of Ukraintsev<sup>[30]</sup>. Starting from Equation (1.26) he showed the possibility to write a symmetric expression of the  $dI/dV$  with respect to the tip and sample LDOSs. From the resulting expression, an approximate form of the differential conductivity can be obtained, neglecting the effects coming from the background term:

$$\frac{dI}{dV} \simeq A [T(eV, V, z_0)\rho_s(eV)\rho_t(0) + T(0, V, z_0)\rho_s(0)\rho_t(-eV)] \quad (1.28)$$

From this expression an estimate of the sample and tip DOS can be performed dividing  $dI/dV$  by the transmission coefficient  $T_{sym} = A[T(eV, V, z_0) + T(0, V, z_0)]$  and exploiting the peculiar dependence of  $T_{sym}$  on  $V$ . The resulting estimates for the sample and tip LDOS are:

$$\rho_s(eV) \propto \frac{dI/dV}{T_{sym}} \quad (V > 0); \quad \rho_t(-eV) \propto \frac{dI/dV}{T_{sym}} \quad (V < 0) \quad (1.29)$$

This method then provides an approximate treatment for the analysis of *unoccupied* states, for both the sample and the tip. From Equation (1.24) and (1.28) it follows that  $T_{sym}$  is symmetrical in the applied voltage, while  $dI/dV$  curve should not, since this feature is also governed by the LDOS of the tip and sample at the Fermi level, as it can be observed in Eq. (1.28). So, another possibility is to normalize the differential conductivity using an asymmetric expression for the transmission coefficient  $T_{as} = A_1T(eV, V, z_0) + A_2T(0, V, z_0)$ . Both  $T_{sym}$  and  $T_{as}$  are strongly influenced by the tip-sample distance  $z_0$ , so it is necessary to make an appropriate choice for this parameter.

In Ref. [31], Koslowski *et al.* further elaborated Equation (1.26), in order to provide a more quantitative treatment of the background term and produce an expression more explicitly related to the sample LDOS. Using the 1D-WKB expression of  $T$  and the mean value theorem for integrals, it follows that:

$$A \int_0^{eV} \rho_s(E)\rho_t(E - eV) \frac{d[T(E, V, z_0)]}{d(V)} dE = -f(z_0, V)I(V) \quad (1.30)$$

where the function  $f(z_0, V)$  is given by

$$f(z_0, V) = \frac{z_0 \hbar}{\sqrt{8m [\Phi + eV/2 - \bar{E}(V)]}} \quad (1.31)$$

and it can be evaluated for the particular considered system through  $\bar{E}(V)$ ; also, it generally depends on the effective work function, as well as on  $z_0$  and  $V$ . The extraction of the sample LDOS, then, follows from Equations (1.26) and (1.30), leading to the following relation:

$$\rho_s(eV) = \frac{1}{AT(eV, V, z_0)\rho_t(0)} \left[ \frac{dI}{d(eV)} + \frac{1}{e} f(z_0, V) I(V) \right] \quad (1.32)$$

The main limitation of this method lies in the hypothesis that the tip LDOS is constant. Generally, the tip LDOS is not known *a priori* and it is not possible to exclude any effects on the STS measurement resulting from a non-constant tip LDOS. In this regard, in literature other normalization methods were presented being more advanced than those described above and including the problem related to a non-constant tip LDOS; for example, Passoni *et al.*<sup>[32]</sup> discussed all the aforementioned methods and proposed an extension of them, focusing on two main issues: on the one hand, the improvement of the physical model and estimate of WKB parameters; on the other hand, the investigation of the effects of the tip electronic structure.

# Thin films of metal oxides on metallic surfaces

The growth of thin films on solid substrates holds an essential role in the modern technology, notably in nanotechnology. Some fields which make use of thin film deposition are, for example, microelectronics, magnetoelectronics, optoelectronics and catalysis. The term *thin film* generally refers to a layer with thickness going from less than one nanometer to some microns; the more specific expression *ultrathin film*, in addition, is related to a film with a very low thickness (e.g. a few nanometers).

The aforementioned thin films and, notably, ultrathin films represent a sort of low-dimensional systems, therefore systematic differences in the structural, electronic and chemical properties arise with respect to the bulk counterpart<sup>[33]</sup>. In this framework, as mentioned in Chapter 1, STM is a very powerful technique to inspect this kind of films and understand both their morphological/structural properties and electronic ones. A suitable substrate for the deposition of ultrathin films, as an example, is the (111) surface of gold, since its surface reconstruction is able to provide some preferential nucleation sites for some metals and metal oxides (e.g. CoO<sup>[34]</sup>).

## 2.1 The surface of Au(111)

### 2.1.1 Morphology and structure

Gold, as many other metals, shows the phenomenon of *reconstruction* at single-crystal surface; however, it is the only face-centered cubic (FCC) one whose (111) surface exhibits this phenomenon<sup>[35]</sup>. This was observed with different techniques, such as helium atom scattering (HAS)<sup>[36]</sup>, and a model of the unit cell was proposed; this is depicted in Figure 2.1. The unit cell shows a  $(22 \times \sqrt{3})$  reconstruction, which means that the dimensions of this cell are respectively 22 and  $\sqrt{3}$  times larger than the ones of the substrate unit cell (i.e. the bulk unit cell). In addition, this cell is characterized by different stacking regions: in the middle it has a hexagonal close-packed (HCP) stacking, whereas in the lateral regions a FCC one. These areas are separated by two transition regions, called *discommensuration lines*, whose direction is  $\langle 11\bar{2} \rangle$ . Also, the topographic profile is not planar but shows a corrugation of about 0.2 Å. Both the

corrugation and the FCC/HCP alternation come from uniaxial compression along the  $\langle 1\bar{1}0 \rangle$  direction, which allows to allocate 23 atoms on 22 bulk atomic sites, giving rise to the  $(22 \times \sqrt{3})$  reconstruction. Moreover, some atoms are displaced along the  $\langle 11\bar{2} \rangle$  direction, occupying HCP sites instead of FCC ones, so that atoms in transition areas are forced to take up *bridge* positions, which are higher than the superficial plane.

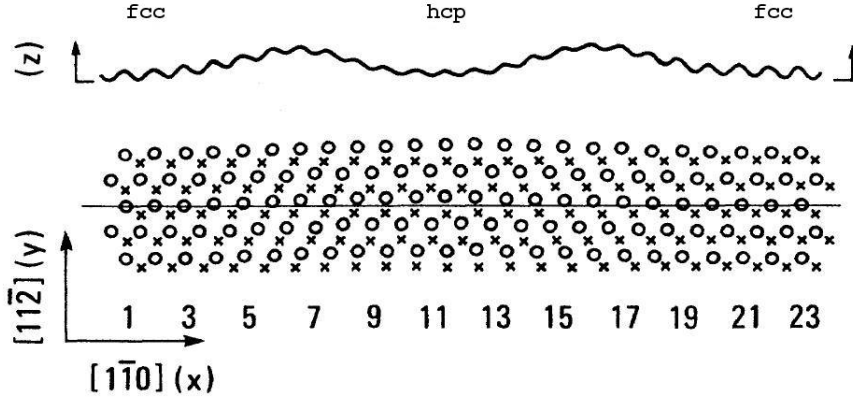


**Figure 2.1:** Model of the  $(22 \times \sqrt{3})$  reconstructed cell. Above, the topographic profile along the  $[1\bar{1}0]$  direction. Below, the schematic representation of the atomic sites within the cell: the crosses denote the positions of atoms in the second layer, whereas open circles denote the positions of atoms in the reconstructed top layer.<sup>[35]</sup>

Thereafter, the Au(111) $(22 \times \sqrt{3})$  surface reconstruction was confirmed with STM<sup>[35,37]</sup>. As an example, Figure 2.2(a) shows a high-resolution STM image in which the reconstructed surface unit cell has been highlighted. The discommensuration lines here appear as light parallel stripes. In the large-scale image in Figure 2.2(b), instead, they follow a “zig-zag” path. This is called *herringbone reconstruction* and it is a peculiar superstructure due to symmetry reasons; indeed, three equivalent directions to the  $[1\bar{1}0]$  exist, so that the surface can relax the uniaxial stress producing a regular pattern of different domains, which form angles of  $\pm 120^\circ$  between them. Two kinds of “ridges” exist, according to the way they undergo this rotation: the so-called X ridges bulge out towards the convex side of the bend, whereas the Y ridges follow a smoother curve. The point where a ridge bends is called *elbow* and, speaking of X ridges, one elbow can be said *bulged* if the prominence heads towards the FCC region; conversely, it can be said *pinched*. The already mentioned lattice compression, moreover, is not the same for all the different sites on the reconstructed surface (discommensuration lines, elbows, HCP and FCC regions), hence they show different values of lattice constants (2.86 Å for the FCC and HCP regions, 2.72-2.75 Å for the ridges and 2.65-2.68 Å for the elbows)<sup>[38]</sup> and they consist in non-equivalent sites from the energetic point of view.

Furthermore, on a freshly prepared Au(111) surface many and various defects can be observed, as reported by Barth *et al.*<sup>[37]</sup>. Such defects are mainly represented by U-shaped connections between adjacent ridges, which usually enclose HCP domains and occasionally FCC ones, or distorted elbows, which can be found near some terrace steps or where differently oriented domains meet.

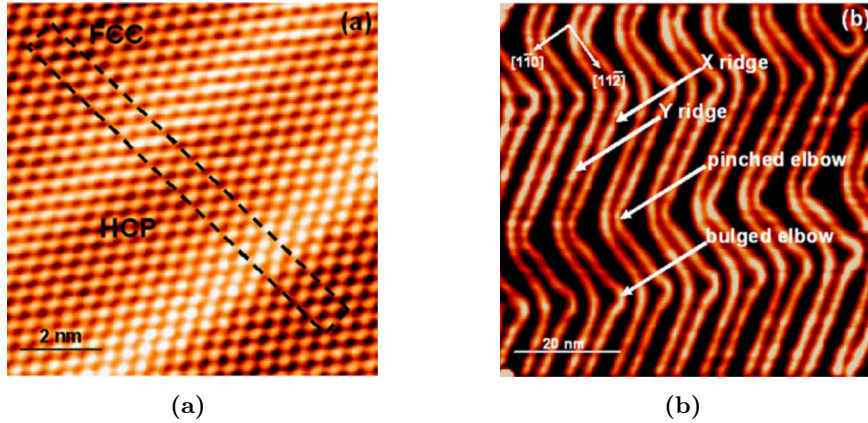


**Figure 2.2:** STM images of the clean Au(111) surface. **(a)** Atomically resolved STM image ( $V = -0.4$  V,  $I = 0.6$  nA) showing the  $(22 \times \sqrt{3})$  unit cell (indicated by a dashed rectangle). The bright ridges (corrugation  $\sim 0.2$  Å) running along the  $\langle 11\bar{2} \rangle$  direction represent the discommensuration lines composed by atoms in between two different stacking positions. **(b)** Large scale STM image ( $V = -1$  V,  $I = 1$  nA) of the typical *herringbone* surface reconstruction of Au(111).<sup>[39]</sup>

### 2.1.2 Electronic structure

Generally speaking, if one wants to study the electronic states of a crystalline solid at its surface, the so-called *surface states* must be considered: they are a sort of localized eigenstates due to the simple presence of the surface itself. This fact causes two additional difficulties, with respect to the bulk problem: 1) translational symmetry only exists in directions within the plane of the surface; 2) due to the changed chemical bonds at the surface, surface relaxations and reconstructions frequently occur. From the theoretical point of view, surface states can be described with the nearly-2D-free-electron model and, for historical reasons, they are called *Shockley states*; on the other hand, they can be described in terms of the tight-binding approximation, called *Tamm states*; the difference between them is just the mathematical approach<sup>[40]</sup>.

The Au(111) surface notably exhibits remarkable electronic properties that are dominated by its *sp*-derived Shockley surface state. This is a typical feature of other (111) surfaces, such as Cu(111) and Ag(111)<sup>[41]</sup>. The Au(111) surface state consists of delocalized electrons which are confined to the top atomic layers of the surface and, as previously mentioned, they can be described in terms of the nearly-2D-electron model.

From the experimental side, the Au(111) surface state can be investigated with various techniques, such as STS; with this technique not only is it possible to determine the energetic position of this state, but also to unveil differences between HCP and FCC regions<sup>[42]</sup>. Figure 2.3(a) shows the  $dI/dV$  curves taken in different regions of the Au(111) surface (HCP, FCC and ridges); generally, the Shockley surface state is similar to a step function arising at  $-0.46$  eV; in addition, the HCP regions show a higher peak at lower energy with respect to FCC ones. The differential conductivity map in Figure 2.3(b), instead, can be used to understand the spatial modulation of the LDOS, due to the scattering phenomena of electrons with impurities, steps or other defects on the surface.

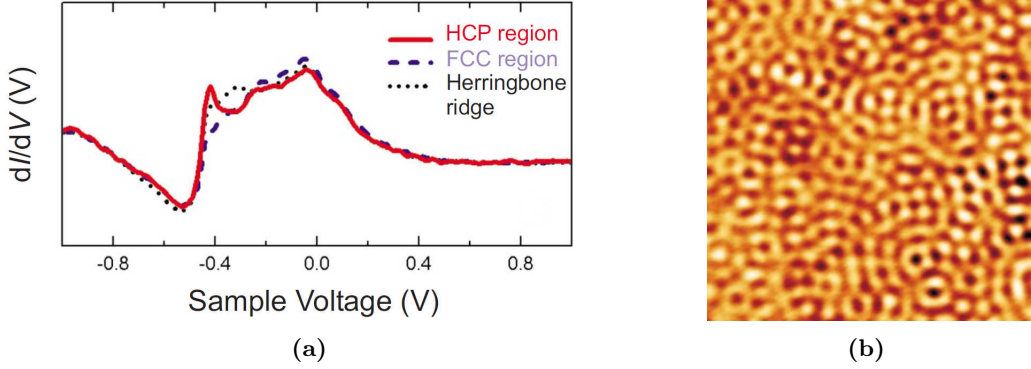


**Figure 2.3:** (a)  $dI/dV$  curves of Au(111) reveal a steplike onset around  $-460$  meV, the signature of the surface state. The HCP region contains a higher density of lower-energy electrons, while the FCC region contains more high-energy electrons ( $T = 4.5$  K). (b)  $35.3 \times 35.3$  nm<sup>2</sup> LDOS map at  $-30$  meV of an Au(111) terrace ( $T = 78$  K).<sup>[42]</sup>

From a theoretical point of view, in order to model the Au(111) Shockley state, the potential seen by a 2D surface-state electron can be approximated as an extended square-well Kronig-Penney (KP) potential<sup>[43]</sup> having the same periodicity as the reconstruction, as in the work of Chen *et al.*<sup>[44]</sup>. This potential is periodic along the  $[1\bar{1}0]$  surface direction (“ $x$  direction”, perpendicular to the ridges) and constant along the  $[11\bar{2}]$  direction (“ $y$  direction”, parallel to the ridges); in this simple model, indeed, domain rotation is ignored. With a suitable calculation, the following expression of the local density of states (LDOS) can be found<sup>[44]</sup>:

$$\rho_L(E, x, y) = \frac{a + b}{\pi^2} \sqrt{\frac{2m^*}{\hbar^2}} \int_0^{k'} dk_x |\Psi_{k_x, k_y}(x, y)|^2 \frac{1}{\sqrt{E - \varepsilon(k_x)}} \quad (2.1)$$

where  $a = 25$  Å represents the width of the HCP region (width of the square potential well),  $b = 38$  Å represents the width of the FCC region (“crest” of the periodic potential)  $\varepsilon(k_x)$  is the 1D KP dispersion relation along  $[1\bar{1}0]$ ,  $k' = \sqrt{2m^*E/\hbar^2}$  and  $m^* = 0.26m_e$ ; the latter is the effective mass of a surface-state electron ( $m_e$  is the electron mass). Figure 2.4 shows this quantity calculated at the centers of both the HCP and FCC regions of the extended KP potential. At low energy (just before  $-0.4$  eV) a large peak in the HCP LDOS dominates over a much reduced FCC peak; this behavior is due to the “bound state” nature of eigenstates, whose energy lie below the top of the square-well potential. At slightly higher energy, instead, electrons are no more localized inside the square-wells but are in the “continuum” regime and the FCC (barrier region) state density rises above the HCP curve. This behavior is very similar to the experimental data (Fig. 2.3(a)).

## 2.2 Monocrystalline titanium dioxide

### 2.2.1 Morphology and structure

Titanium oxide is one of the most studied monocrystalline systems in the whole surface science of metal oxides; also, it can be applied in several technological fields.

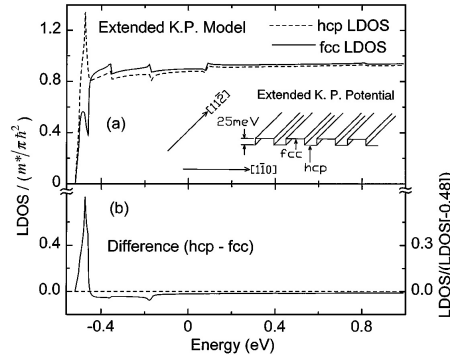


**Figure 2.4:** (a) Theoretical LDOS calculated at the centers of the HCP and FCC regions of the extended Kronig-Penney potential; the inset shows a sketch of the potential. (b) Difference of theoretical LDOS curves shown in (a).<sup>[44]</sup>

The naturally occurring oxide of titanium is  $\text{TiO}_2$  and it is often referred to as *titania*. It crystallizes in three major different structures: *rutile* (tetragonal), *anatase* (tetragonal) and *brookite* (rhombohedral); however, the latter is by far less important in the applications of  $\text{TiO}_2$ . Figure 2.5 shows the bulk structures of rutile and anatase: in both phases the basic building block consists of a titanium atom surrounded by six oxygen atoms in a more or less distorted octahedral configuration<sup>[9]</sup>.

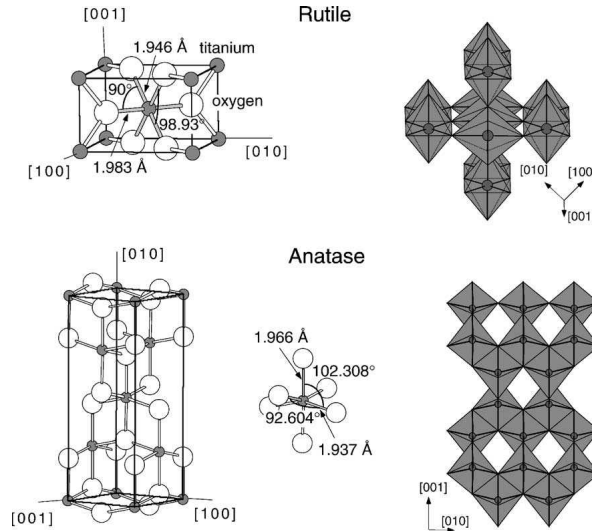


**Figure 2.5:** Bulk structures of rutile and anatase. The tetragonal bulk unit cell of rutile has the dimensions  $a = b = 4.587 \text{ \AA}$ ,  $c = 2.953 \text{ \AA}$ , and the one of anatase  $a = b = 3.782 \text{ \AA}$  and  $c = 9.502 \text{ \AA}$ .<sup>[9]</sup>

Rutile surfaces have been extensively studied with microscopic and spectroscopic techniques, especially the (110) surface, which is the stablest one from a thermodynamical point of view. On the other hand, scientific research on anatase has developed more recently and studies about (101) and (001) stable surfaces have been carried out<sup>[9]</sup>. For example, Figures 2.6 and 2.7(c) show two STM images of anatase (101) and rutile (110) surfaces, respectively. Figure 2.7(a)-2.7(b), instead, shows a scheme of the rutile crystal structure and of the (110) surface, neglecting the relaxation effects.

The interpretation of STM images of oxides, generally speaking, is not manifest

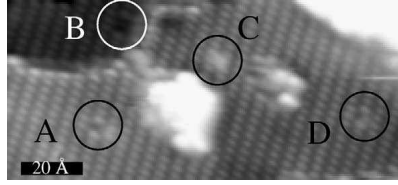


**Figure 2.6:** STM image of anatase (101) surface ( $13 \times 6 \text{ nm}^2$ ,  $V = 1.22 \text{ V}$ ,  $I = 1.23 \text{ nA}$ ). The labeled circles highlight four types of point defects<sup>[9]</sup>.

because of strong variations in the electronic structure and because tips can easily catch a surface oxygen atom. The same occurs for titanium dioxide surfaces and it is not always clear if the bright surface features are related to topographic protrusions or to electronic effects. Considering Figure 2.7(c), one may suppose that the so-called bridging oxygen atoms (missing one bond to one Ti atom) generate a topographic contrast since they emerge above the main surface plane. However, normally this is not the case: instead, Ti sites are imaged bright in this and similar images. To understand this, the electronic structure of  $\text{TiO}_2$  should be considered. A  $\text{TiO}_2$  crystal can be *reduced*, which means that oxygen vacancies are present, so that the O:Ti stoichiometric ratio is slightly lower than 2. This effect can be obtained with an annealing treatment in UHV. From an electronic point of view, this material becomes a *n*-type semiconductor, since  $\text{Ti}^{3+}$  ions are present and they act as donor atoms ( $\text{Ti}^{3+} \rightarrow \text{Ti}^{4+} + e^-$ ). This material has a band gap of about 3 eV with the  $E_F$  near to the bottom of the conduction band ( $E_c$ ); applying a positive bias between the tip and the sample, consequently, electrons can flow from the former to the latter's conduction band. If this positive bias is lower than 2 V, the conduction states of the sample, which contribute to the tunneling, are near to  $E_c$  and they mainly come from 3*d* states of titanium cations, so Ti atoms are expected to appear bright in STM images in constant current mode (as in Fig. 2.7(c)). On the contrary, the valence band has a 2*p*-like character due to 2*p* atomic orbitals of oxygen atoms. Even if a topographic-electronic controversy exists, presently the contribution of empty localized states of titanium atoms is considered predominant (at positive and moderate voltages), thanks to both experimental and theoretical evidences<sup>[9]</sup>.

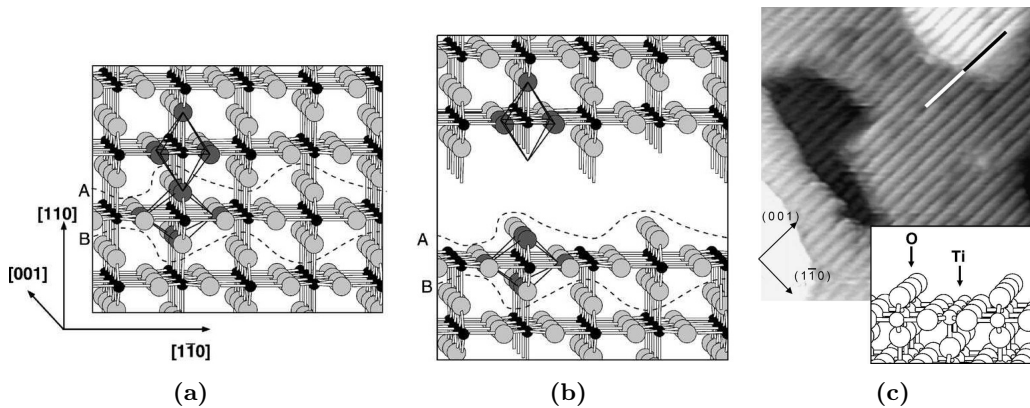


**Figure 2.7:** (a) Ball-and-stick model of the rutile crystal structure. (b) The crystal is “cut” along line A and the resulting surface is the (110)-(1×1) one. (c) STM image of the same surface ( $14 \times 14 \text{ nm}^2$ ,  $V = 1.6 \text{ V}$ ,  $I = 0.38 \text{ nA}$ ). The inset shows the model of the same unrelaxed surface.<sup>[9]</sup>

## 2.2.2 Electronic structure

There is a widespread agreement in the scientific community that the electronic structure of stoichiometric  $\text{TiO}_2$  surfaces is not so different from that of the bulk, since no surface states are observed; on the other hand, non-stoichiometric surfaces exhibit this kind of surface states<sup>[9]</sup>.

Considering stoichiometric  $\text{TiO}_2$  surfaces, the occupied states are mostly  $\text{O}_{2p}$ -derived, even if a certain degree of covalency is present; indeed, this effect is stronger on the (110) surface, where the covalency of bonds between bridging O atoms and the underlying sixfold coordinated Ti atoms is magnified. On the other hand, the conduction band is mostly  $\text{Ti}_{3d}$ -derived, where the crystal field removes the degeneracy of the  $d$  orbitals, splitting them into two sub-bands. An experimental measurement of X-ray absorption which shows this effect is represented in Fig. 2.8(a). Finally, due to the electronic structure analogy between the bulk  $\text{TiO}_2$  and its stoichiometric surface, the band gap value  $E_g = 3.1$  eV still holds in this case<sup>[9]</sup>.

On the other hand, a reduced  $\text{TiO}_2$  (110) surface can be obtained after annealing at high temperature or electron bombardment, so that some bridging oxygen atoms will be missing. Figure 2.8(b) shows two typical photoemission spectra, from the valence band region, which highlight this effect: the solid line comes from a reduced  $\text{TiO}_2$  (110) surface, obtained after sputtering and annealing in ultra-high vacuum (UHV), and a defect state within the band gap is evident; after adsorption of molecular  $\text{O}_2$  at room temperature, then, this state disappears and the spectrum is shifted to higher binding energy (dashed line)<sup>[9]</sup>.

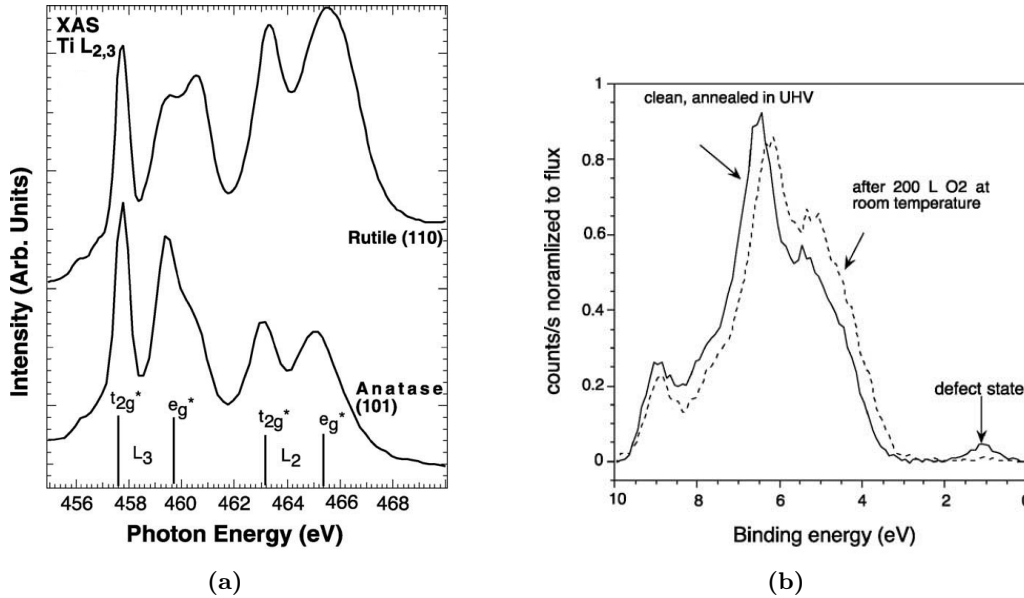


**Figure 2.8:** (a) X-ray absorption spectra of the  $\text{Ti}2p$  edge of a stoichiometric, well-ordered rutile  $\text{TiO}_2$  (110) surface. (b) Photoemission spectra ( $h\nu = 35$  eV, normal emission) from the valence band region of a sputtered and UHV-annealed, clean  $\text{TiO}_2$  (110) surface.<sup>[9]</sup>

Despite the great interest on the  $\text{TiO}_2$  (110) surface, STS measurements on it are quite uncommon. An example is the work of Batzill *et al.*<sup>[45]</sup>, which is focused on the electronic properties of a reduced surface with the presence of defects, such as  $(1 \times 2)$  strands, which are characterized by a  $\text{Ti}_2\text{O}_3$  stoichiometry, and step edges. Figure 2.9(a)

shows the results ( $dI/dV$  curves) for different regions of the surface; the spectra were recorded at  $-1.6$  V. The different electronic properties of these regions, however, is beyond the goal of this section. An earlier work of Sakai *et al.*<sup>[46]</sup>, instead, was aimed to a more general STS study of the  $\text{TiO}_2$  (110)( $1 \times 1$ ) surface. Figure 2.9(b) shows the  $dI/dV$  spectra acquired on “bright rows” and “dark rows” of the  $\text{TiO}_2$  (110)( $1 \times 1$ ) surface; the former are mainly attributed to fivefold coordinated Ti ions, the latter simply to the space between the previous ones. The curve recorded on the bright rows shows a broad peak, on the contrary of the curve acquired between the rows. In all these STS experiments, finally, the Fermi level (corresponding to a zero applied voltage) is close to the bottom of the conduction band ( $E_c$ ), which is a typical feature of a  $n$ -type semiconductor.

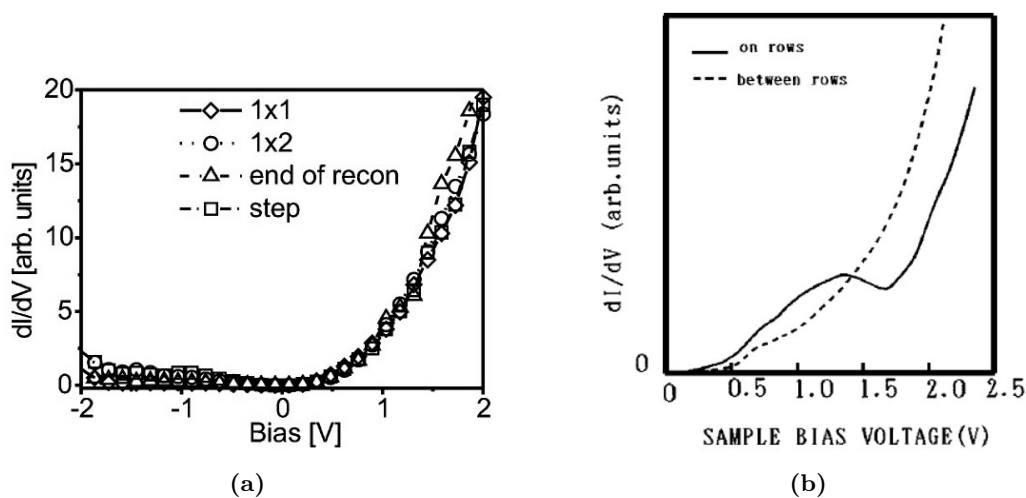


**Figure 2.9:** STS measurements on the  $\text{TiO}_2$  (110) surface. (a) Differential conductivity curves on different areas of the surface. ( $1 \times 1$ ), ( $1 \times 2$ ), the termination of the ( $1 \times 2$ ) strands and [001] step edges are discriminated<sup>[45]</sup>. (b) Differential conductivity measured on the rows (solid curve) and in the spaces between rows (dotted curve)<sup>[46]</sup>

## 2.3 Fundamentals of nucleation and growth of thin films

Many techniques of thin films deposition have been developed and widely used not only in research laboratories, but also in industries. In this section few basic concepts of this topic are briefly explained, since they are mandatory for a whole understanding of the subject of this thesis work.

Film growth methods can be generally divided into two groups: vapor-phase deposition and liquid-based growth. The former includes, for example, evaporation, molecular beam epitaxy (MBE), sputtering, chemical vapor deposition (CVD) and atomic layer deposition (ALD)<sup>[47]</sup>. The latter is less important for our purposes, since this thesis work does not involve any liquid-based growth. The previous examples of vapor-phase growth methods, moreover, can be summarized in two main families: *chemical vapor deposition* (CVD, already mentioned) and *physical vapor deposition* (PVD). CVD is the process of chemically reacting a volatile compound of a material to be deposited, with other gases, to produce a non-volatile solid that deposits

atomistically on a suitably placed substrate<sup>[48]</sup>. On the other hand, physical vapor deposition (PVD) is a process of transferring growth species from a source or a target and deposit them on a substrate to form a film; the process proceeds atomistically and mostly involves no chemical reactions<sup>[47]</sup>. The deposition technique employed in the experimental activity presented in this paper is the *electron beam evaporation*; this will be explained in the Appendix A.4.

The individual atomic processes which determine film growth in its initial stages are illustrated in Figure 2.10. First of all, a particle from the gas phase can condensate on the surface; then, it might immediately re-evaporate or it may diffuse along the surface. This diffusion process can lead to adsorption, especially in defect sites, or to a re-evaporation (also in this case). Besides adsorption and surface diffusion, nucleation of more than one adsorbed particle might occur, as well as the growth of an already formed island thanks to the addition of new particles. During film growth, interdiffusion is often an important process: substrate and film atoms can exchange places and the film-substrate interface is smoothed. The occurrence (or nonoccurrence) of these processes depends on the surface features, surface temperature and particles energy with respect to the activation energies of the individual processes. Also, it should be noted that the film growth is a non-equilibrium phenomenon, so a global theory of film growth requires a description in terms of rate equations (kinetic theory) for each of the processes depicted in Fig. 2.10<sup>[40]</sup>.

Instead of following this kind of theoretical atomistic approach, the film growth process can be considered under a phenomenological view. Generally speaking, three different modes of film growth can be distinguished (Fig. 2.11):

1. *layer-by-layer* growth mode (or Frank-van der Merwe, FM);
2. *layer-plus-island* growth mode (or Stranski-Krastanov, SK);
3. *island growth* (or Volmer-Weber, VW).

In the first case, the interaction between substrate and film atoms is stronger than the one between neighboring layer atoms; a new layer starts growing only when the previous one is completed. The VW growth is the opposite: the interaction between neighboring film atoms overcomes the overlayer-substrate one, leading to island growth with tridimensional shape. The Stranski-Krastanov growth is a sort of intermediate case: after the formation of one, or sometimes several complete monolayers, island formation occurs<sup>[40]</sup>.

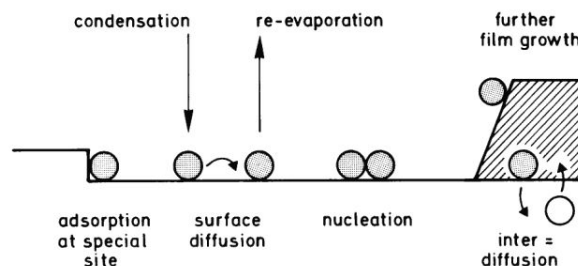


**Figure 2.10:** Schematic representation of atomic processes involved in film growth on a solid substrate. Film atoms shown as dark circles, substrate atom as open circle<sup>[40]</sup>.

*Epitaxy* is a very particular process and refers to the formation or growth of single crystal over a single crystal substrate (or seed). Epitaxial growth can be further divided in *homoepitaxy*, which is the growth of a film over a substrate in which both

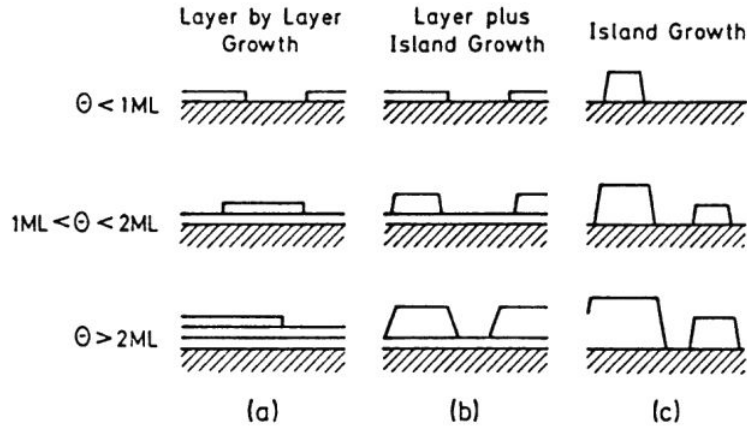


**Figure 2.11:** Schematic illustration of the three main growth modes of a film for different coverage ( $\Theta$ ) regimes (ML means monolayer). (a) Layer-by-layer growth (Frank-van der Merwe). (b) Layer-plus-island growth (Stranski-Krastanov). (c) Island growth (Volmer-Weber).<sup>[40]</sup>

are the same material, and *heteroepitaxy*, in which the growing material is different from the substrate. Heteroepitaxial growth is frequently *pseudomorphic*, which means that the deposit grows with a lattice constant matched to the substrate<sup>[49]</sup>. In the case of homoepitaxy there is no lattice mismatch between the two, whereas in the second case it is given by:

$$f = \frac{a_s - a_f}{a_f} \quad (2.2)$$

where  $a_s$  is the unstrained lattice constant of the substrate and  $a_f$  is the unstrained lattice constant of the film. If  $f > 0$ , the film is strained in tension, whereas if  $f < 0$ , it is strained in compression. Figure 2.12 schematically illustrates the cases of homoepitaxial and heteroepitaxial (strained and relaxed) structures<sup>[47]</sup>.

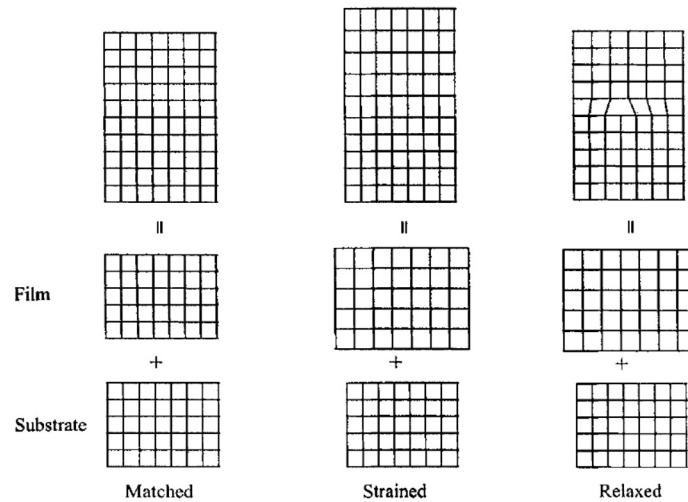


**Figure 2.12:** Schematic illustrating the lattice matched homoepitaxial film and substrate, strained and relaxed heteroepitaxial structures<sup>[47]</sup>.

## 2.4 Metal oxide ultrathin films on (111) metal surfaces

Many methods to realize metal oxides ultrathin films exist; two main classes can be distinguished<sup>[50]</sup>:

- *physical methods*, such as controlled oxidation of bulk single-crystal surfaces, sputter deposition, pulsed laser deposition (PLD), reactive physical vapor deposition, sputtering or ablation of pure targets in oxidizing atmosphere, reactive molecular beam epitaxy, post-oxidation of pre-deposited thin metal films;
- *chemical methods*, such as chemical vapor deposition (metal organic CVD, ALD...), reactive-layer-assisted deposition (RLAD).

The preparation method strongly influences the morphological properties of the oxide film, since the growth-related physical mechanisms and kinetic factors which characterize it vary depending on the oxidation method employed. In addition, the growth and the morphology of the oxide film depend on the experimental variables, such as substrate temperature, deposition rate, partial pressure of oxidizing agents, temperature and time of thermal treatments. Furthermore, the substrate itself influences the final properties of the film. From the structural point of view, a suitable metal support for film growth is characterized by many parameters<sup>[33]</sup>:

1. the atomic arrangement in the metal surface should match the symmetry of the oxide unit cell along the desired growth direction;
2. the formation of high quality interfaces requires a small difference between metal and oxide lattice constants (less than 5% to have a pseudomorphic growth<sup>[51]</sup>);
3. support and ad-layer should be non-miscible at the interface and the support should have a good thermal and mechanical stability.

In addition, the term *coverage* is frequently used in ultrathin film deposition, which refers to the amount of overlayer material deposited on the substrate. For metals it is expressed in monolayers (ML): one monolayer corresponds to the density of substrate atoms per unit area; for metal oxides, instead, it is expressed in equivalent monolayers (MLE): 1 MLE represents the oxide film coverage obtained with the oxidation of 1 ML of metal film. Speaking of metal oxides, also, another unit of measurement should be introduced, the Langmuir (L): 1 L is the dosage corresponding to exposure of the surface for 1 s to a gas (in our case, oxygen) pressure of  $10^{-6}$  Torr<sup>[40]</sup>.

In the following sections some systems of metal oxides over (111) metal surfaces will be briefly analyzed; the growth of  $\text{TiO}_x$  nanostructures on Au(111) will be described in more detail in Section 2.5.

### 2.4.1 $\text{TiO}_x/\text{Pt}(111)$

An extensive study of the system  $\text{TiO}_x/\text{Pt}(111)$  has been performed by the research group of Granozzi<sup>[52–55]</sup>. In these works, titanium is deposited at a controlled rate in the presence of oxygen (reactive deposition) and at room temperature; the as-deposited film is then annealed at a certain temperature and partial oxygen pressure (or in UHV) to get a single  $\text{TiO}_x/\text{Pt}(111)$  phase. In these papers, different phases have been observed, both varying the coverage and the experimental parameters; some of them exhibit hexagonal

symmetry (Fig. 2.13 and 2.15), other rectangular one (Fig. 2.14), as evidenced by low-energy electron diffraction (LEED)<sup>[52]</sup>. Furthermore, on the basis of STM measurements of the film thickness with respect to the substrate, X-ray photoelectron spectroscopy (XPS) and X-ray photoelectron diffraction (XPD) measurements, the authors suppose that most of the observed phases consist of a O–Ti bilayer with titanium atoms at the film-substrate interface<sup>[52–54]</sup>.

At low coverage (0.4 MLE) and after annealing the sample at the temperature of 673 K in an oxygen pressure of about  $10^{-5}$  Pa, the *kagomé-like*<sup>a</sup>-TiO<sub>x</sub> is obtained (Fig. 2.13). The unit cell is shown in Fig. 2.13(b), whereas the structural model is shown in Fig. 2.13(c) after theoretical simulations<sup>[54]</sup>: the unit cell contains two titanium atoms (located in *hollow* sites of the substrate lattice) forming a *honeycomb* lattice and three oxygen atoms (located in *bridge* sites) forming a *kagomé* pattern; the stacking is such that O atoms are the topmost layer and the stoichiometry is Ti<sub>2</sub>O<sub>3</sub>. This model is obtained under the hypothesis that at negative bias the negatively charged oxygen ions are imaged (current tunneling from valence occupied states). For the sake of simplicity, the model in Fig. 2.13(c) represents a commensurate (2×2) reconstructed overlayer, whereas the measured one is incommensurate, with a (2.15×2.15) reconstruction, as evidenced by LEED measurements<sup>[52,54]</sup>.

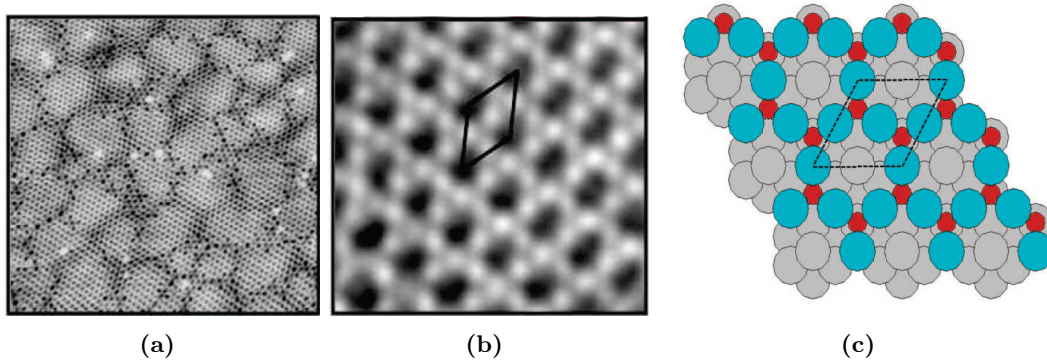


**Figure 2.13:** STM images and structural model of the *k*-TiO<sub>x</sub>/Pt(111) phase (0.4 MLE). (a)  $30 \times 30 \text{ nm}^2$ ,  $V = 1 \text{ V}$ ,  $I = 1 \text{ nA}$ . (b)  $3 \times 3 \text{ nm}^2$ ,  $V = -0.4 \text{ V}$ ,  $I = 1.06 \text{ nA}$ . (c) Structural model: grey = Pt, red = Ti, blue = O.<sup>[54]</sup>

By increasing the coverage (0.8 MLE) at the same oxygen pressure of the previous case, the so-called *zig-zag* phase is obtained (*z*-TiO<sub>x</sub>, Fig. 2.14). This phase shows a rectangular unit cell (Fig. 2.14(b)) and the structural model (Fig. 2.14(c)), verified by theoretical simulations, implies a TiO<sub>1.33</sub> stoichiometry<sup>[56]</sup>. Since the STM image in Figure 2.14(b) has been taken at positive bias, tunneling is expected to occur from empty *d* states of Ti atoms, which will consequently appear as bright spots in the image. Moreover, the presence of two kinds of Ti atoms can be noticed: some of them are brighter than others. From the proposed model, this is an electronic effect: brighter Ti atoms are fourfold coordinated (each one is bonded to four oxygen atoms), whereas the less bright ones are threefold coordinated. Thus, the density of empty states of the first ones is higher than the second ones', making them appear brighter.

<sup>a</sup>Japanese name for a woven bamboo basket which exhibits the same type of structure on a “macroscopic” scale.

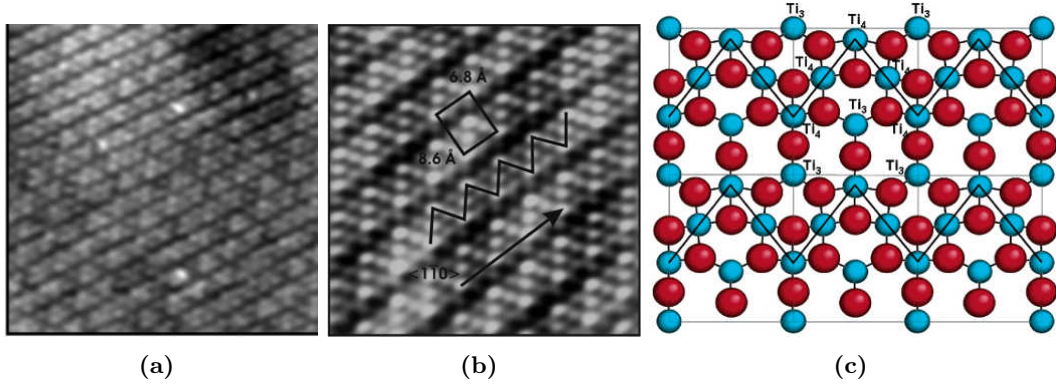


**Figure 2.14:** STM images and structural model of the  $z$ - $\text{TiO}_x/\text{Pt}(111)$  phase (0.8 MLE). (a)  $35 \times 35 \text{ nm}^2$ ,  $V = 0.9 \text{ V}$ ,  $I = 1.4 \text{ nA}$ . (b)  $6 \times 6 \text{ nm}^2$ ,  $V = 0.1 \text{ V}$ ,  $I = 1.5 \text{ nA}$ . (c) Structural model: red = O, blue = Ti.<sup>[56]</sup>

At a coverage of 1.2 MLE, after a post-annealing at 823 K and  $p_{\text{O}_2} = 10^{-5} \text{ Pa}$  (5 minutes), the so-called *pinwheel* or *wagon-wheel* phase ( $w$ - $\text{TiO}_x$ ) is obtained (Figs. 2.15 and 2.16). It is characterized by a  $(\sqrt{43} \times \sqrt{43})R7.6^\circ$  commensurate hexagonal unit cell (Fig. 2.15(b)); the structural model is shown in Fig. 2.15(c): yellow segments link the fourfold coordinated Ti atoms, whereas blue segments link the threefold coordinated ones, which are at the border of the central cavity. This model leads to a very good agreement with the STM images (the contrast is explained in the same way as in the *zig-zag* phase) and to a  $\text{TiO}_{1.2}$  stoichiometry. However, the theoretical Ti coverage predicted with this model (0.7 MLE) does not match the experimentally derived one ( $0.8 < x < 1.2$  MLE), which still is an issue<sup>[54]</sup>. Finally, two other kinds of *pinwheel* phases exist for this system (the more reduced  $w'$ - $\text{TiO}_x$  and the intermediate  $w_{\text{int}}$ ), which are still commensurate but show different values of unit cell vectors and rotation angle<sup>[53]</sup>. After their observations on this “family” of phases, the authors proposed the following definition: *a wagon-wheel (or pinwheel) structure is a hexagonal commensurate superstructure with symmetry  $p6$  which grows on a  $p6m$  substrate, and where the unit cell vector of the commensurate superstructure is rotated by a  $\theta$  angle with respect to the principal direction of the substrate*<sup>[53]</sup>.

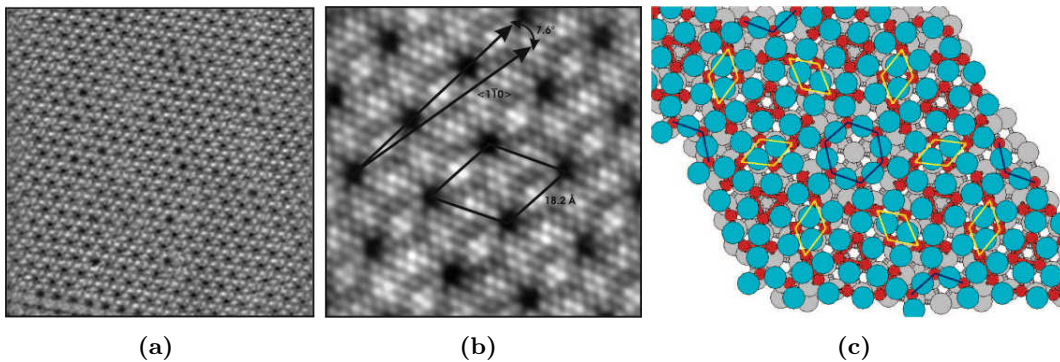


**Figure 2.15:** STM images and structural model of  $w$ - $\text{TiO}_x/\text{Pt}(111)$  phase (1.2 MLE). (a)  $35 \times 35 \text{ nm}^2$ ,  $V = 1 \text{ V}$ ,  $I = 0.6 \text{ nA}$ . (b)  $7.5 \times 7.5 \text{ nm}^2$ ,  $V = 1.3 \text{ V}$ ,  $I = 1.9 \text{ nA}$ . (c) Structural model: grey = Pt, red = Ti, blue = O.<sup>[52,54]</sup>

Initially, the STM observations have been discussed on the basis of a Moiré-like

model (Fig. 2.16(b), that is derivating from a modulation of the Ti occupancy of the different substrate sites (i.e. hollow, bridge and on-top sites)<sup>[52]</sup>. However, this Moiré-like model did not furnish any hypothesis on the nature of the hexagonally arranged black features detected by STM (Fig. 2.16(a)), nor on the positions occupied by the O atoms on the Ti layer. For a comparison between the two models (the previously described one and the Moiré-based one), the reader may look at Figs. 2.15(c) and 2.16(c), where similar rhombohedral arrangements of Ti atoms are highlighted: in the first case, as already mentioned, these are fourfold coordinated atoms; in the second case they are quasi-bridge atoms.

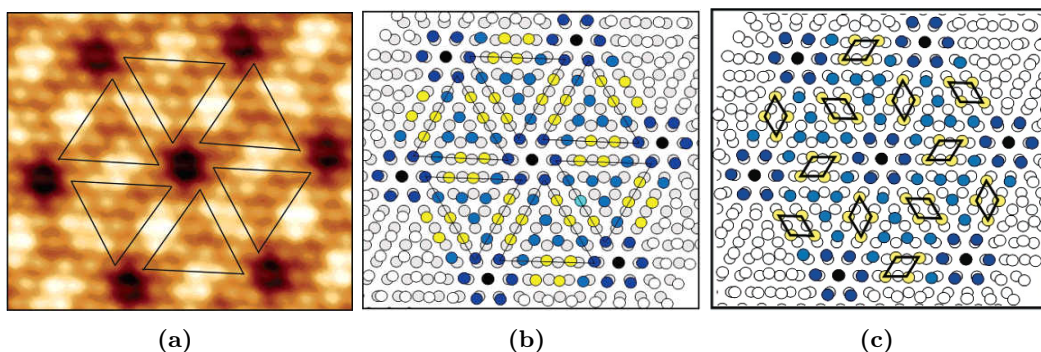


**Figure 2.16:** (a) Atomic resolution STM image of the *pinwheel* phase. (b) Schematic drawing of the Moiré-like coincidence between the Pt(111) lattice and the *w*-TiO<sub>x</sub> superlattice (yellow = quasi-bridge, light-blue = quasi-hollow, blue = quasi-top, black = on-top).<sup>[52]</sup> (c) Same model as (b), but the quasi-bridge Ti atoms are highlighted.<sup>[53]</sup>

In Table 2.1, finally, a schematic summary of the different phases exhibited by the system TiO<sub>x</sub>/Pt(111) at low coverages is shown (in this section only some of them have been described).

### 2.4.2 VO<sub>x</sub>/Pd(111)

The ultrathin films of vanadium oxide on Pd(111) have been investigated by the research group of Netzer and Surnev<sup>[57–60]</sup>. The growth method is, also in this case, reactive evaporation (V metal in an oxygen atmosphere,  $p_{O_2} = 10^{-7}$  mbar). In the sub-monolayer regime, different phases can be observed; notably, two of them are shown in Figure 2.17. The STM image in Fig. 2.17(a) was obtained after annealing the 0.25 MLE VO<sub>x</sub>/Pd(111) sample to 673 K and it shows the coexistence of two phases: the  $p(2 \times 2)$  *honeycomb* one and the *pinwheel* (or *wagon-wheel*) one. The former is more stable before the annealing (as-deposited conditions), whereas the latter substitutes the former as the post-annealing temperature rises, until the oxide decomposition occurs. The honeycomb lattice has a  $5.5 \pm 0.2$  Å separation, which is twice the Pd–Pd distance at the (111) surface, accordingly with the observed  $p(2 \times 2)$  pattern in LEED; conversely, the pinwheel superstructure can be described by  $(\sqrt{63} \times \sqrt{63})R19.1^\circ$  cell, using the Wood notation. Finally, this phase exhibits a bias-dependent appearance<sup>[57]</sup>.

According to Surnev *et al.*, the observed pinwheel phase for this system can be explained on the basis of the model proposed by Zhang *et al.*<sup>[61,62]</sup> for Cr overlayers on Pt(111) annealed at 800 K: the triangles' borders of the pinwheel hexagonal cell are

**Table 2.1:** Summary of the  $\text{TiO}_x$  phases on Pt(111) prepared in different conditions (i.e.  $\text{O}_2$  pressure, in Pa, and Ti dose, in MLE):  $k$  = *kagomé*;  $z$  = *zigzag-like*;  $w$  = *wagon-wheel-like*; *rect* = *rectangular*. Superstructures in matrix notation are related to the hexagonal mesh of Pt(111) with  $d = 2.77 \text{ \AA}$  and  $\alpha = 120^\circ$ . The corresponding unit cells are also reported. The actual stoichiometries reported were obtained from the corresponding models derived by density-functional calculations<sup>[6]</sup>.

Annealing $\text{O}_2$ pressure (Pa)	$5 \times 10^{-4}$		$\text{rect-TiO}_2$ $\begin{bmatrix} 1.16 & 0.18 \\ 0.58 & 1.56 \end{bmatrix}$ Incommensurate rectangular 3.8 $\text{ \AA}$ x 3.2 $\text{ \AA}$		$\text{rect}'\text{-TiO}_2$ $\begin{bmatrix} 1.37 & 0.0 \\ 1.95 & 2.55 \end{bmatrix}$ Incommensurate centred rectangular 3.7 $\text{ \AA}$ x 12.2 $\text{ \AA}$
	$10^{-5}$	$k\text{-TiO}_{1.5}$ $\begin{bmatrix} 2.15 & 0.0 \\ 0.0 & 2.15 \end{bmatrix}$ Incommensurate hexagonal 6 $\text{ \AA}$ x 6 $\text{ \AA}$	$z\text{-TiO}_{1.33}$ $\begin{bmatrix} 2.5 & 0 \\ 1.8 & 3.6 \end{bmatrix}$ Incommensurate rectangular 6.8 $\text{ \AA}$ x 8.6 $\text{ \AA}$	$w\text{-TiO}_{1.2}$ $\begin{bmatrix} 7 & 1 \\ -1 & 6 \end{bmatrix}$ Commensurate hexagonal 18.2 $\text{ \AA}$ x 18.2 $\text{ \AA}$ $(\sqrt{43} \times \sqrt{43})R7.6^\circ$	
	$10^{-8}$ (UHV)		$z'\text{-TiO}_{1.2}$ $\begin{bmatrix} 6 & 0 \\ 3 & 6 \end{bmatrix}$ Commensurate rectangular 16.6 $\text{ \AA}$ x 14.4 $\text{ \AA}$ $(6 \times \sqrt{3})\text{-rect}$	$w'\text{-TiO}_x$ $\begin{bmatrix} 8 & 3 \\ -3 & 5 \end{bmatrix}$ Commensurate hexagonal 19.4 $\text{ \AA}$ x 19.4 $\text{ \AA}$ $(7 \times 7)R21.8^\circ$	
		0.4	0.8	1.2	$\geq 2$
<b>Equivalent monolayer (MLE)</b>					

referred to as dislocation lines of the substrate's surface induced by the formation of a surface V-Pd alloy<sup>[57]</sup>. This model, for example, cannot be applied to the aforementioned  $\text{TiO}_x/\text{Pt}(111)$  since in this case there is no evidence for any dislocation line and there is a rotation between the substrate's and overlayer's unit cells<sup>[53]</sup>.

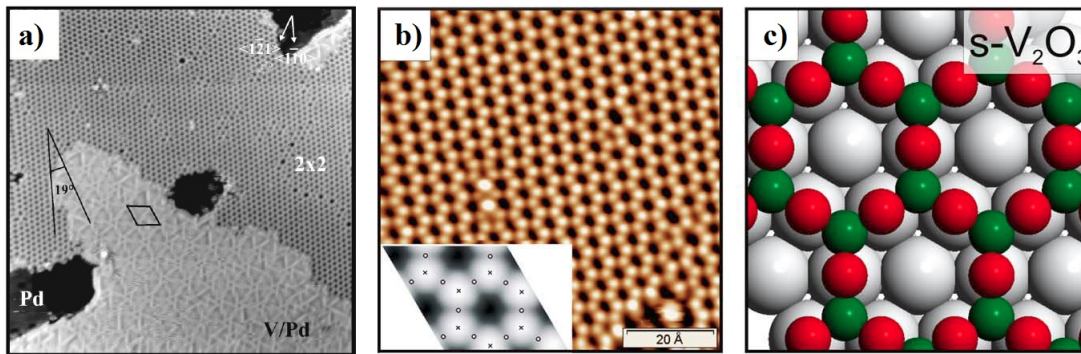


**Figure 2.17:** (a) STM image of 0.25 MLE  $\text{VO}_x/\text{Pd}(111)$  ( $30 \times 30 \text{ nm}^2$ ,  $V = 0.1 \text{ V}$ ,  $I = 1.0 \text{ nA}$ )<sup>[57]</sup>. (b) Atomically resolved STM image of the  $(2 \times 2)$ -surface- $\text{V}_2\text{O}_3/\text{Pd}(111)$  phase (0.5 MLE); the inset shows the STM simulation for the respective model. (c) Density functional theory (DFT) model of the phase shown in (b).<sup>[60]</sup>

## 2.5 Growth of $\text{TiO}_x/\text{Au}(111)$

In this section the current STM research studies on  $\text{TiO}_x/\text{Au}(111)$  will be highlighted in order to evidence some analogies or differences with the work presented here. Particularly, this section is focused on works in which a similar experimental procedure is carried out, i.e. deposition of Ti by thermal/electron-beam evaporation and subsequent oxidation; these will be reviewed in chronological order. Those which employ a different deposition method<sup>[63–65]</sup>, instead, will not be discussed in the following.

The first work we will consider is the one of Biener *et al.*<sup>[11]</sup>; the main purpose of this study was to synthesize and characterize titanium oxide nanostructures on the Au(111) surface and study their morphology at different coverages and annealing temperatures. The experimental procedure to obtain titanium oxide nanostructures consisted of two steps:

1. *e*-beam evaporation of Ti at room temperature (0.1 ML/min);
2. oxidation ( $5 \times 10^{-5}$  mbar for 200 s,  $\sim 10000$  L of exposure) at room temperature;

consequently, an annealing for 10 minutes at different temperatures (600 K, 900 K) was performed.

Figure 2.18 shows STM images of  $\text{TiO}_x/\text{Au}(111)$  at 0.1 MLE (a, b), 0.25 MLE (c) and 0.5 MLE (d). The image in Fig. 2.18(a) has been obtained after annealing at 600 K; with respect to the as-deposited conditions, the density of titanium oxide clusters is decreased. Fig. 2.18(b) shows that, after further annealing at 900 K, faceted three-dimensional  $\text{TiO}_x$  (with an apparent height of  $\sim 0.6$ – $1.2$  nm and a diameter of several nanometers) decorate both step edges and terraces; the inset, also, shows that the herringbone reconstruction of the Au(111) surface is disturbed in their proximity. Fig. 2.18(c) shows the appearance of the  $\text{TiO}_x/\text{Au}(111)$  system at 0.25 MLE (again after an annealing at 900 K): both 2D and 3D islands are present, either with triangular or hexagonal shape and with a typical feature size of  $\sim 5$  nm. Notably, the apparent height of 2D ones is bias-dependent. Fig. 2.18(d), instead, shows a STM image obtained at 0.5 MLE after the same annealing treatment; in this case, additional features appear, such as needle-like  $\text{TiO}_x$  crystallites, which decorate the step edges (inset I); hexagonal-shaped ones are close to step edges (inset II) and the apparent height of 3D ones is up to 2.5 nm (inset III).

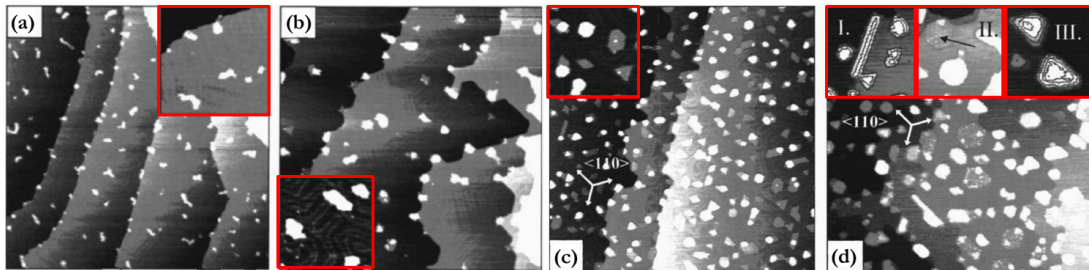


**Figure 2.18:** STM images of  $\text{TiO}_x$  deposited on Au(111) surface: (a) 0.1 MLE, after annealing at 600 K ( $200 \times 200 \text{ nm}^2$ ); (b) 0.1 MLE, after annealing at 900 K ( $160 \times 160 \text{ nm}^2$ ); (c) 0.25 MLE ( $200 \times 200 \text{ nm}^2$ ); (d) 0.5 MLE ( $160 \times 160 \text{ nm}^2$ ).<sup>[11]</sup>

The work of Potapenko *et al.*<sup>[10]</sup> has the aim to show that the synthesis of  $\text{TiO}_x$

nanostructures obtained by oxidizing a Ti-Au alloy brings superior results in terms of both greater nanoparticle structural homogeneity and narrower size distribution, compared with other methods, such as the post-annealing (the one of Biener *et al.*<sup>[11]</sup>, described above) and the so-called reactive-layer-assisted deposition (RLAD)<sup>[63,66]</sup>. The experimental procedure followed in this paper was:

1. thermal evaporation of Ti on Au(111) at room temperature (RT);
2. annealing at 900 K for 5';
3. oxidation (10', ~500 L) keeping the sample at 900 K.

Figure 2.19(a) shows an STM image of a 0.7 MLE  $\text{TiO}_x/\text{Au}(111)$  sample; it shows that most of the crystallites have either a triangular or hexagonal shape, with flat-top faces parallel to the surface, and that a reduction of 35% of the covered area is measured with respect to the same sample before the oxidation process. Measuring the height distribution in the reported image, the authors found a peak at 0.6 nm followed by others at the regular interval of 0.23 nm; this means that the lowest apparent height of the  $\text{TiO}_x$  crystallites is 0.6 nm, i.e. the first layer, then the following layers are 0.23 nm thick. On the basis of this height distribution and the overall hexagonal symmetry of the crystallites, the authors argued that stoichiometric  $\text{TiO}_2$  nAnocrystals were obtained, in the form of rutile with the (100) plane parallel to the surface; this holds for 95% of the islands. The remaining ones, on the other hand, are interpreted also as rutile  $\text{TiO}_2$ , but with a sort of 3D structure.

Figure 2.19(b), furthermore, shows the STS spectra collected over a set of crystallites and the Au(111) surface at 0.7 MLE. The crystallites'  $dI/dV$  curve shows a band gap in the electronic states very similar to the bulk rutile band gap value (about 3.0 eV); also, the center of this gap is shifted towards a negative sample bias, which is typical for an *n*-type semiconductor. Nevertheless, the Au(111) surface spectrum is significantly different from both the typical spectrum of this surface (see Figure 2.3(a)) and, moreover, to other spectra reported in the authors' own work; no explanation of this fact is accounted for.

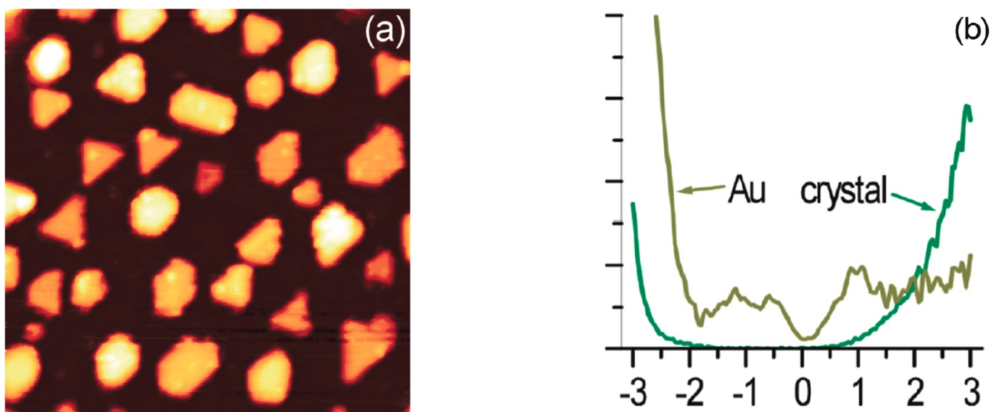


**Figure 2.19:** (a) STM image of Ti-Au surface alloy with 0.7 ML of Ti, oxidized in  $\text{O}_2$  at 900 K and cooled to RT ( $80 \times 80 \text{ nm}^2$ ). (b) Representative STS spectra ( $dI/dV$ ) recorded at various positions on the Au(111) surface and  $\text{TiO}_x$  crystallites.<sup>[10]</sup>

A deeper study of the  $\text{TiO}_x/\text{Au}(111)$  system has been performed by Wu and co-workers<sup>[12]</sup>, where various coverages have been investigated. Again the experimental procedure is slightly different from the previous cases:

1. *e*-beam evaporation of Ti;
2. annealing and simultaneous oxidation ( $p_{O_2} = 10^{-6}$  Pa, 600 °C,  $t = 30'$ ,  $\sim 20$  L);
3. cooling to RT at the same  $p_{O_2}$ .

STM investigation has been performed from 0 to 5 MLE showing the presence of a sequence of different phases: *honeycomb* (labeled as  $\beta$ , from 0.1 MLE), *triangular* ( $\gamma$ , from 0.6 MLE) and *pinwheel* ( $\delta$ , from 1.1 MLE). Figure 2.20(a), for example, shows the coexistence of these three phases at 1.1 MLE; the “spoke” and the unit cell of the pinwheel phase are rotated respectively by an angle  $\theta$  (approximately  $2^\circ$ ) and  $\phi$  (approximately  $13^\circ$ ) with respect to the honeycomb structure, which, conversely, is aligned with the crystallographic directions of the gold substrate.

From atomically resolved STM images and Auger electron spectroscopy (AES) data, the structural models for honeycomb and pinwheel phases (Fig. 2.20(b)-(c)) have been proposed; AES, notably, was employed in order to determine the stoichiometry of some of the  $TiO_x$  phases. The STM technique, indeed, is not sufficient alone to accomplish this task, since no information on the O atoms positions could be inferred in this study. The honeycomb phase (Fig. 2.20(b)) is made of a  $(2 \times 2)$  unit cell with  $5.9 \pm 0.3$  Å periodicity along the Au [110] direction; Ti atoms occupy the threefold *hollow* sites of the Au(111) substrate, while O atoms are located at the *bridging* sites of the Ti atoms; for this phase a  $Ti_2O_3$  stoichiometry is predicted. For the pinwheel phase, on the other hand, the STM images are interpreted as the result of a Moiré pattern formed by the superposition between a hexagonal Ti lattice (3.27 Å periodicity) and the Au(111) surface (2.89 Å periodicity). This model produces a  $(\sqrt{67} \times \sqrt{67})R12.2^\circ$  reconstruction (Fig. 2.20(c)); however, it lacks the oxygen atoms, since no AES spectrum of the pinwheel phase could be obtained, due to the simultaneous presence of the honeycomb and triangular phases. Concerning the triangular phase, furthermore, no atomic resolution could be obtained, so no structural model has been proposed, even if the stoichiometry of  $TiO_{1.3}$  has been determined (contrary to the  $TiO_2$  stoichiometry claimed by Potapenko *et al.*<sup>[10]</sup>). Finally, since Au is a nobler metal than Pt and Pd, no zigzag-like phase has been observed, on the contrary of the  $TiO_x/Pt(111)$  system<sup>[52,56]</sup> and the  $VO_x/Pd(111)$  one<sup>[59]</sup>; indeed, no Au–O–Ti stacking is possible, but only a Au–Ti–O one.

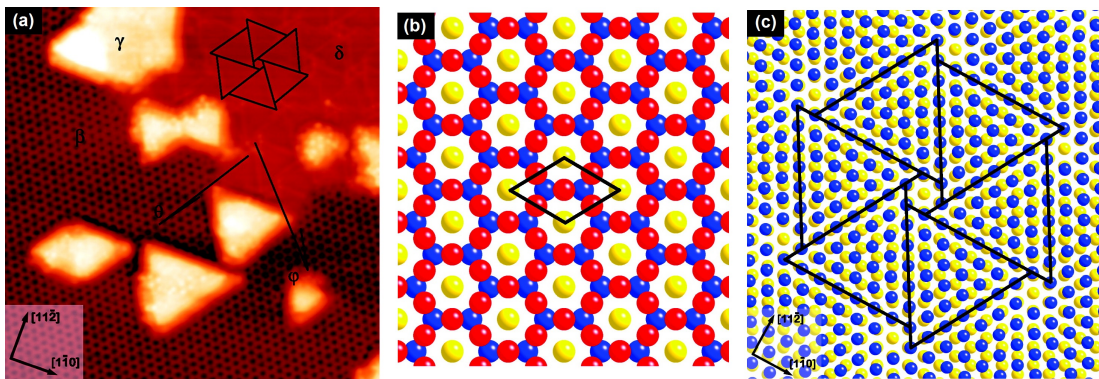


**Figure 2.20:** (a) STM image of a  $TiO_x$  surface with coexisting honeycomb, pinwheel and triangular structures (1.1 MLE,  $24 \times 24$  nm<sup>2</sup>,  $V = 0.98$  V,  $I = 0.20$  nA). (b) Atomic model for the honeycomb structure; the unit cell is indicated with a black rhombus (yellow = Au; blue = Ti; red = O). (c) Atomic model for the pinwheel structure (same colors as (b)), where Ti atoms are arranged in a rotated lattice on the Au(111) surface. The position of O atoms is not shown. The six triangles that make up the pinwheel are drawn on the image.<sup>[12]</sup>

It should be noted that, when speaking of the reconstruction of  $\text{TiO}_x$  phases on the Au(111) surface, it is assumed that no  $(22 \times \sqrt{3})$  reconstruction occurs under them (in fact the atomic models in Fig. 2.20 show the unreconstructed surface for Au(111)); this fact agrees with STM observations in which the herringbone reconstruction “avoids” the  $\text{TiO}_x$  islands at low coverage. In addition, the honeycomb phase has been recently observed also by Ragazzon *et al.*<sup>[65]</sup>, even if they deposited  $\text{TiO}_x$  nanostructures by means of a chemical vapor deposition method in UHV. Also in this case, the honeycomb phase exhibits a  $\text{Ti}_2\text{O}_3$  stoichiometry with a  $(2 \times 2)$  reconstruction, which is supported by LEED data.

The experimental works which have just been reviewed are affected by some incompleteness, since no systematic study on the morphological, structural and electronic properties of the system  $\text{TiO}_x/\text{Au}(111)$  had been performed. Only the work of Wu *et al.*<sup>[12]</sup> attempted to fulfill this challenge (without considering the electronic properties); however, the results obtained could not be “universal”, since the oxidation method is strongly influential on the final properties of the film, and a rigorous structural model of the observed phases still was absent.

In this framework, an experimental study on this system has been overtaken by the Micro and Nanostructured Materials Laboratory (Nanolab) of Politecnico di Milano (the same research laboratory under which the work presented here was performed) and a thesis work has been accomplished<sup>[13]</sup>. Not only  $\text{TiO}_x/\text{Au}(111)$  was considered, but also  $\text{Ti}/\text{Au}(111)$ , after which an article concerning this matter has been recently published<sup>[67]</sup>. The results obtained in the aforementioned thesis work will be now briefly resumed, since they represent both a development of the previous studies on this system and a starting point for the current thesis work.

The experimental procedure to obtain  $\text{TiO}_x/\text{Au}(111)$  is the following:

1. *e*-beam evaporation of Ti at room temperature (0.2 ML/min);
2. oxidation ( $p = 10^{-6}$  mbar,  $t = 8'$ , exposure  $\sim 500$  L) at room temperature;
3. annealing in UHV at 850 K for 15' (low coverage) or 20-25' (from 1 MLE).

Figure 2.21 represents a sort of overall view of the observed  $\text{TiO}_x$  phases: all the investigated coverage range is shown, both with “low”-magnification images (left column) and high-magnification ones (right column).

At low coverage (0.25 MLE, Fig. 2.21(a)-2.21(b)) triangular and polygonal  $\text{TiO}_x$  islands are formed (one layer thick) and they are disorderly arranged on the surface; in addition, some of them decorate the step edges of the substrate. Higher magnification STM images (Fig. 2.21(b)) show that polygonal crystallites simply result from the cohesion of the triangular ones, which act as “elementary units”. The latter can also appear isolated and with different dimensions: their side length goes from  $\sim 2.6$  nm to  $\sim 5$  nm. The Au(111) surface reconstruction, then, is perturbed so that the ridges tend to avoid the  $\text{TiO}_x$  islands and surround them. In addition, it was observed that the apparent height and the contrast of these crystallites is not always the same, so the influence of the applied bias and/or the apical atom of the STM tip was considered as a reasonable explanation of this effect.

At slightly higher coverage (0.4 MLE, Fig. 2.21(c)-2.21(d)), crystallites have an increased average size and some of them coalesce. Figure 2.21(d) confirms this size increase and shows that most of them assume a hexagonal shape. Over them, triangular structures arise and by analyzing topographic profiles, similarly as in the

inset in Fig. 2.21(d), their height is found to be independent on the experimental setup and equal to  $0.45 \pm 0.02$  nm (whereas the apparent height of the first-layer islands is  $\sim 0.2$  nm). Measurements as the aforementioned one show that these crystallites never directly grow on the Au(111) surface and they are really a second-layer phase, logically called *triangular* phase, as in the work of Wu *et al.*<sup>[12]</sup> The first-layer phase, instead, can be identified with high-resolution STM images: it is made up of several triangular units merged together and it has the appearance of the *pinwheel* phase, being qualitatively comparable to literature observations.<sup>[12,52,54,57]</sup>

At the intermediate coverage of 0.65 MLE (Fig. 2.21(e)-2.21(f)), pinwheel crystallites grow in size and coalesce until the substrate surface is almost uniformly covered; notably, the coalescence phenomenon can occur independently from the presence of Au(111) steps. Fig. 2.21(f) better shows the coalescence of the pinwheel phase, over which other triangular crystallites grow, as well as amorphous ones. Even in this case, a dependence on the experimental conditions of the pinwheel apparent height was observed.

The highest investigated coverage was 1.5 MLE. Fig. 2.21(g) shows that the surface is almost fully covered with one layer of  $\text{TiO}_x$  film, on which different structures grow: small triangular islands, large irregular islands and needle-shaped structures (rarely observed). Fig. 2.21(h), in addition, reveals the presence of new phases: apart from the already mentioned pinwheel (labeled with the letter “p”) and triangular (“t”), honeycomb (“h”) and row (“r”) appear; this figure shows also that some portions of the Au(111) surface remain uncovered. The *honeycomb* phase appears almost identical to the one observed by Wu *et al.*<sup>[12]</sup>, but it comes into view at higher coverage (only after 0.8 MLE) and after the pinwheel phase. The so-called *row* phase, instead, had not been observed before for this system. Pinwheel and honeycomb are first-layer structures, whereas triangular and row phases grow over them. In addition, an irregular second-layer island with unclear structure is present and it is labeled with a question mark.

Atomic resolution images for most of the observed phases have been obtained. For the pinwheel phase, Figure 2.22(a) shows this kind of STM image at 1.5 MLE, in which the unit cell is shown. The measured periodicity is  $3.2 \pm 0.15$  nm, whereas the measured interatomic distance is  $3.2 \pm 0.2$  Å. This image was recorded at positive bias, so the most common interpretation<sup>[9]</sup> suggests that tunneling mainly occurs from the tip occupied states to the *3d* empty states of titanium, so that the image should represent the atomic corrugation related to the Ti LDOS. Conversely, at negative bias one may expect to visualize oxygen atoms, but atomic resolution in this condition could not be obtained, so no information about the location of O atoms could be inferred. Nonetheless, an atomic model for this phase was proposed (Fig. 2.22(b)): it is based on a Moiré pattern (similarly as the model of Wu *et al.*<sup>[12]</sup>) in which a  $(\sqrt{133} \times \sqrt{133})R17.5^\circ$  reconstruction on the Au(111) surface is obtained. This was calculated comparing it with atomically resolved STM images in order to get a good agreement with the experimental data. Since no information on oxygen atoms could be obtained, only Au and Ti atoms are represented, and the Ti–Ti interatomic distance in this model is 3.37 Å, whereas a periodicity of 3.2 Å is found. However, this model suffers from the same limitations as the one suggested by Wu *et al.*<sup>[12]</sup> the reason why coincidence sites are imaged dark is still unclear and a theoretical atomistic simulation was not available.

Considering now the honeycomb phase, Figure 2.23(a) shows an atomically resolved STM image, on the left, and two line profiles taken on it, on the right (Fig. 2.23(b) and Fig. 2.23(c)). This phase shows an apparent height of  $0.09 \pm 0.01$  nm with respect to

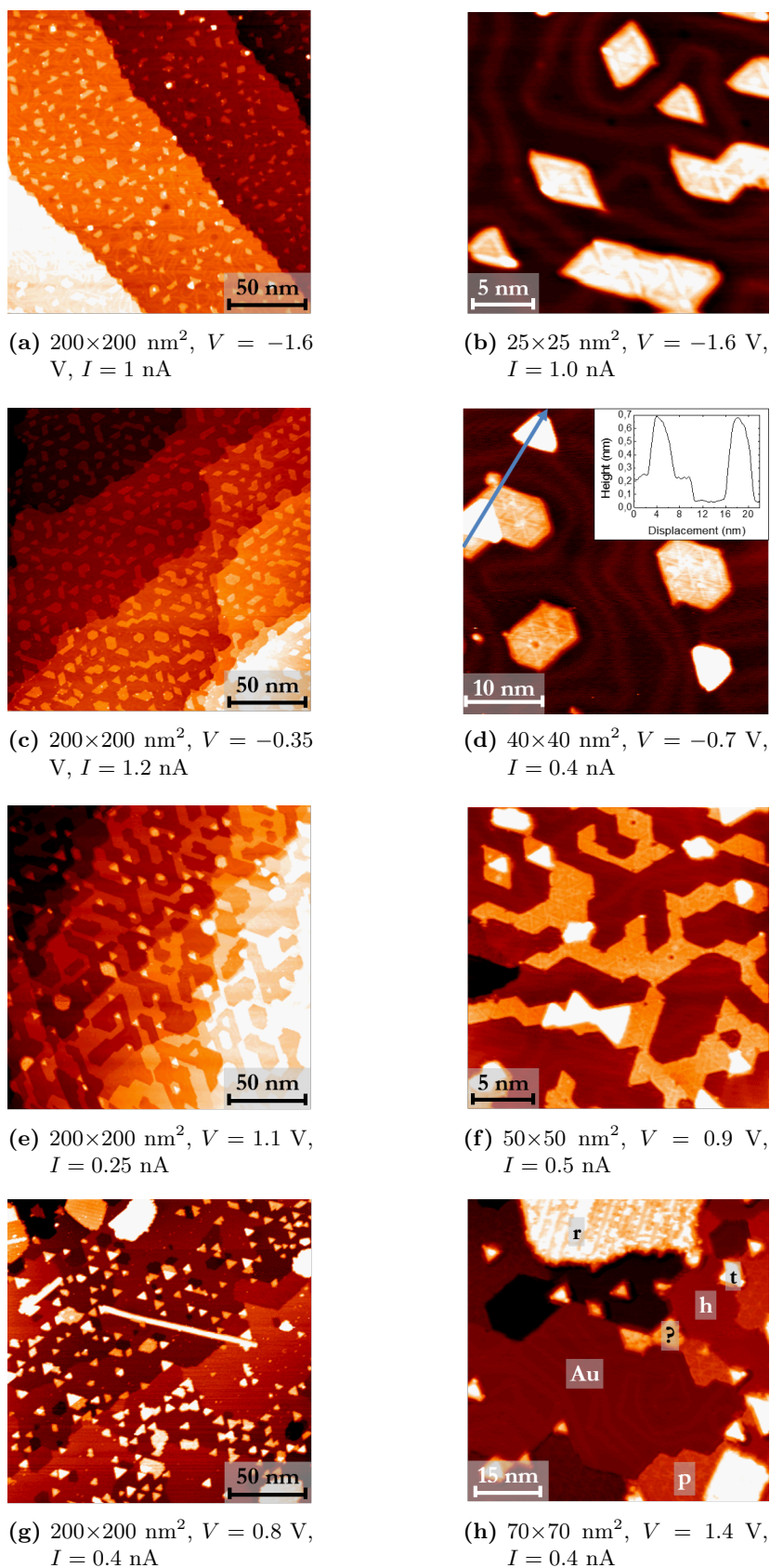


**Figure 2.21:** STM images of  $\text{TiO}_x/\text{Au}(111)$  at increasing coverage. (a) and (b): 0.25 MLE; (c) and (d): 0.4 MLE; (e) and (f): 0.65 MLE; (g) and (h): 1.5 MLE.<sup>[13]</sup>

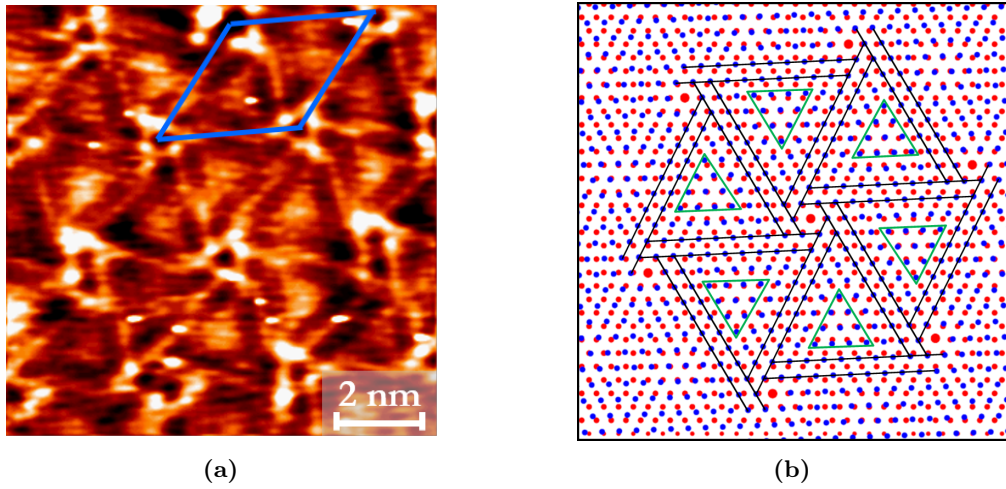


**Figure 2.22:** (a) Atomic resolution STM image of the pinwheel phase (1.5 MLE,  $10 \times 10 \text{ nm}^2$ ,  $V = 0.1 \text{ V}$ ,  $I = 1.5 \text{ nA}$ ). (b) Structural model of this phase based on a Moiré pattern (red = Au, blue = Ti). Bigger red atoms represent coincidence sites and the geometry of this phase is highlighted; atoms into the green triangles are in *quasi-coincidence* positions, so these regions appear brighter in STM images.<sup>[13]</sup>

the substrate; from the structural point of view, it has a hexagonal symmetry, the unit cell vector is  $6.8 \pm 0.2 \text{ \AA}$  long (Fig. 2.23(c)) and an interatomic distance of  $4.7 \pm 0.2 \text{ \AA}$  was found (Fig. 2.23(b)). An angle of  $19^\circ \pm 1^\circ$  with respect to the pinwheel phase is also observed. For this phase, no structural model was proposed, since a discrepancy with the model of Wu *et al.*<sup>[12]</sup> was found: the greater values of periodicity ( $6.8 \pm 0.2 \text{ \AA}$  against  $5.9 \pm 0.3 \text{ \AA}$ ) and interatomic distance ( $4.7 \pm 0.2 \text{ \AA}$  against  $\sim 3.3 \text{ \AA}$ ) were not consistent with an exact  $(2 \times 2)$  reconstruction. This discrepancy might have been due to an uncertainty in the measurements due to a *drift* effect; however, a mismatch between the honeycomb lattice and the substrate's was considered possible and could not be excluded *a priori*.

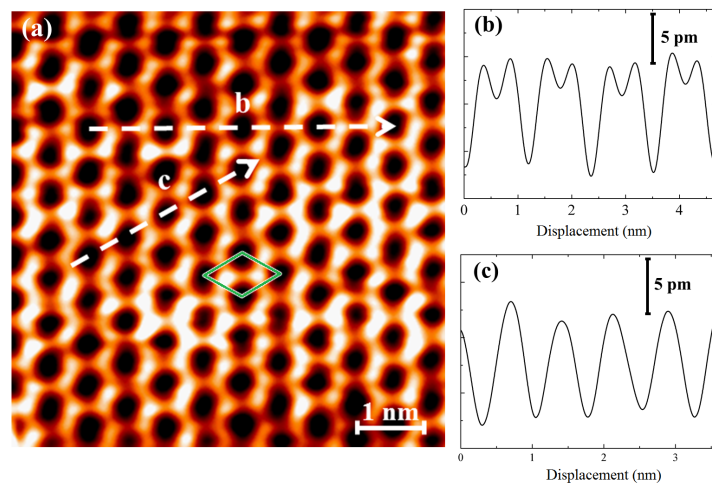


**Figure 2.23:** (a) Atomic resolution STM image of the honeycomb phase, where the unit cell is highlighted ( $1.5 \text{ MLE}$ ,  $7 \times 7 \text{ nm}^2$ ,  $V = 0.6 \text{ V}$ ,  $I = 0.2 \text{ nA}$ ). (b) Topographic profile along the “b” arrow of (a). (c) Topographic profile along the “c” arrow of (a).<sup>[13]</sup>

The triangular phase appears in the form of crystallites as in Figure 2.24. In the sub-monolayer regime their height is generally 0.45 nm, with sides of 5 nm; at higher coverage, however, larger islands can exist and some of them reach the height of 0.75 nm. This fact, together with high-resolution observations (as in Fig. 2.24), led to the hypothesis of a layered structure for the triangular crystallites, so that the bigger islands may be formed by one layer ( $\sim 0.3$  nm thick) more than the smaller ones. In addition, the apparent height with respect to the honeycomb phase is 0.6 nm, a different value from the one calculated over the pinwheel phase. However, for this phase no atomic resolution could be achieved, nor a structural model was available, so all the aforementioned observations have not been thoroughly explained.

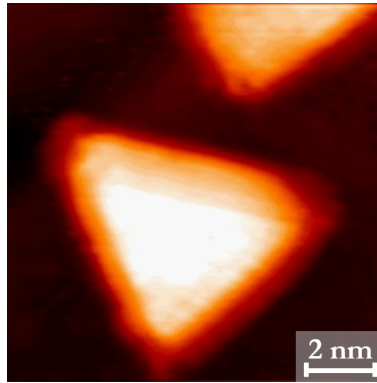


**Figure 2.24:** STM image of a triangular island ( $11 \times 11$  nm<sup>2</sup>,  $V = 0.2$  V,  $I = 1.5$  nA).<sup>[13]</sup>

The row phase, finally, usually appears in the form of relatively extended islands (with dimension of 20–40 nm, as in Fig. 2.21(g)-2.21(h)), which are made of more than one layer, each one 0.25 nm thick. On their surface, parallel lines can be observed, with the alternation of brighter ones and darker ones. These can have different directions, forming angles of  $\pm 60^\circ$ , and different orientational domains can be present in a single island. Very high resolution could be achieved (Figure 2.25(a)) and each line was found to be made of two parallel rows of atoms. The interatomic distance along a single row (Fig. 2.25(b)) was found to be  $5.5 \pm 0.1$  Å. Also in this case, no structural model was available.

From the analysis of the state of the art of this system, it emerges that, to this author's knowledge, no STS studies have been performed yet (at least, considering  $\text{TiO}_x/\text{Au}(111)$  obtained with the evaporation method). In addition, the morphological and structural analysis is not complete: atomic models have not been built for all the phases. Moreover, LEED experiments have been performed only in a preliminary way.

## 2.6 Thesis objectives

In light of the considerations that have been shown up to this point, it is possible to define in detail the objectives of the work presented in this thesis. Since this work is contiguous with the previous thesis one<sup>[13]</sup>, on the one hand it aims to both a morphological and structural study on the  $\text{TiO}_x$  phases; some of them still have not been observed at atomic resolution; notably, the row phase has been observed with a very high resolution, close to the atomic one, but this does not hold for the needle-like phase (observed only in low-magnification images) and for the triangular one. In

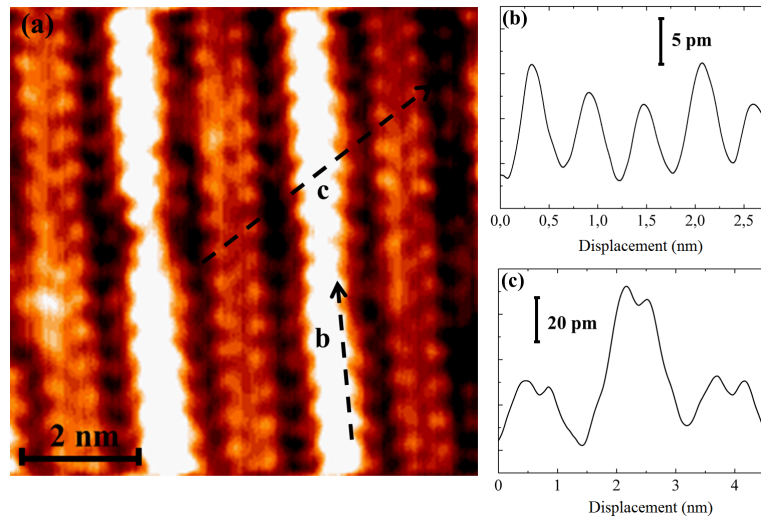


**Figure 2.25:** (a) High resolution STM image of the row phase (1.5 MLE,  $8 \times 8 \text{ nm}^2$ ,  $V = 0.7 \text{ V}$ ,  $I = 0.5 \text{ nA}$ ). (b) Topographic profile along the line “b” of (a). (c) Topographic profile along the line “c” of (a).<sup>[13]</sup>

addition, structural models for almost all the phases are needed (the one for the pinwheel phase should be confirmed at least). On the other hand, the other main objective is the STS study for the whole  $\text{TiO}_x/\text{Au}(111)$  system at different coverage, mainly in the sub-monolayer regime and at relatively high coverage (namely 1.5 MLE).

In order to pursue these goals, the employed techniques are scanning tunneling microscopy (STM), scanning tunneling spectroscopy (STS) and low-energy electron diffraction (LEED).

## Experimental results

In this chapter the experimental results will be presented and discussed. After the description of the experimental procedure (Section 3.1), the second section (3.2) describes the structural properties of the observed  $\text{TiO}_x/\text{Au}(111)$  phases, starting with the low-energy electron diffraction (LEED) analysis and considering also the presence of adsorbates. The third section (3.3) is focused on the scanning tunneling spectroscopy (STS) study of the system, starting with a general procedure to explain the data collection for this analysis and considering both the  $\text{Au}(111)$  surface and four  $\text{TiO}_x$  phases of the five observed ones. Finally, the obtained results will be summarized and discussed (Section 3.4).

### 3.1 Experimental procedure

The experiments were performed in a ultra-high vacuum (UHV) chamber (base pressure  $\sim 5 \times 10^{-11}$  mbar) equipped with an *Omicron VT-SPM* system, a low-energy electron diffraction (LEED) device, an Auger electron spectroscopy (AES) device and standard facilities for sample preparation. The  $\text{Au}(111)$  surface, either from a single crystal or a  $\text{Au}/\text{mica}$  sample, was cleaned and prepared in UHV by 15 minutes  $\text{Ar}^+$  sputtering at 1 KeV at a sample temperature of 850 K, which was kept for at least 30' after sputtering. After this procedure, a preliminary STM observation of the clean surface was performed, in order to exclude contaminations and check the quality of the  $(22 \times \sqrt{3})$  reconstruction. Titanium was deposited by means of electron-beam evaporation (Ti wire purity 99.99%) on the clean  $\text{Au}(111)$  surface at room temperature (RT). The deposition rate (about  $3.3 \times 10^{-3}$  ML/s or 0.2 ML/min) was controlled by monitoring the ion flux from the evaporator; titanium coverage was varied from 0.25 ML up to 1.5 ML. After that, to synthesize titanium oxide, the preparation chamber was filled with oxygen up to the pressure of  $10^{-6}$  mbar by means of a high-precision valve (*leak valve*); the sample, so, was exposed to  $\text{O}_2$  for 8' at RT, which corresponds to the exposure of  $\sim 500$  L. Finally, the sample was annealed at 850 K for 15' for Ti coverage up to 1 ML and for 25' for higher coverage.

STM measurements were performed at constant current mode at room temperature (if not, the temperature is specified). The  $dI/dV$  signal was acquired at  $\sim 110$  K, using a liquid nitrogen cooling system, by means of a lock-in amplifier applying a modulation

of 40 mV at the frequency of 8 kHz;  $dI/dV$  maps were acquired with a closed feedback loop, whereas STS spectra were locally recorded simultaneously with  $I(V)$  curves (in the same points) with an open feedback loop. At least three STS spectra were recorded at each point of interest for consistency. To discriminate the influence of the tip in spectroscopic measurements, bulk W and Cr tips were employed; they were prepared with an electrochemical process, as described in Appendix A.3 and in Ref. [68] (for Cr tips). In order to extract the local density of states (LDOS) information from the  $dI/dV$  curves, we first applied a proper normalization to the spectra<sup>[69]</sup>; more details about this procedure are reported in Sub-section 3.3.1. Among the different possibilities, the method discussed by Ukraintsev *et al.*<sup>[30]</sup> was chosen for the reasons that will be explained in Sub-section 3.3.1.

## 3.2 Morphology and structure

### 3.2.1 LEED analysis

At the beginning of my thesis work, a low-energy electron diffraction (LEED) analysis has been performed by my research group in order to determine the structure of some of the  $\text{TiO}_x/\text{Au}(111)$  phases. The measurements and analysis were not performed by me, but they are presented here since they have let us confirm (or rectify) the hypotheses on the atomic structure of the observed phases. As a premise, it should be noted that, generally speaking, a LEED pattern corresponds to the superposition of the single patterns of each phase in the first atomic layers; this means that, at high coverage, a rather complex pattern corresponding to both the honeycomb and pinwheel phases is expected. The other  $\text{TiO}_x$  phases (triangular, row and especially needle) are not expected to give any contribution, since their quantity, compared with the first-layer phases (pinwheel and honeycomb), is quite lower.

Figure 3.1 shows the evolution of the LEED pattern during  $\text{TiO}_x$  deposition, from low to high coverage. More precisely, Fig. 3.1(a) shows the LEED pattern corresponding to the clean  $\text{Au}(111)$  surface and it exhibits a hexagonal symmetry, which is typical for a (111)-oriented surface of a FCC structure. The pattern, in addition, reveals the multiple satellite spots characteristic of the  $\text{Au}(111)(22 \times \sqrt{3})$  herringbone reconstruction<sup>[70]</sup> (marked with a yellow box). When  $\text{TiO}_x$  is present on the  $\text{Au}(111)$  surface, in the sub-monolayer regime (Fig. 3.1(b)), these satellite spots disappear and the formation of other features nearby the substrate ( $1 \times 1$ ) can be observed (highlighted with a red box). At higher coverage (1.5 MLE, Fig. 3.1(c)), these features appear sharper (marked with a red square) and the pattern becomes more complex; in fact, as already mentioned, a superposition between the patterns corresponding to both the honeycomb and pinwheel phases appear. Indeed, in Fig. 3.1(c), other spots arise, with rather low intensity, around the center of the image and, with higher intensity, additional spots between the ( $1 \times 1$ ) ones appear (marked with a cyan square). Some segments have been drawn to clarify the presence of all these different spots: the yellow-colored AB line links two ( $1 \times 1$ ) spots and the cyan-colored CD dashed line links two lower intensity spots to each other.

The assignment of these spots to their corresponding phase (pinwheel and honeycomb) was performed with a geometrical argument and on the strength of STM observations. Indeed, the ratio between CD and AB is 1/2 (the same occurs for other equivalent segments) and they are aligned, so this means that these spots correspond

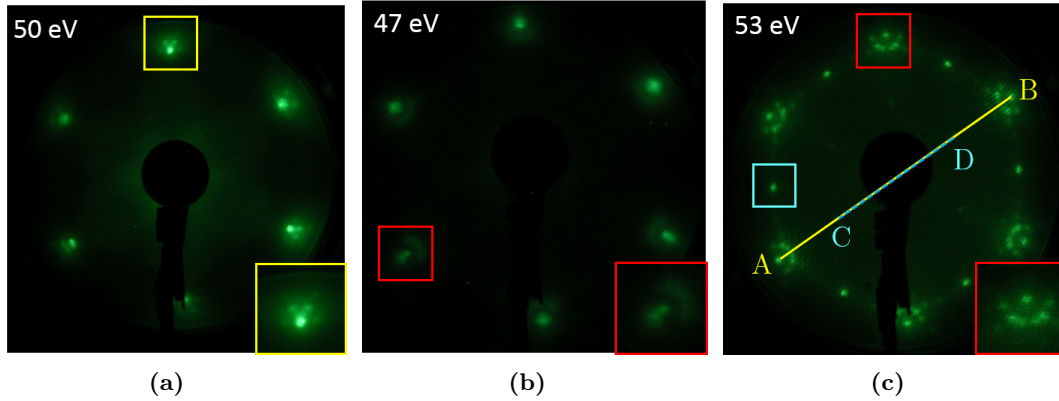


**Figure 3.1:** LEED patterns of the  $\text{TiO}_x/\text{Au}(111)$  system at increasing coverage; the insets show magnifications of the highlighted spots. (a) Clean Au(111) surface; (b) 0.5 MLE; (c) 1.5 MLE. The primary energy is reported on each image.

to a unrotated  $(2 \times 2)$  reconstruction, which belongs to the honeycomb phase, for which this reconstruction was previously hypothesized<sup>[12,13]</sup>. The spot highlighted with a cyan square and the other equivalent ones, in addition, represent the second-order diffraction pattern of the  $(2 \times 2)$  superstructure; this was also verified through analogous measurements. A freeware program for LEED simulations (LEEDpat) was employed to obtain a simulation of the  $(2 \times 2)$  LEED pattern and the results perfectly agree with the measured one (as in Figure 3.2).

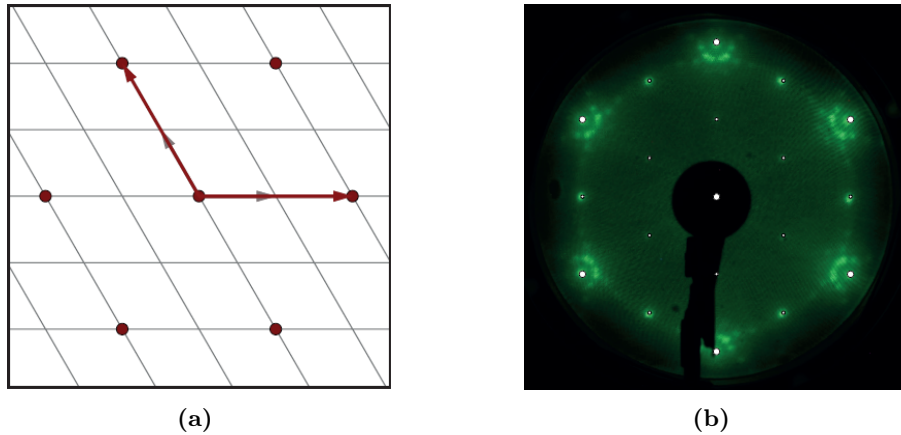


**Figure 3.2:** Simulated LEED for the honeycomb phase. (a) Real space lattice. (b) Reciprocal space image superimposed with the measured LEED pattern; larger spots belong to the Au(111) substrate, while smaller ones to the overlayer.

Concerning the features in the neighborhood of the  $(1 \times 1)$  spots, which were ascribed to the pinwheel phase, the situation is less straightforward, but the same criterion can be applied: calculating the ratio between suitable segments and the angle between them (of course this was repeated for several points) and inserting these values in the same program, considering a commensurate superstructure growing on a substrate with  $p6m$  symmetry<sup>a</sup>, the following rotation matrix was obtained:

<sup>a</sup>See Sub-section 2.4.1 for the definition of the pinwheel phase.

$$\begin{bmatrix} 12 & 4 \\ 8 & 12 \end{bmatrix}$$

In the Wood notation, this corresponds to a  $(\sqrt{111} \times \sqrt{111})R19.1^\circ$  reconstruction. This value is slightly different from the previous  $(\sqrt{133} \times \sqrt{133})R17.5^\circ$  obtained without the aid of LEED measurements<sup>[13]</sup>. Figure 3.3, indeed, shows the results of the simulated LEED pattern, which clearly agrees with the measured one.

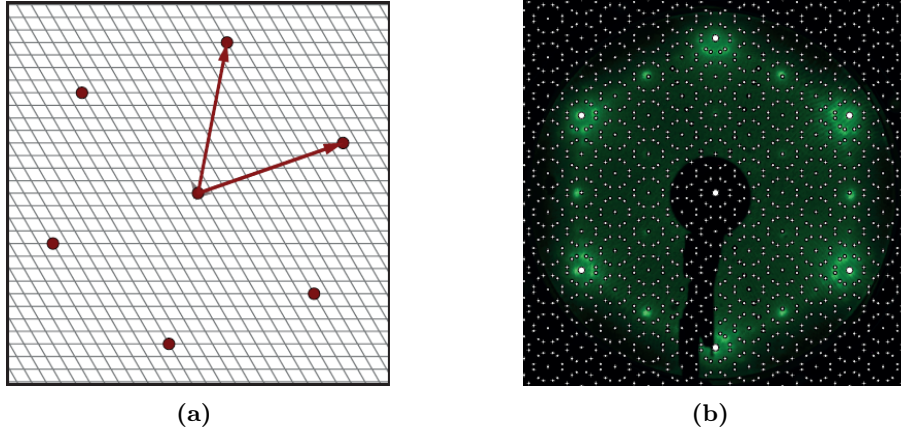


**Figure 3.3:** Simulated LEED of the pinwheel phase. (a) Real space superstructure. (b) Reciprocal space image superimposed with the measured LEED pattern.

### 3.2.2 Atomic structure of $\text{TiO}_x$ phases

The STM observations of the  $\text{TiO}_x/\text{Au}(111)$  system have confirmed the ones reported in the previous thesis work<sup>[13]</sup>, which have been described in the previous chapter (Section 2.5). Figure 3.4 shows an overview of the STM measurements at low and high coverage. More precisely, Figs. 3.4(a) and 3.4(b) illustrate the low coverage regime: polygonal crystallites of the pinwheel phase, made of jointed triangular units, grow on the  $\text{Au}(111)$  surface, which shows a perturbed herringbone reconstruction; in addition, triangular crystallites grow on top of the pinwheel ones, as well as less ordered clusters, which may be due to some impurities. It should be noted, indeed, that the value of 0.4 MLE for the appearance of the triangular phase is mainly an approximate threshold and, occasionally, they may appear at lower coverage.

On the other hand, Figures 3.4(c) to 3.4(f) show STM images at high coverage ( $\geq 1$  MLE). Fig. 3.4(c), notably, shows a “low”-magnification image, where all the known  $\text{TiO}_x/\text{Au}(111)$  phases appear (pinwheel, honeycomb, triangular, row and needle); in this case, also, no clean  $\text{Au}(111)$  areas are present. Fig. 3.4(d), on the other hand, shows some atomic terraces of honeycomb and pinwheel phases, on which triangular crystallites grow, as well as a row one; the latter, notably, exhibits the presence of two different domains with a relative rotation of  $120^\circ$ . It should be pointed out that this image, as the one in Fig. 3.4(f), has been filtered in order to increase the surface corrugation. Indeed, Fig. 3.4(f) derives from Fig. 3.4(e) and they show the presence of a pinwheel layer, a region of uncovered  $\text{Au}(111)$  surface and row phase crystallites. More precisely, the  $\text{Au}(111)$  surface exhibits the well-known ridges of the herringbone

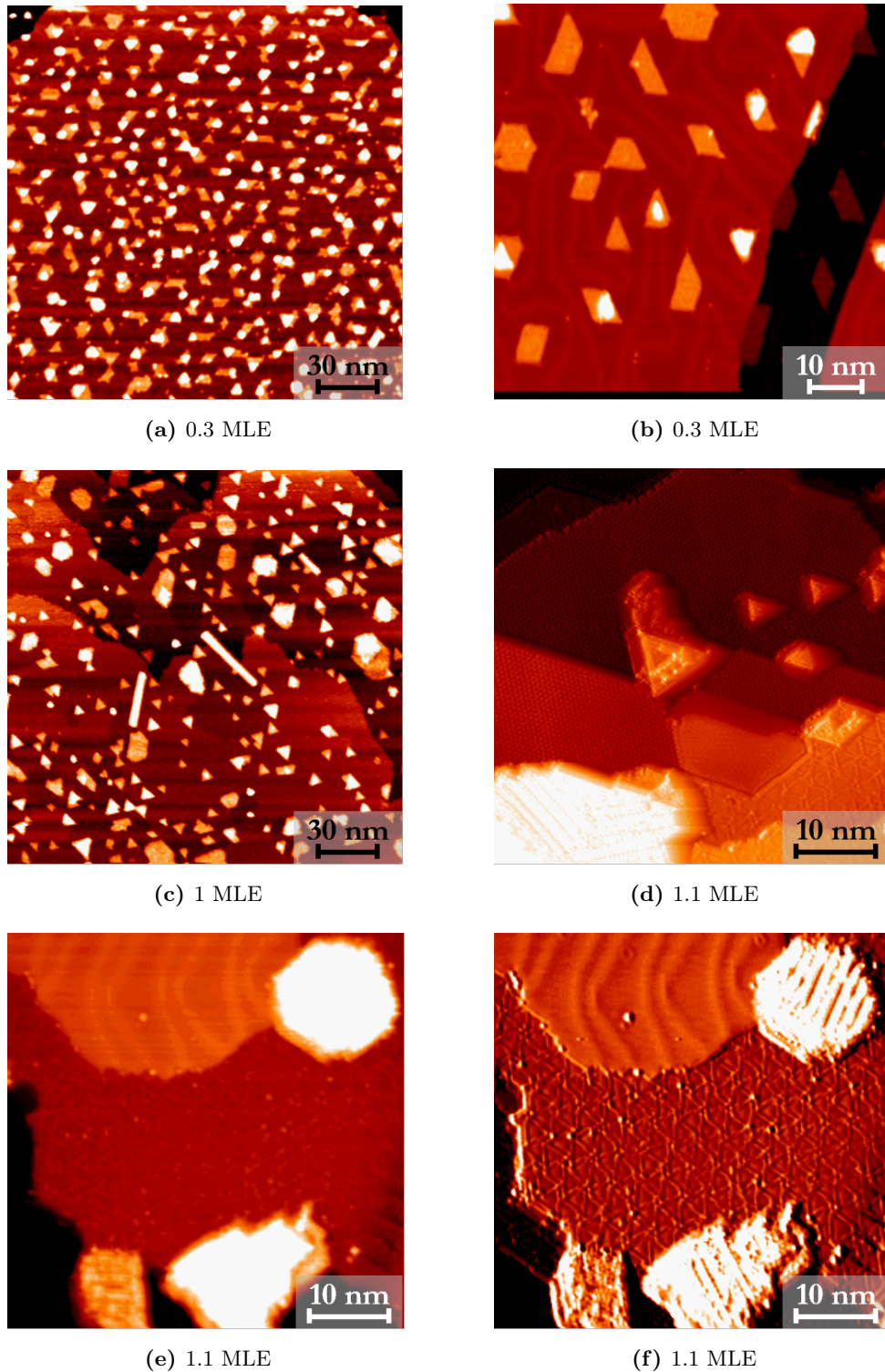


**Figure 3.4:** STM images of  $\text{TiO}_x/\text{Au}(111)$  at low (a,b) and high (c-f) coverage; images (d) and (f) have been filtered in order to highlight the surface corrugation. (a) 0.3 MLE, W tip ( $200 \times 200 \text{ nm}^2$ ,  $V = -0.81 \text{ V}$ ,  $I = 0.36 \text{ nA}$ ). (b) 0.3 MLE, W tip ( $75 \times 75 \text{ nm}^2$ ,  $V = 1 \text{ V}$ ,  $I = 0.38 \text{ nA}$ ). (c) 1 MLE, Cr tip ( $200 \times 200 \text{ nm}^2$ ,  $V = 0.97 \text{ V}$ ,  $I = 0.60 \text{ nA}$ ,  $T = 110 \text{ K}$ ). (d) 1.1 MLE, W tip ( $50 \times 50 \text{ nm}^2$ ,  $V = 1.12 \text{ V}$ ,  $I = 0.22 \text{ nA}$ ). (e) 1.1 MLE, W tip ( $50 \times 50 \text{ nm}^2$ ,  $V = 1 \text{ V}$ ,  $I = 0.29 \text{ nA}$ ). (f) Same image as (e), filtered as described above.

reconstruction (deviated from their usual path), as well as the presence of some “holes”, which also were observed in the previous thesis work<sup>[13]</sup>; in the lower-left side of the image, in addition, a cluster with unclear structure is present.

In the following paragraphs, the analysis of the atomic structure of the  $\text{TiO}_x$  phases will be elucidated, with the assistance of atomically resolved STM images.

### Honeycomb

The atomic structure of the honeycomb phase had already been observed in the previous thesis work<sup>[13]</sup>; in that case, a discrepancy from the work of Wu *et al.*<sup>[12]</sup> emerged: indeed, a greater periodicity ( $6.8 \pm 0.2 \text{ \AA}$  against  $5.9 \pm 0.3 \text{ \AA}$ ) and a greater interatomic distance ( $4.7 \pm 0.2 \text{ \AA}$  against  $\sim 3.3 \text{ \AA}$ ) were found, thus leading to a non exact correspondence with a  $(2 \times 2)$  reconstruction (this was already mentioned in Section 2.5). Performing new measurements at room temperature, an approximate average value of  $6.3 \text{ \AA}$  for the periodicity was found, which is closer to the one measured by Wu *et al.*<sup>[12]</sup>; in addition, slightly different values of the periodicity, depending on the direction, were measured in the same image, in several cases. Based on these observations, we can conclude that our measurements are probably affected by drift effects, which can be only approximately adjusted. We can conclude that an error of  $\pm 0.5 \text{ \AA}$  is plausible and that our measurements are not in contrast with the one of Wu *et al.*<sup>[12]</sup>. Anyway, as mentioned in Sub-section 3.2.1, LEED measurements show a clear evidence of a  $(2 \times 2)$  reconstruction, which dispels any doubt about the superstructure of the honeycomb phase.

Figure 3.5 shows high-resolution STM images of the honeycomb phase. Notably, Fig. 3.5(a) shows an atomically resolved STM image in which the unit cell is highlighted and, also, the atomic model is displayed. Here, we have adopted the same model proposed by Wu *et al.*<sup>[12]</sup>: the unit cell contains two Ti atoms forming a honeycomb lattice and three O atoms forming a *kagomé* pattern, with the latter as the topmost layer. The stoichiometry resulting by this stacking, thus, is  $\text{Ti}_2\text{O}_3$ , with a  $\text{Ti}^{3+}$  formal oxidation state. Figures 3.5(b) and 3.5(c) show the effect of a change in the applied bias: Fig. 3.5(b) was acquired at negative bias ( $-1 \text{ V}$ ) and Fig. 3.5(c) at nearly-zero bias ( $\sim 0.1 \text{ V}$ ); notably, the latter has an unusual appearance, analogous to the  $dI/dV$  map (not shown). Finally, Fig. 3.5(d) shows that, under peculiar conditions, the honeycomb phase revealed a different structure, the *kagomé* one, as observed for the system  $\text{TiO}_x/\text{Pt}(111)$  (which has been already highlighted in Sub-section 2.4.1). This effect has been observed only in one experimental session at  $0.3 \text{ V}$ , so this seems reasonably an occasional manifestation; however, it may be considered as a proof of the previously explained structural model. Nonetheless, it seems quite unrealistic to ascribe bright protrusions in Fig. 3.5(d) to oxygen atoms, since in theory they should be imaged at negative bias. More probably, this kind of STM image is due to a unique tip apex structure and/or density of states. In order to investigate the nature of this contrast, density functional theory (DFT) calculations are required; indeed, they are currently being performed.

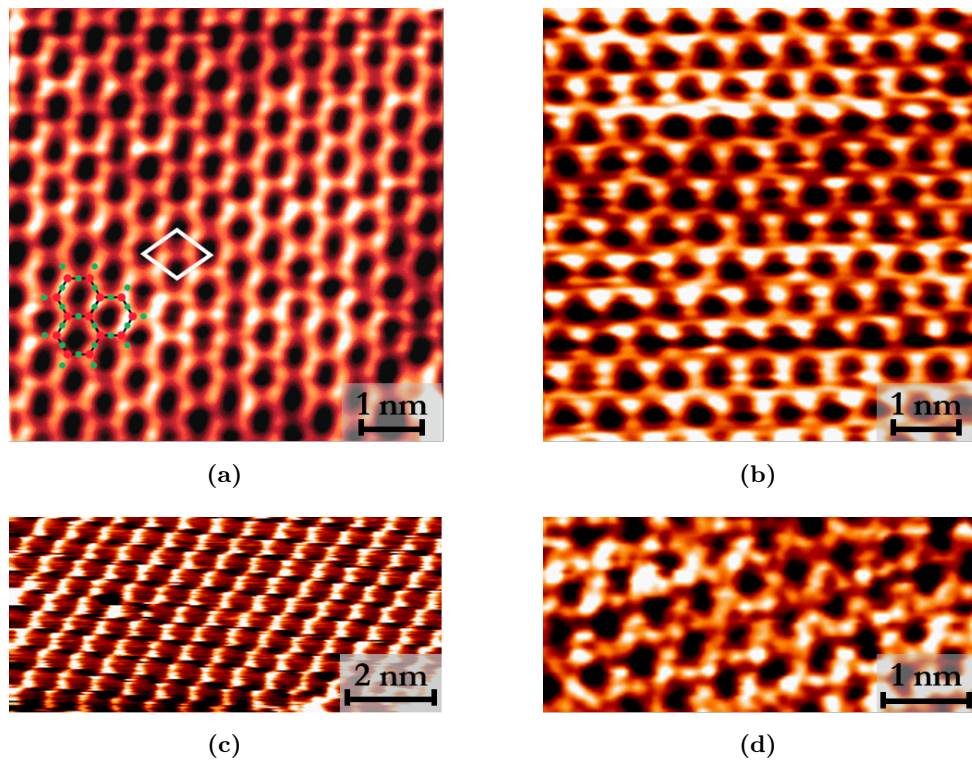


**Figure 3.5:** (a) Atomically resolved STM image (1.3 MLE,  $7 \times 7 \text{ nm}^2$ ,  $V = 0.6 \text{ V}$ ,  $I = 0.2 \text{ nA}$ ); the unit cell is highlighted with a white rhombus and the atomic model is reported (red = Ti; green = O). (b) High-resolution STM image at negative bias (1.1 MLE, W tip,  $6.67 \times 6.67 \text{ nm}^2$ ,  $V = -1 \text{ V}$ ,  $I = 0.31 \text{ nA}$ ). (c) High-resolution STM image at nearly-zero bias (1.1 MLE, W tip,  $10 \times 10 \text{ nm}^2$ ,  $V = 0.09 \text{ V}$ ,  $I = 1.7 \text{ nA}$ ,  $T = 110 \text{ K}$ ). (d) Atomically resolved *kagomé* appearance (1.3 MLE, W tip,  $3.33 \times 2.25 \text{ nm}^2$ ,  $V = 0.3 \text{ V}$ ,  $I = 0.7 \text{ nA}$ ,  $T = 110 \text{ K}$ ).

### Pinwheel

As mentioned at the beginning of this section, at low coverage the pinwheel phase appears as polygonal crystallites made of several jointed triangular units. In some cases, these crystallites have the form of a single pinwheel, made of six jointed triangles: this is shown in atomically resolved STM images, such as in Figs. 3.6(a)-3.6(b), where the second image was graphically filtered to enhance the surface corrugation. On the other hand, at high coverage, it forms a continuous film, wetting the Au(111) surface. The atomically resolved STM image in Fig. 3.6(c) reports the unit cell, which was obtained by linking the periodicity sites to each other. In Sub-section 3.2.1 we have mentioned that, for the pinwheel phase, the  $(\sqrt{111} \times \sqrt{111})R19.1^\circ$  reconstruction was found. However, this is not enough to build an atomic model; indeed, assuming the formation of a Moiré pattern, we need the Ti-Ti interatomic distance and the angle between the two layers ( $\theta$ ). Following the argumentation of Wu *et al.*<sup>[12]</sup>, we can write the equation which expresses the condition of coincident points for the two lattices<sup>[71]</sup>:

$$\begin{pmatrix} s & \frac{1}{2}s \\ 0 & \frac{\sqrt{3}}{2}s \end{pmatrix} \begin{pmatrix} h \\ k \end{pmatrix} = \begin{pmatrix} \cos \theta & -\sin \theta \\ \sin \theta & \cos \theta \end{pmatrix} \begin{pmatrix} a & \frac{1}{2}a \\ 0 & \frac{\sqrt{3}}{2}a \end{pmatrix} \begin{pmatrix} m \\ n \end{pmatrix} \quad (3.1)$$

where  $s$  and  $a$  are the atomic spacings of the Au substrate layer (2.89Å) and the Ti adlayer, respectively,  $\theta$  is the angle between the two layers and  $h, k, m, n$  are integer multiples of the Au(111) ( $h, k$ ) and Ti overlayer ( $m, n$ ) interatomic spacing, which lead to the coincidence between both lattices. The coincidence in terms of the Au(111) spacing is given by the vector  $\mathbf{v} = (8, 4)$ , as emerges from the LEED data, whereas in terms of the Ti spacing is given by the vector  $\mathbf{w} = (7, 3)$ ; this can be found from atomically resolved STM images, as those ones in Fig. 3.6. From the above discussion, we have  $h = 8, k = 4, m = 7, n = 3$ , and from Equation (3.1) we can find

$$a = s \sqrt{\frac{h^2 + hk + k^2}{m^2 + mn + n^2}} = 3.43 \text{ \AA} \quad (3.2)$$

and

$$\theta = \arctan \left[ \frac{\sqrt{3}(km - hn)}{2hm + hn + km + 2kn} \right] = 2.11^\circ \quad (3.3)$$

All the quantities to build the atomic model for this phase, now, are known, and Fig. 3.6(d) shows this model, where the Ti overlayer (red circles) with a 3.43 Å periodicity is placed on the Au(111)(1 × 1) substrate, having a 2.89 Å periodicity, with a relative angle of 2.11°. The angle between Ti and Au lattices estimated by this model is in agreement with STM results, obtained by measuring the angle between the pinwheel lattice and the honeycomb one (since the latter is aligned with the substrate's) at their boundary ( $\sim 2.2^\circ$ ), as shown in Fig. 3.6(e).

Additional features are present in Fig. 3.6(d): green triangles can be identified with the inner part of triangles which make up the pinwheel hexagonal unit cell, which usually appears brighter in atomically resolved STM images (e.g. Fig. 3.6(c)); an explanation for their brighter appearance may be that the sites occupied by Ti atoms in these triangles are very close (*quasi-coincidence*) with the atomic sites of the Au substrate; therefore, they arise a little with respect to atoms in *hollow* or *quasi-hollow* sites. On the other hand, green-circled blue spots in Fig. 3.6(d) represent the coincidence sites,

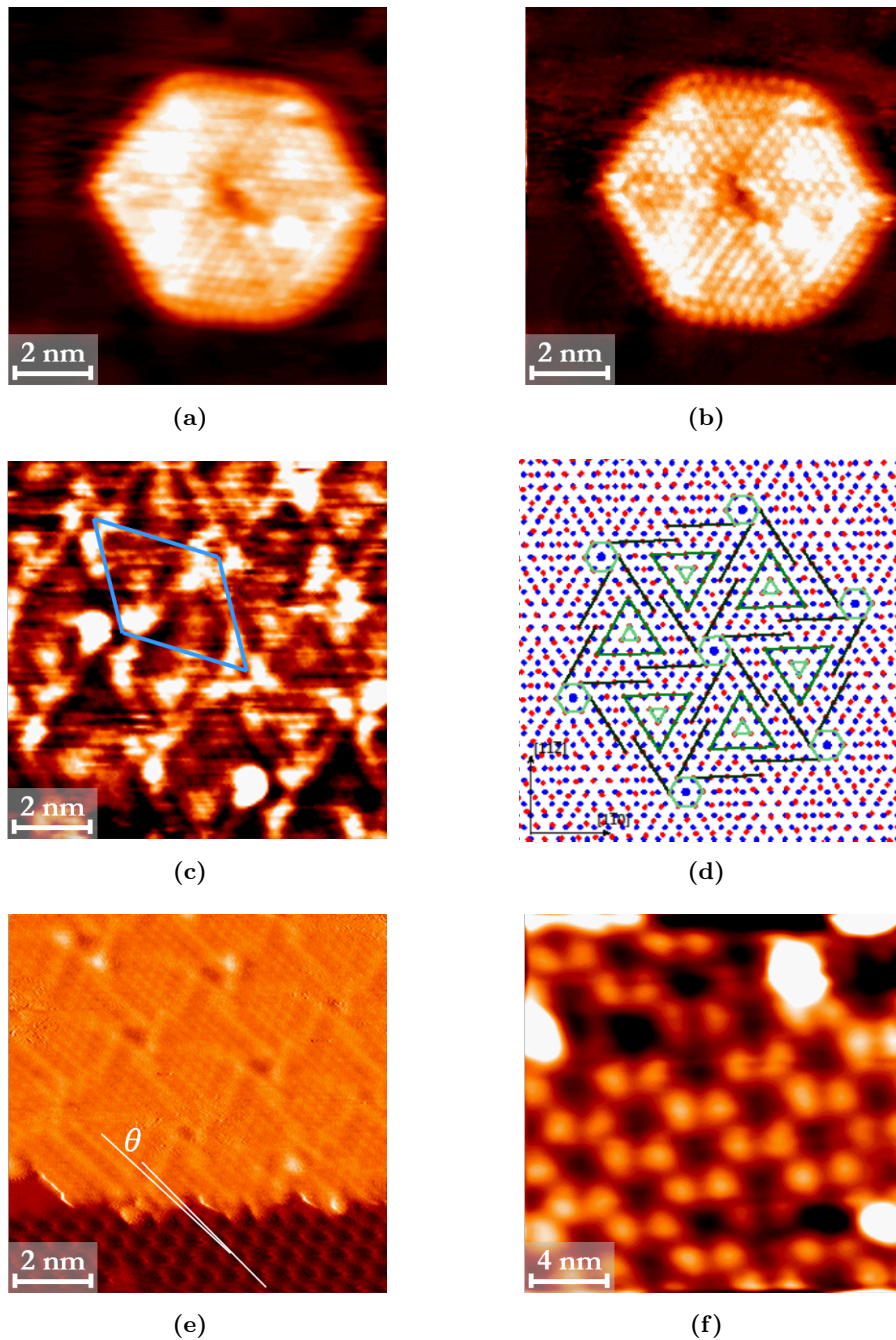


**Figure 3.6:** Atomic structure of the pinwheel phase. Low coverage: (a) atomically resolved STM image (0.2 MLE, W tip,  $10 \times 10 \text{ nm}^2$ ,  $V = 0.13 \text{ V}$ ,  $I = 2.5 \text{ nA}$ ); (b) same image as (a), graphically filtered to enhance the surface corrugation. High coverage: (c) atomically resolved STM image (1.1 MLE, W tip,  $10 \times 10 \text{ nm}^2$ ,  $V = 0.17 \text{ V}$ ,  $I = 1.82 \text{ nA}$ ); (d) atomic model of the pinwheel phase based on the Moiré pattern (blue = Au; red = Ti; bigger blue circles represent the coincidence sites; a schematic draw of the pinwheel geometry is highlighted); (e) atomically resolved STM image, graphically filtered to enhance the surface corrugation; the angle  $\theta$  between the honeycomb and pinwheel lattices is depicted (1.1 MLE, W tip,  $10 \times 10 \text{ nm}^2$ ,  $V = -1 \text{ V}$ ,  $I = 0.45 \text{ nA}$ ); (f) example of the effect of the applied bias (1.3 MLE, W tip,  $20 \times 20 \text{ nm}^2$ ,  $V = 2.51 \text{ V}$ ,  $I = 0.38 \text{ nA}$ ,  $T = 110 \text{ K}$ ).

which in STM images are pictured as black spots. The uncertainty regarding their origin (electronic effects or actual Ti vacancies) and the location of oxygen atoms still remains, even if the Ti vacancy hypothesis seems more likely due to the unfavorable energetic *on-top* positioning on these sites. Nonetheless, as already stressed, this Moiré-like model represents a qualitative interpretation of the STM images, although supported by LEED data; more advanced theoretical simulations are needed in order to answer these open issues. Another unresolved question is the stoichiometry of this phase; we have not made any hypothesis on this matter, whereas Wu *et al.*<sup>[12]</sup>, by comparing this system to other similar ones (e.g. VO<sub>x</sub>/Rh(111)<sup>[72,73]</sup>), assumed a TiO stoichiometry; also in this case theoretical studies should shed light on this matter. As a final remark, Fig. 3.6(f) shows the effect of a relatively high applied bias (2.5 V), which was also observed in the previous thesis work<sup>[13]</sup>: the inner part of the triangles, which build the pinwheel structure, appears bright and homogeneous; the reason why this electronic effect occurs is still unclear; however, an analogous effect was observed for the pinwheel phase of the system VO<sub>x</sub>/Pd(111)<sup>[57]</sup>.

### Triangular

Concerning the triangular phase, the previous observations<sup>[13]</sup> have been confirmed: this phase starts to appear at 0.4 MLE on top of the pinwheel phase with a height of 0.45 nm with respect to it; in addition, it can grow on the honeycomb film, but with a different relative height (0.6 nm). As an example, Fig. 3.7(a) shows two triangular crystallites growing on the honeycomb film; the same image was graphically filtered (Fig. 3.7(b)) unveiling the bilayered structure of these islands. The presence of more than one layer is also suggested by high-resolution STM images, such as Fig. 3.7(c) and Fig. 3.7(d); the latter was filtered in the same way as Fig. 3.7(b), enhancing the corrugation of this crystallite. However, still no atomic resolution has been obtained, no clear interpretation about the different relative heights (with respect to the pinwheel and honeycomb phases) exists and, likewise all the other phases, no theoretical models about its atomic structure are available. Nonetheless, a hexagonal symmetry can be ascribed to this phase.

### Row

Regarding the row phase, as already mentioned in Section 2.5, it appears above  $\sim 1$  MLE in the form of large islands (with a typical area of 400-1000 nm<sup>2</sup>), made of multiple layers with the height of about 0.25 nm, as shown in Fig. 3.8(a); this height seems independent on the applied bias. Higher magnification images allow to recognize the presence of brighter and darker rows (Fig. 3.8(b)), which exhibit a slightly different apparent height, as illustrated by the line profile in Fig. 3.8(c). In addition, it has been found that, similarly to the triangular islands, these crystallites show a different minimum relative height depending on the phase underneath (0.43 nm with respect to the pinwheel and 0.58 nm with respect to the honeycomb). Another improvement obtained with the present analysis is the achievement of atomically resolved STM images, such as the one shown in Fig. 3.8(d). The aforementioned bright and dark rows are defined by black “channels” and are made of parallel rows of two or three atoms, respectively; the height difference between the two kinds of rows is about 0.4 Å. In the same figure, also, the rectangular unit cell is reported with dimensions  $(5.7 \pm 0.2) \times (58 \pm 1)$  Å<sup>2</sup>; the measured interatomic distance is  $3.2 \pm 0.2$  Å. Since these STM measurements have not shown a bias dependence, we can infer that these are a consequence of the topography rather than of the electronic contrast; as a

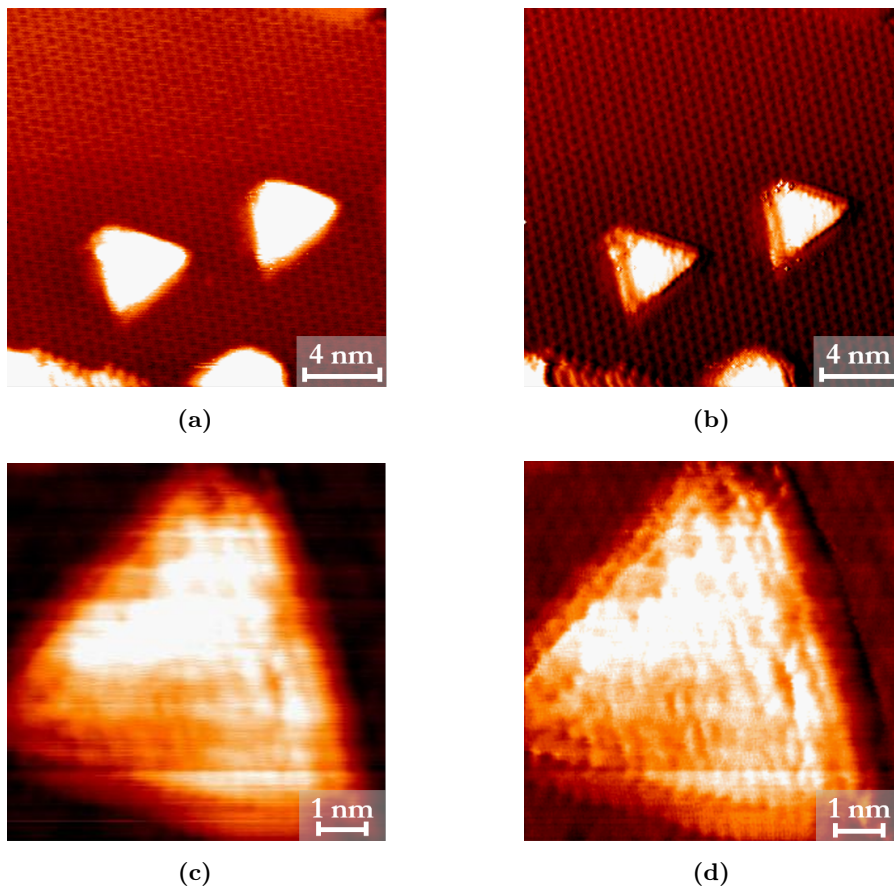


**Figure 3.7:** STM images of the triangular phase. (a) 1.1 MLE, W tip ( $20 \times 20 \text{ nm}^2$ ,  $V = 0.76 \text{ V}$ ,  $I = 0.23 \text{ nA}$ ). (b) Same as (a), after applying a graphic filter to enhance the surface corrugation. (c) 1.3 MLE, W tip ( $8 \times 8 \text{ nm}^2$ ,  $V = 0.45 \text{ V}$ ,  $I = 1.7 \text{ nA}$ ,  $T = 110 \text{ K}$ ). (d) Same as (c), after applying a graphic filter to enhance the surface corrugation.

first approximation, so, black “channels” and dark rows may be associated with two or one rows of missing Ti atoms with respect to the bright rows, respectively.

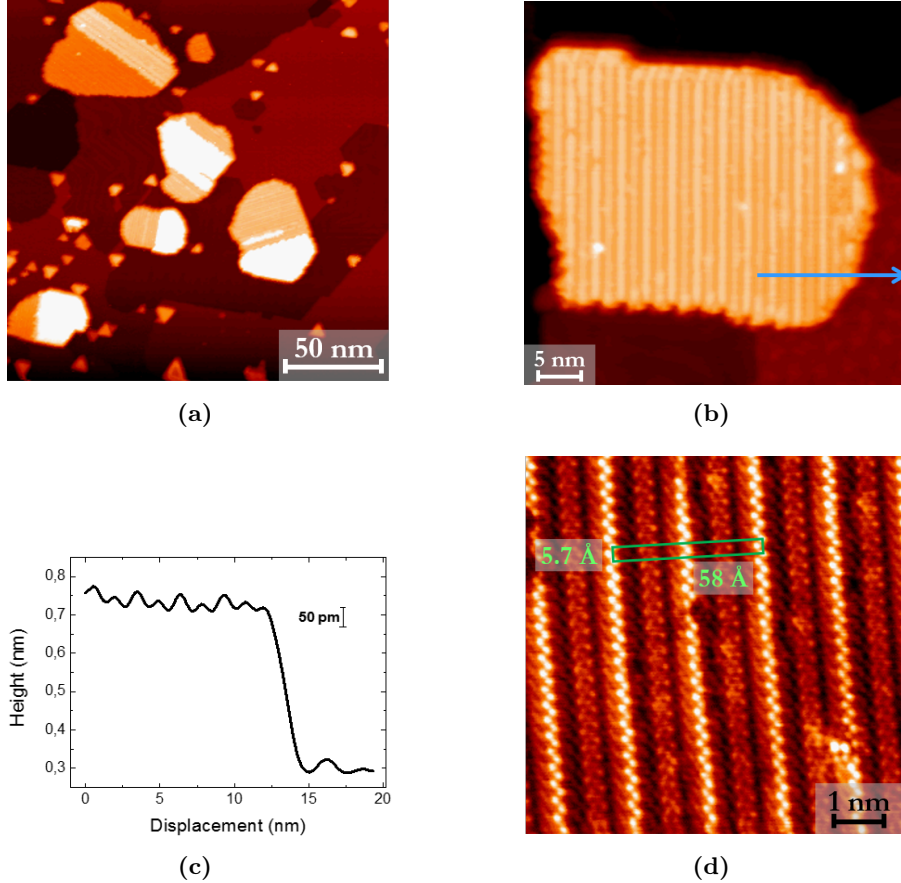


**Figure 3.8:** STM images of the row phase. **(a)** “Low”-magnification image; some row phase islands consisting of at least two layers are visible (1.3 MLE, W tip,  $200 \times 200 \text{ nm}^2$ ,  $V = 1 \text{ V}$ ,  $I = 0.38 \text{ nA}$ ). **(b)** Higher magnification image; the line profile shown in (c) has been taken along the blue arrow (1.1 MLE, W tip,  $45 \times 45 \text{ nm}^2$ ,  $V = 0.79 \text{ V}$ ,  $I = 0.19 \text{ nA}$ ). **(c)** Line profile corresponding to the blue arrow in (b). **(d)** Atomically resolved STM image; the rectangular unit cell is depicted in green (1.1 MLE, W tip,  $15 \times 15 \text{ nm}^2$ ,  $V = 0.3 \text{ V}$ ,  $I = 1.46 \text{ nA}$ ).

### Needle

The needle-like phase had already been observed<sup>[13]</sup>, but no high-magnification images could be obtained on it. As the row phase, it grows at relatively high coverage (at least 1 MLE) in the form of nanowires, reaching a length of even 150 nm and a width of about 5 nm at most (as illustrated in Fig. 3.9(a)). This kind of structures seem to exhibit a cylindrical shape, as shown in Fig. 3.9(b) and by the line profile in Fig. 3.9(c), which was recorded along the blue arrow in Fig. 3.9(b). Moreover, the same figure reports the rectangular unit cell, with dimensions  $(3.2 \pm 0.2) \times (5.2 \pm 0.1) \text{ \AA}^2$ ; in this image six atomic rows are visible. In addition, the maximum height relative to the honeycomb phase ( $\sim 0.75 \text{ nm}$ , as in Fig. 3.9(c)) is greater than the one relative to the pinwheel phase ( $\sim 0.60 \text{ nm}$ ); these values are not significantly bias dependent. Finally, Fig. 3.9(d) shows a very high magnification atomically resolved STM image. Also for this phase a theoretical study is necessary in order to understand in more detail its structure and to determine its stoichiometry.

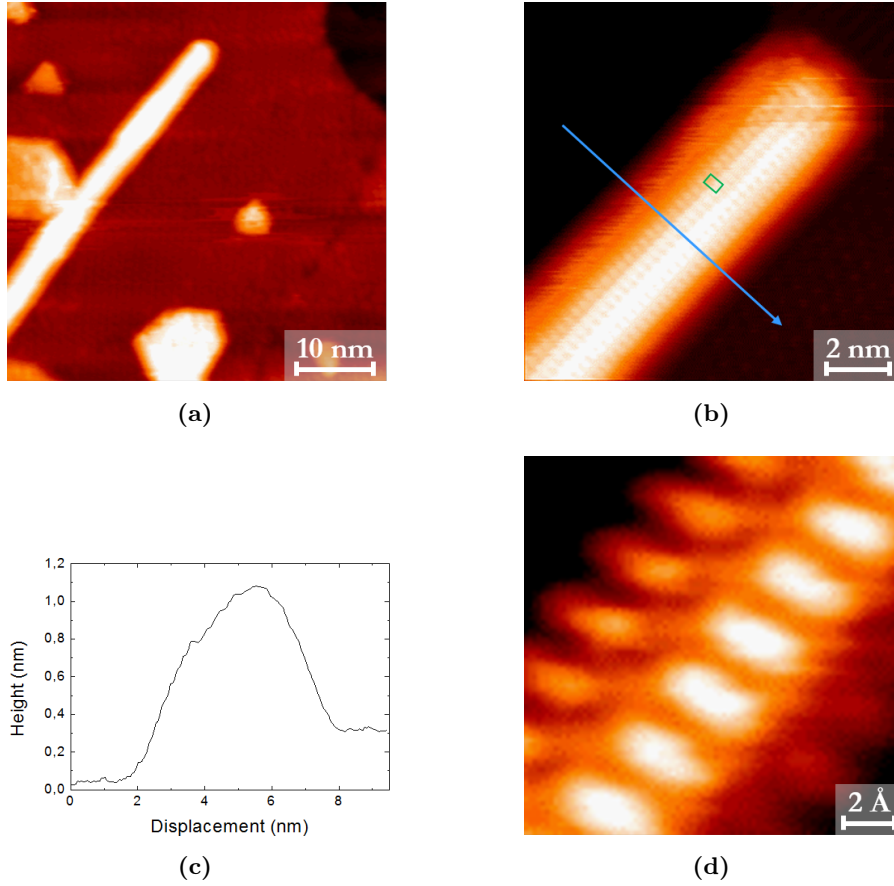


**Figure 3.9:** STM images of the needle phase. (a) “Low”-magnification image (1 MLE, Cr tip,  $50 \times 50 \text{ nm}^2$ ,  $V = 0.87 \text{ V}$ ,  $I = 1 \text{ nA}$ ,  $T = 110 \text{ K}$ ). (b) Atomically resolved image; the unit cell is also shown (1.1 MLE, Cr tip,  $12 \times 12 \text{ nm}^2$ ,  $V = 0.1 \text{ V}$ ,  $I = 3.1 \text{ nA}$ ). (c) Line profile recorded along the blue arrow in (b). (d) High-magnification atomically resolved STM image (1.1 MLE, Cr tip,  $1.5 \times 1.5 \text{ nm}^2$ ,  $V = 0.1 \text{ V}$ ,  $I = 3.1 \text{ nA}$ ).

As a final remark, Table 3.1 shows a summary of the structural analysis of the  $\text{TiO}_x/\text{Au}(111)$  phases, which are displayed as a function of coverage; LEED data for the pinwheel and honeycomb phases are considered (the stoichiometry reported for the second one is based on Ref. [12]), whereas, regarding the row and needle phases, data come from STM experiments. As it can be clearly observed, no data for the triangular phase is known concerning the structural point of view.

**Table 3.1:** Summary of the structural analysis on the  $\text{TiO}_x/\text{Au}(111)$  phases.

		Coexistent $\text{TiO}_x$ phases			
Coverage (MLE)	0.25	Pinwheel $\begin{bmatrix} 12 & 4 \\ 8 & 12 \end{bmatrix}$ Comm. hexagonal $(\sqrt{111} \times \sqrt{111})R19.1^\circ$	Triangular <i>No data</i>		
	0.4				
	0.8				
	$\geq 1$			Honeycomb ( $\text{Ti}_2\text{O}_3$ ) $\begin{bmatrix} 2 & 0 \\ 0 & 2 \end{bmatrix}$ Comm. hexagonal $(2 \times 2)$	Row Rectangular $5.7 \text{ \AA} \times 58 \text{ \AA}$ <i>No further data</i>

### 3.2.3 Adsorbates

Surface defects on metal oxides offer an attractive binding environment for adsorbates, so that they can heavily influence the chemical reactivity of the oxide surface<sup>[33]</sup>. The presence of adsorbates on the system  $\text{TiO}_x/\text{Au}(111)$  has frequently been detected at high coverage, as shown by Figure 3.10; it should be noted that all those images were recorded at  $T = 110$  K. The reason for their presence may be due to some impurities in the UHV chamber. Fig. 3.10(a) shows the adsorbates on both the pinwheel and honeycomb phases, whereas in Fig. 3.10(b) a magnification on the pinwheel phase is shown. They appear as particle-like bright protrusions and they can be located near the pinwheel “hub” (as in the green circle in Fig. 3.10(b)) or they can aggregate, forming a sort of cluster of 1-2 nm<sup>2</sup>, partially or totally covering the hole of this reconstruction (blue and yellow circles in the same figure, respectively). On the other hand, Figs. 3.10(c) and 3.10(d) were recorded on the honeycomb phase; in this case, adsorbates clearly place themselves in the honeycomb “holes” and have almost the same size as the previous case ( $\sim 1$  nm<sup>2</sup>); conversely, they exhibit a bias dependence, which was not observed in the previous case.

Notably, Figs. 3.10(d)(I) and (II) are two STM images of the same portion of the honeycomb film recorded in succession and in both images a change of bias has been applied: the lower part of Fig. 3.10(d)(I) has been acquired at  $-0.2$  V and the upper at  $-0.9$  V; *vice versa* holds for Fig. 3.10(d)(II). Performing other analogous measurements, it was found that adsorbates were detected at  $V < -0.4$  V (as in the line profile in Fig. 3.10(b)(III)), they were not observed in the range  $-0.4$  V  $< V < 0.6$  V and, finally, they “came back” with  $V > 0.6$  V, as in Fig. 3.10(c); in the last case, they appear as large Gaussian protrusions of 0.7 Å height.

A similar behavior was already observed for Pd<sup>[74]</sup> and Ag<sup>[75]</sup> atoms deposited onto  $\text{SiO}_2/\text{Mo}(112)$  with a honeycomb structure. In that cases, at high voltage bright circular protrusions in STM images appear as a consequence of the availability for the electron transport of the adatoms’ 5s resonant state; on the contrary, at low bias the contrast decreases since the aforementioned 5s state of the adatoms undergoes hybridization with the 2p orbitals of oxygen, so that the inner part of the protrusion decreases until the adatoms appear as slightly brighter hexagonal rings of the honeycomb film. Figure 3.11 shows, as an example, the bias dependence of STM images of Pd atoms on  $\text{SiO}_2$  on Mo(112).

In our case, we could not determine the nature of the observed adsorbates, so we have no knowledge about the physical process which governs this effect; however, from these results we can infer the possibility to employ these bidimensional  $\text{TiO}_x$  phases as templates for atom and cluster deposition with the aim to study the chemical reactivity of this oxide surfaces.

### 3.2.4 Defects on the Au(111) surface

At low coverage (0.2–0.3 MLE) and at low temperature (110 K), during our experimental campaign, we frequently observed some defects in the  $dI/dV$  signal, resembling a sort of “ring”, as in Figure 3.12(a). Moreover, some of these “rings” occasionally superimposed to each other, giving rise to a protrusion in the location of their superposition (highlighted with a blue square in Fig. 3.12(a)). By observing the

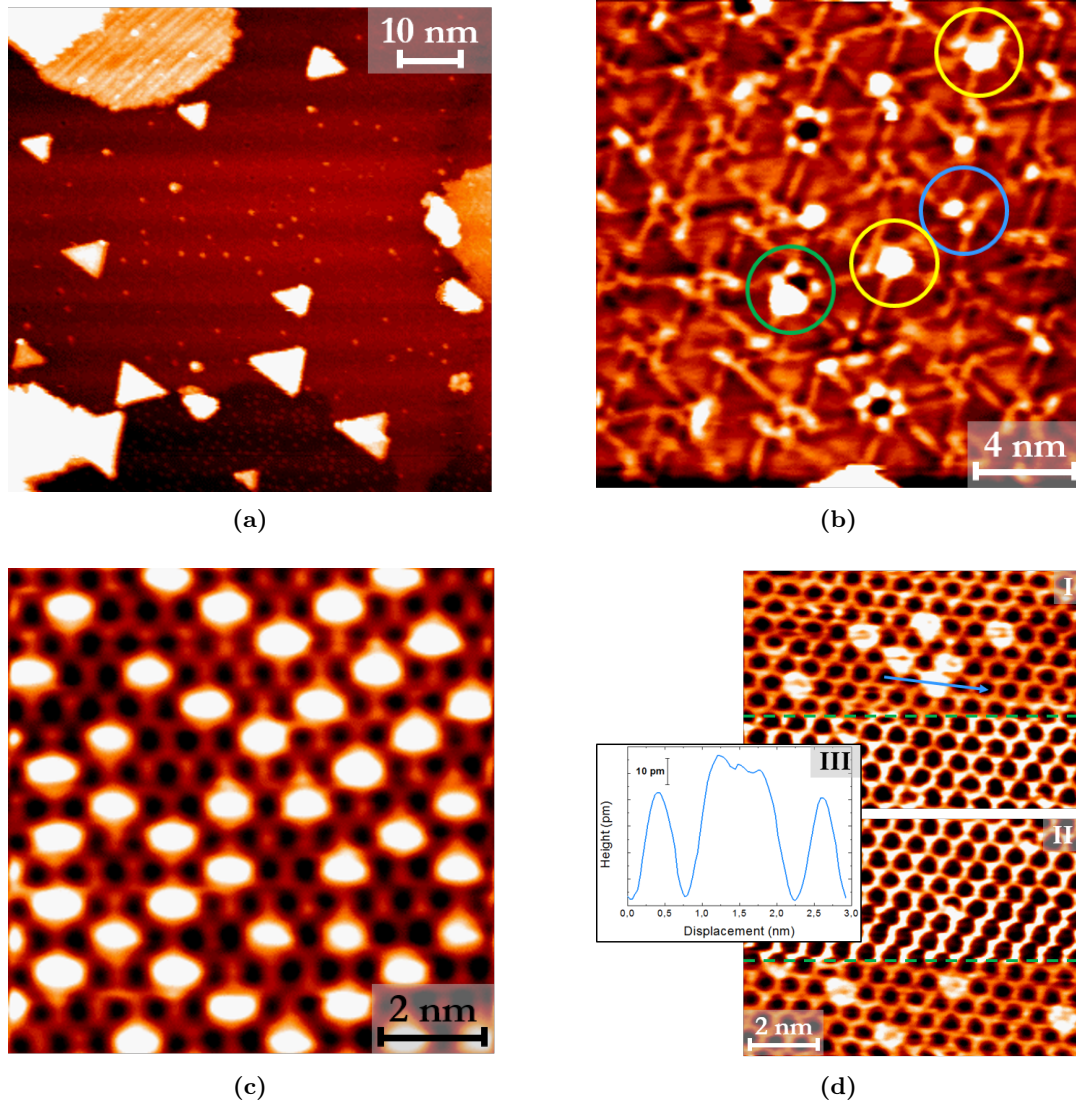


**Figure 3.10:** STM images of the adsorbates on the pinwheel and honeycomb phases acquired at  $T = 110$  K. **(a)** “Low”-magnification image; adsorbates are visible on both phases (1.3 MLE, W tip,  $80 \times 80$  nm<sup>2</sup>,  $V = 1.16$  V,  $I = 0.77$  nA). **(b)** Adsorbates, highlighted with colored circles, on the pinwheel phase (1.3 MLE, W tip,  $20 \times 20$  nm<sup>2</sup>,  $V = 1.16$  V,  $I = 0.77$  nA). **(c)** Adsorbates on the honeycomb phase (1 MLE, W tip,  $9.4 \times 9.4$  nm<sup>2</sup>,  $V = 1.15$  V,  $I = 1$  nA). **(d)** Bias dependence of the adsorbates on the honeycomb phase (1.1 MLE, W tip,  $10 \times 7$  nm<sup>2</sup>,  $I = 1.94$  nA). **(I)** Lower part acquired at  $-0.2$  V, higher at  $-0.9$  V; **(II)** lower part acquired at  $-0.9$  V, higher at  $-0.2$  V (same image as **(I)**); **(III)** line profile recorded along the blue arrow in **(I)**.

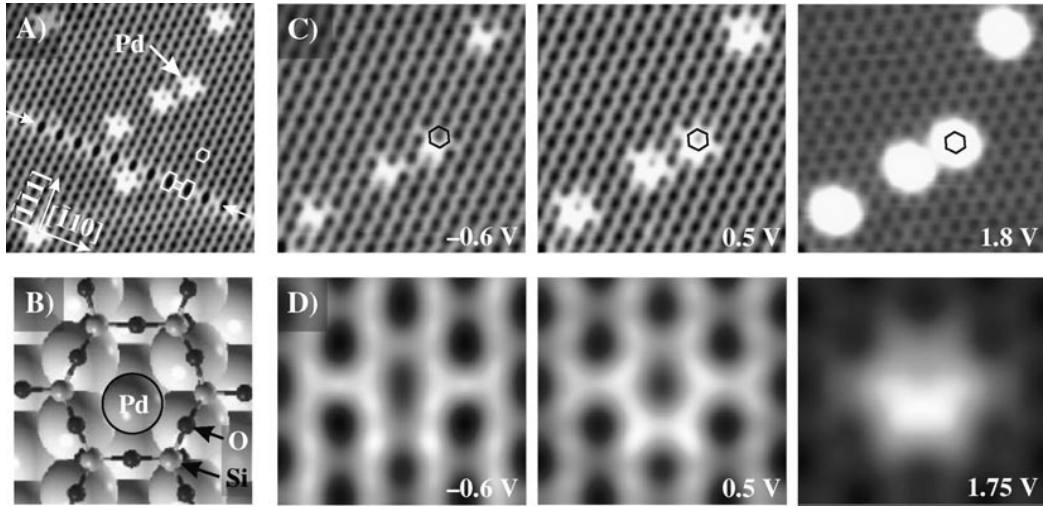


**Figure 3.11:** (A) STM image ( $13 \times 13 \text{ nm}^2$ ,  $V = 0.5 \text{ V}$ ) of 0.1 ML Pd on  $\text{SiO}_2$  on Mo(112). (B) Structure model for the Pd adsorption site (small black spheres: O; small grey spheres: Si; large grey sphere: Pd). Bias dependence of the topographic contrast of Pd atoms in (C) experimental ( $5 \times 5 \text{ nm}^2$ ) and (D) simulated STM images ( $1.8 \times 1.6 \text{ nm}^2$ ,  $6 \times 4$  supercell).<sup>[74]</sup>

corresponding topographic images (in this case, Fig. 3.12(b)), these defects were not detected; however, if any superposition occurred, an analogous protrusion was found also in topographic images (as the blue-boxed one in Fig. 3.12(b)). Analogous “rings” in the differential conductivity maps were found by Schouteden *et al.*<sup>[42]</sup>; however, in that case the clean Au(111) surface was investigated and they were interpreted as standing-wave patterns. In our case, conversely, we have not a clear interpretation of these effects; a deeper study may shed light on this matter.

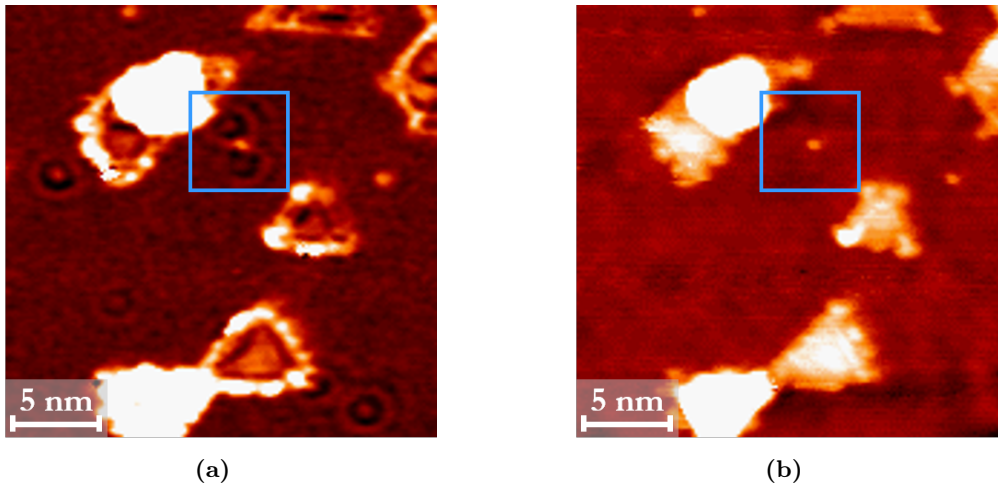


**Figure 3.12:** STM images of defects on the Au(111) surface at low coverage (0.2 MLE,  $25 \times 25 \text{ nm}^2$ ,  $V = 1.26 \text{ V}$ ,  $I = 0.61 \text{ nA}$ ,  $T = 110 \text{ K}$ ). (a)  $dI/dV$  map; the superposition between two “rings” is highlighted; (b) topographic image; the same location marked in (a) is also highlighted in this image; in this area a protrusion is detected.

### 3.3 Electronic properties of the $\text{TiO}_x/\text{Au}(111)$ system

In this section, the local electronic properties of the  $\text{TiO}_x/\text{Au}(111)$  system will be considered, showing their study by means of the STS technique. The first subsection (3.3.1) deals with the general procedure to collect and normalize STS spectra; the following ones are respectively focused on a single  $\text{TiO}_x/\text{Au}(111)$  phase and also on the  $\text{Au}(111)$  surface. Afterwards, a comparison between all the investigated phases is made (Sub-section 3.3.7). However, no STS analysis on the needle phase could be achieved, since it rarely appeared in the STM measurements.

#### 3.3.1 Data collection and analysis procedures

As mentioned in Section 3.1, STS spectra are acquired at low temperature, notably about 110 K, in order to avoid on the one hand tip and sample instability, on the other hand to reduce thermal drift effects. Before acquiring the spectra, so, STM imaging is performed and the operator tries to get a measurement stability applying voltage pulses to the tip; after, an area of interest is chosen (visualized in an STM image, the so-called “reference image”) and STS spectra are acquired on each phase to be analyzed (the voltage ramp usually goes from  $-2.5$  to  $+2.5$  V); it must be noted that the STM measurement goes on during this analysis, except during the proper acquisition of the spectrum. For consistency, we recorded from three to five spectra at each point of choice within short time intervals; it should be noted that both  $dI/dV$  (lock-in differential conductivity) and  $I(V)$  curves are recorded at the same time. This procedure is repeated until a new area of interest (reference image) is chosen. The data are then collected in a spreadsheet and an average (for each phase and for each reference image) is obtained. The averaging procedure is justified since spectra are acquired in the same experimental conditions and after verifying a similar trend in the curves; indeed, if the setpoint voltage, setpoint current and lock-in parameters<sup>b</sup> are changed (or just one of them), a new average must be calculated. A sufficient statistic should be obtained in order to compare different curves and properly select data for the subsequent normalization procedure. Afterwards, each couple of average lock-in  $dI/dV$  curve and  $I(V)$  is imported in a Matlab program (developed in NanoLab) which extracts a normalized  $dI/dV$  curve. To do so, this program works in three steps:

1. rescaling process: the average lock-in  $dI/dV$  is compared to the numerical  $dI/dV$ , obtained by the numerical differentiation of the average  $I(V)$ ; the result is the so-called “rescaled  $dI/dV$ ”, whose units are nA/V;
2. optimization of the normalization parameters (i.e.  $z_0$ , see Sub-section 1.2.2);
3. choice of the normalization method: the program allows to choose between the methods proposed by Stroscio *et al.*<sup>[29]</sup>, Ukraintsev *et al.*<sup>[30]</sup> and Koslowski *et al.*<sup>[31]</sup>.

Notably, we have chosen the normalization method proposed by Ukraintsev *et al.* (with a symmetric transmission coefficient,  $T_{sym}$ , and  $\Phi = 4.5$  eV) since it allows to avoid the numerical problems that are present in the other two normalization procedures, thus providing the most reliable results. Another reason supporting this choice is that with the ( $I/V$ ) method a singularity in  $V = 0$  is obtained and with the method of Koslowski *et al.* an abrupt decrease in the negative voltage region occurs.

<sup>b</sup>A deeper explanation about the lock-in amplifier is presented in Appendix A.2.2.

Using this kind of normalized  $dI/dV$  the sample DOS is probed mainly at positive applied voltage (unoccupied states), while the tip DOS is probed mainly at negative bias<sup>[30]</sup>. However, assuming that the tip DOS is nearly constant in the measured region, and higher than the sample DOS at the Fermi level, Equation (1.29) gives information about both occupied and unoccupied DOS in the surface region, provided the negative bias is not too large, i.e. it can be employed to extract also features related to sample occupied states<sup>[30]</sup>. Finally, the normalized  $dI/dV$  curves are plotted and compared to each other; a further average between similar curves can be performed in order to highlight a general trend for each  $\text{TiO}_x/\text{Au}(111)$  phase. It should be noted that both Cr and W tips have been used, in order to discriminate their influence on measurements, as already mentioned in Section 3.1. A comparison between the spectra obtained with a Cr tip and the ones obtained with a W tip, indeed, will be shown afterwards (obviously for each phase).

Figure 3.13 illustrates an example of the aforementioned procedure; notably, the pinwheel phase at high coverage is considered. Fig. 3.13(a) shows the so-called reference image, on which several colored circles are present: these represent the points on which multiple STS spectra have been recorded; these are shown in Fig. 3.13(b), where each curve corresponds to the equally colored circle in Fig. 3.13(a); the curves are stacked to make them distinguishable. After, they are averaged (Fig. 3.13(c)) and the lock-in  $dI/dV$  is compared to the numerical derivative of  $I(V)$  (shown in Fig. 3.13(d)), which is the already mentioned numerical  $dI/dV$  (Fig. 3.13(e)): this figure is quite self-explanatory concerning the reason why the numerical  $dI/dV$  is not normalized, but the lock-in one. The normalized  $dI/dV$  curve for this example is shown in Fig. 3.13(f). Henceforth, the quantity  $n$  will be referred to as the number of single spectra by which the normalized  $dI/dV$  (or non-normalized one) is made up; in this case,  $n = 22$ . Also, vertical lines are added to clarify the Fermi level ( $E = 0$ ) and the energy of peaks. In addition, other quantities will be identified: the symbol  $o_x$  will be employed to label the position of a peak in the occupied states (i.e. negative energies) for the phase  $x$ , while  $u_x$  to label a peak in the unoccupied states (i.e. positive energies); in most cases their positions have been determined with the help of a Gaussian fit. In addition, the quantity  $\Delta$  is defined as the energy difference between  $u_x$  and  $o_x$ , i.e.  $\Delta = u_x - o_x$ . The values of  $u_x$ ,  $o_x$  and  $\Delta$  are specified in the captions. For the example shown in Fig. 3.13(f),  $o_p$  is not present but  $u_p = 0.5$  eV;  $\Delta$ , then, can be calculated. The value of  $\Delta$ , however, has been considered more important for the triangular and row phases in our analysis, rather than the aforementioned peaks, since in some cases the spectra of these phases show a zero minimum in  $E = 0$ ; in other words, the LDOS shows a minimum at the Fermi level, so  $\Delta$  becomes somehow similar to the bulk energy gap  $E_g$ .

In the following sections the full procedure will not be shown, but only the normalized  $dI/dV$  curve (such as Fig. 3.13(f)) and, usually, the reference image (such as Fig. 3.13(a)); also, some averages calculated considering similar normalized  $dI/dV$  curves will be shown. In some cases, moreover, the separated  $dI/dV$  curves cannot be averaged on the whole, since some differences occur, so they are grouped in “families”, averaged and normalized discerning the different families. Finally, as already mentioned, in Sub-section 3.3.7 a final overview of the STS analysis is presented, comparing some exemplifying spectra.

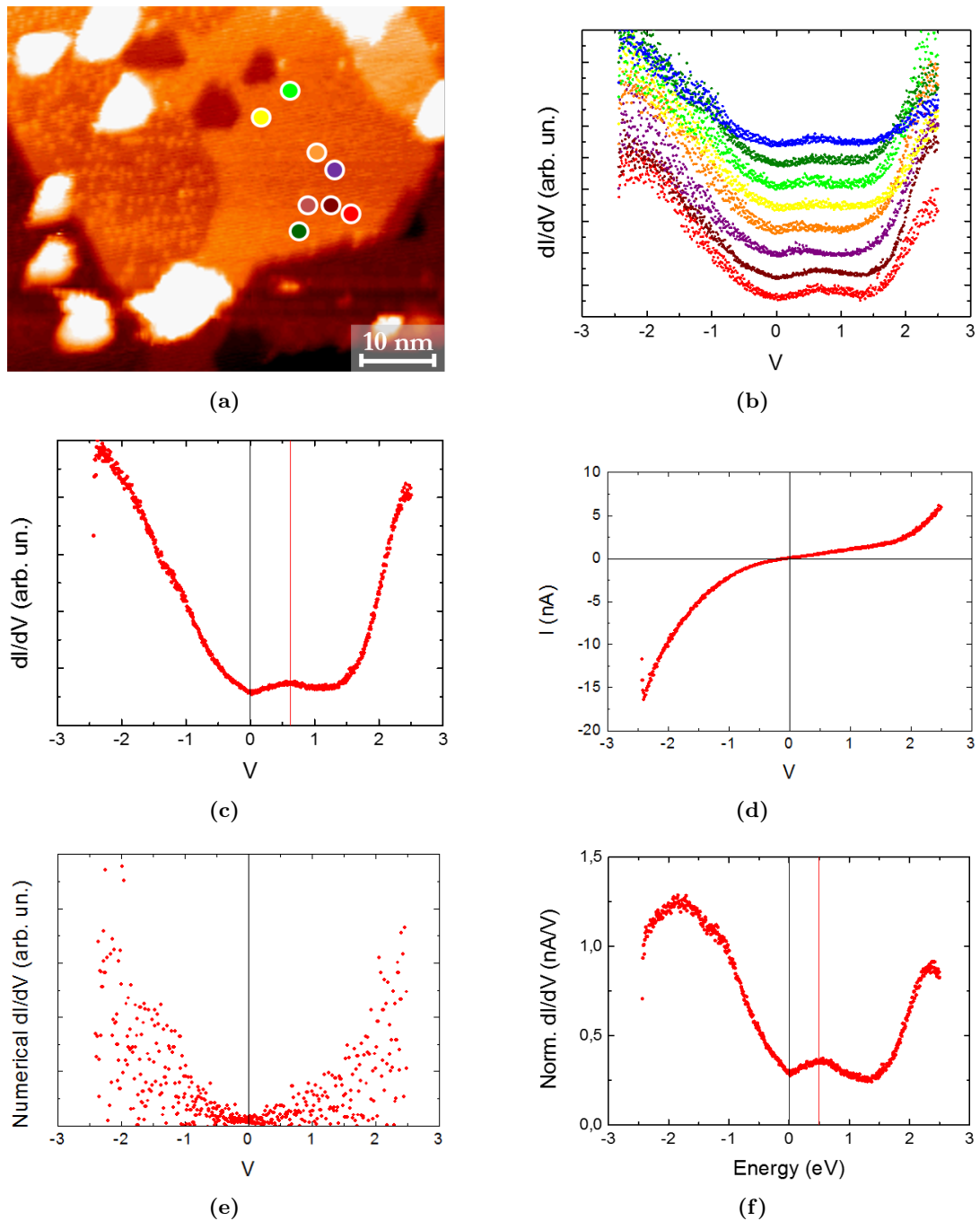


**Figure 3.13:** Example of the data collecting procedure. (a) Reference image (1.3 MLE, W tip,  $60 \times 50 \text{ nm}^2$ ,  $V = 1.24 \text{ V}$ ,  $I = 0.7 \text{ nA}$ ); on each colored circle three different spectra are acquired (except blue and dark green, 2). (b) Separated spectra ( $V = 0.6 \text{ V}$ ,  $I = 0.8 \text{ nA}$ ); each colored curve corresponds to the equally colored circle in (a). (c) Average  $dI/dV$ . (d) Average  $I(V)$ . (e) Numerical  $dI/dV$ . (f) Normalized average  $dI/dV$  ( $n = 22$ ,  $u_p = 0.5 \text{ eV}$ ,  $z_0 = 5 \text{ \AA}$ ).

### 3.3.2 Au(111)

STS spectra on the clean Au(111) surface were acquired both at low and high coverage, with Cr tips as well as W tips. The results of the low-coverage analysis are summarized in Figure 3.14. The STM image in Fig. 3.14(a) and the STS spectrum in Fig. 3.14(b) were acquired with a Cr tip at 0.35 MLE. The latter shows the presence of the Shockley peak at  $-0.52$  eV, a slightly different value than the literature one of  $-0.46$  eV<sup>[42]</sup>. The STM image in Fig. 3.14(c) and the average spectrum in Fig. 3.14(d), conversely, have been acquired with a W tip and at 0.25 MLE. In this case, the STS average spectrum has not been normalized, due to the absence of the exponential tails. Nevertheless, the Shockley peak is evident and its value is  $-0.5$  eV, similarly as the previous case.

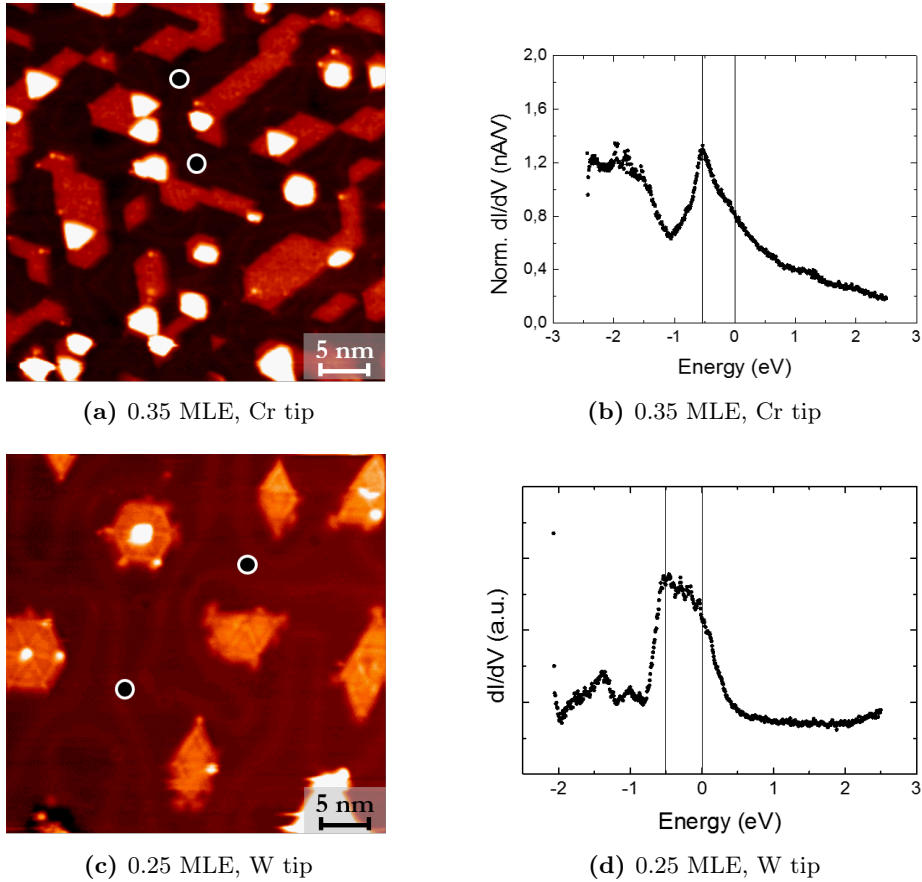


**Figure 3.14:** STS of Au(111) at low coverage. 0.35 MLE, Cr tip: (a) reference image ( $40 \times 40$  nm<sup>2</sup>,  $V = 1.4$  V,  $I = 1.2$  nA), (b) STS spectrum ( $n = 6$ ,  $z_0 = 7.5$  Å). 0.25 MLE, W tip: (c) reference image ( $40 \times 40$  nm<sup>2</sup>,  $V = 1.4$  V,  $I = 1.2$  nA), (d) STS spectrum ( $n = 6$ , non-normalized).

Figure 3.15 depicts the results of the STS analysis at high coverage (1.3 MLE for all the figures). In this case, however, no spectra with a Cr tip could be acquired. Fig. 3.15(a) shows the STM reference image for the spectrum in Fig. 3.15(b), which exhibits a Shockley peak at  $-0.44$  eV, very close to the literature value<sup>[42]</sup>. Figs. 3.15(c) and 3.15(d), on the other hand, show a comparison between different STS curves (the red one is the same shown in Fig. 3.15(b); for the other ones, the reference images are not shown). In Fig. 3.15(c), notably, non-normalized curves are compared, while in Fig. 3.15(d) the corresponding normalized ones are present. The curves are stacked for

the sake of clarity. The Shockley peak values for these curves go from  $-0.44$  to  $-0.3$  eV and an overall feature is the presence of secondary peaks.

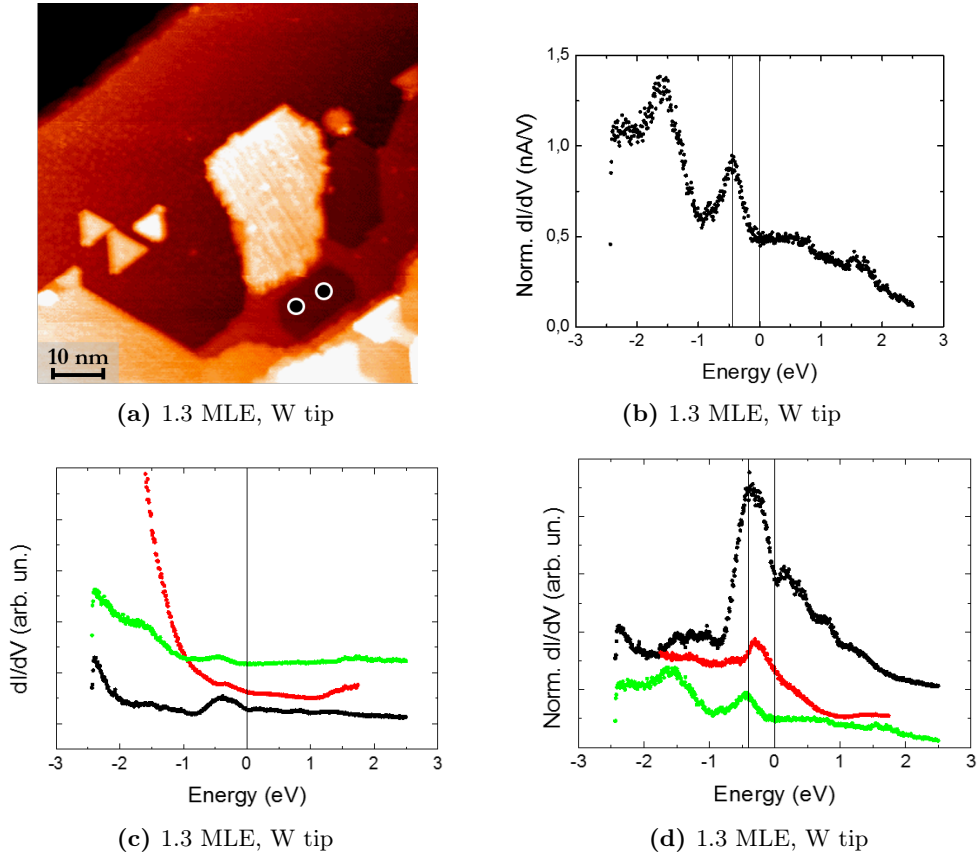


**Figure 3.15:** STS of Au(111) at high coverage (1.3 MLE, W tip). (a) Reference image for (b) ( $75 \times 75$  nm<sup>2</sup>,  $V = 0.87$  V,  $I = 0.44$  nA). (b) STS spectrum ( $V = 0.9$  V,  $I = 0.4$  nA,  $n = 6$ ,  $z_0 = 7.5$  Å). (c) Comparison between non-normalized average  $dI/dV$  curves (black:  $V = 0.7$  V,  $I = 0.8$  nA,  $n = 3$ ; green:  $V = 0.5$  V,  $I = 0.7$  nA,  $n = 2$ ; red: same as (b)). (d) Comparison between the normalized curves in (c) (black:  $z_0 = 9.5$  Å, green:  $z_0 = 9.5$  Å, red: same as (b)).

From this analysis on the Au(111) surface, similarities between the low and high coverage behaviors emerge; no substantial change in the Shockley peak value occurs, even if in some cases it is broadened or secondary peaks occur (e.g. Fig. 3.15(d)). The Au(111) surface electronic structure seems little perturbed by the presence of TiO<sub>x</sub> clusters or films, even in the high coverage regime only small areas remain uncovered, usually having a polygonal shape (e.g. Fig. 3.15(a)); conversely, this does not hold for the system Ti/Au(111), which shows a clear modification of the Shockley peak<sup>[67]</sup>; this effect may be correlated to the distortion of the Au(111) superstructure around Ti islands, which conversely does not occur for TiO<sub>x</sub> ones at low coverage.

### 3.3.3 Honeycomb

The honeycomb phase, as already mentioned, was not observed at low coverage, so clearly no STS analysis at low coverage was performed. Figure 3.16 shows the overall results of the STS analysis on this phase; the spectrum in Fig. 3.16(a) was acquired

with a Cr tip, while the ones in Fig. 3.16(b) with a W tip. The former has a peculiar trend, since no evident  $o_h$  peak is present and  $u_h$  is made of two sub-peaks; also, the local minimum is shifted from 0. On the contrary, both spectra in Fig. 3.16(b) exhibit the  $o_h$  peak (even if their values are not the same), as well as the  $u_h$  one; also, the blue spectrum shows the presence of secondary peaks (the negative one about at  $-1.5$  eV; the positive one after  $u_h$  is due to a normalization effect). The different qualitative behavior of the spectrum recorded with the Cr tip may be related to the presence of adsorbates on the surface of the honeycomb phase (this matter will be considered in Sub-section 3.2.3), but they have been observed also in other cases; another explanation may be the effect of the tip DOS.

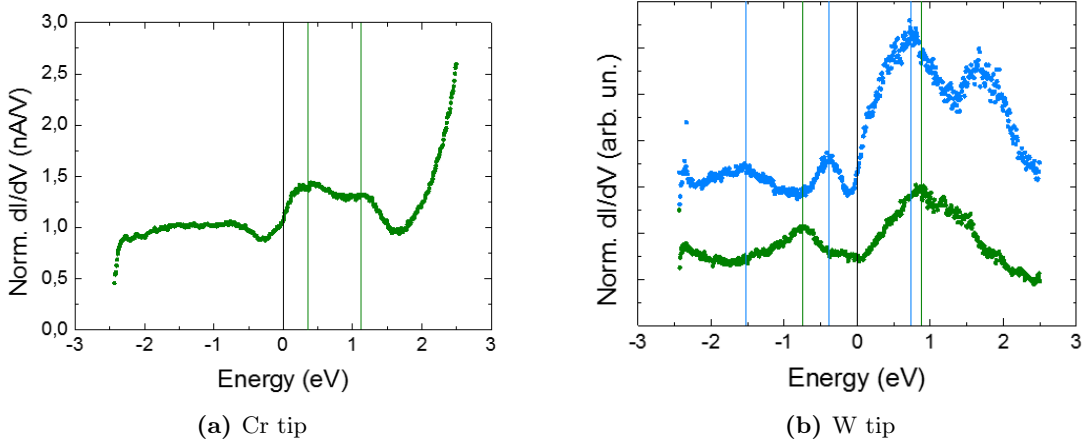


**Figure 3.16:** STS of the honeycomb phase at high coverage. **(a)** STS spectrum at 1 MLE with Cr tip ( $V = 0.9$  V,  $I = 0.8$  nA,  $n = 24$ ,  $z_0 = 8$  Å,  $u_{p1} = 0.35$  eV,  $u_{p2} = 1.13$  eV). **(b)** STS spectra with W tip (green: 1.1 MLE,  $V = 0.3$  V,  $I = 0.4$  nA,  $n = 9$ ,  $z_0 = 7.25$  Å,  $o_h = -0.74$  eV,  $u_h = 0.84$  eV,  $\Delta = 1.58$  eV; blue: 1.3 MLE,  $V = 0.6$  V,  $I = 0.8$  nA,  $n = 6$ ,  $z_0 = 9$  Å,  $o_h = -0.39$  eV,  $u_h = 0.75$  eV,  $\Delta = 1.09$  eV, secondary peak at  $-1.53$  eV).

A high-resolution STS analysis was performed on the honeycomb phase with the W tip, as illustrated in Figure 3.17. Notably, Fig. 3.17(b) shows the spectra acquired on the “edges” of the honeycomb rings, while Fig. 3.17(c) shows the spectra acquired in their “holes”. In Fig. 3.17(a) (reference image) no actual data points are shown, since they could not be individually determined (due to the combined effects of thermal drift and surface periodicity), hence just four points have been displayed as examples (so they must not be put in a one-to-one relationship with the curves in Figs. 3.17(b) and 3.17(c)). The green-colored circles correspond to the “edges” of the honeycomb rings, the blue-colored ones to the “holes”; the actual investigated points are equivalent to these examples. Also, contrary to the general procedure, in this case for each investigated point only one spectrum has been acquired; the reason is that, due to drift effects, the acquisition of multiple spectra on a single point would not correspond to an actual single position, but to few closely-spaced positions, invalidating the punctual analysis at high magnification. Considering all the spectra in Fig. 3.17, two “families” of curves are present: the light-colored ones (acquired with lower setpoint voltage), which show a well-defined value for the  $o_h$  peak (comparable to the one of the green spectrum in Fig. 3.16(b)), and the dark-colored ones, which conversely do not exhibit any clear maximum. Also, the first family shows a more defined minimum at 0 eV and the presence of a secondary peak in the neighborhood of  $-1.5$  eV. The curves for “holes” and “edges” do not show substantial differences (regarding the pairs recorded at the same

setpoint bias), even if a more evident  $u_h$  peak is present in the “edges” curve. Another difference is the lower intensity of the “holes” curves. The positive energy side of all the curves in Fig. 3.17, however, is somehow similar to the spectra’s in Fig. 3.16(b), even if those show a more defined peak in that region. Also, the blue curve in Fig. 3.16(b) exhibit a secondary peak similar to the aforementioned one for the light-colored curves in Fig. 3.17.

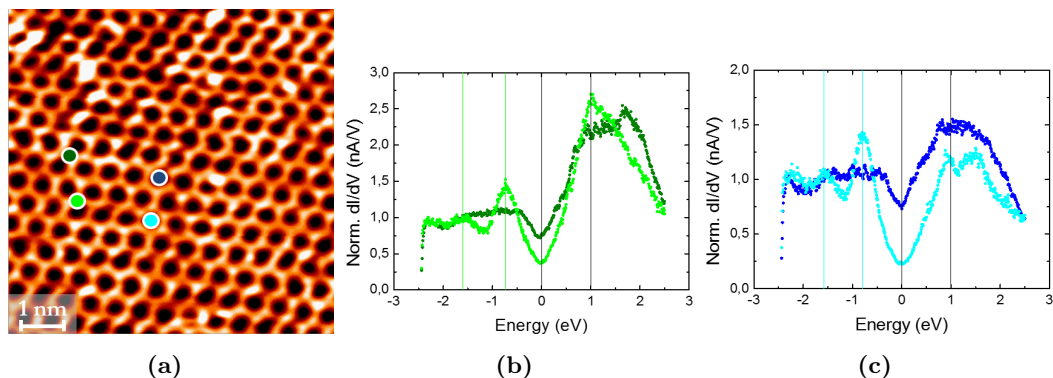


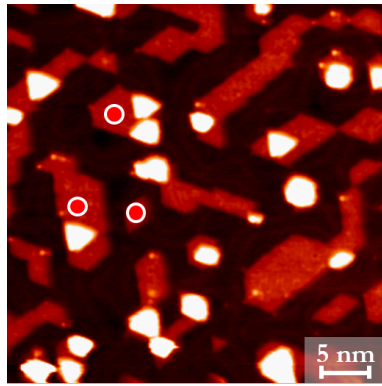
**Figure 3.17:** STS of the honeycomb phase with a W tip at 1.1 MLE; the light-colored spectra have been recorded with setpoint parameters  $V = 0.38$  V,  $I = 1.37$  nA, while the dark-colored ones with  $V = 0.66$  V and  $I = 1.37$  nA. (a) Reference image ( $7.5 \times 7.5$  nm<sup>2</sup>,  $V = 0.36$  V,  $I = 1.37$  nA). (b) STS spectra of the “edges” (light-green:  $n = 4$ ,  $z_0 = 6$  Å,  $o_h = -0.73$  eV,  $u_h = 1$  eV,  $\Delta = 1.73$  eV, secondary peak at  $-1.63$  eV; dark-green:  $n = 7$ ,  $z_0 = 10$  Å). (c) STS spectra of the “holes” (cyan:  $n = 5$ ,  $z_0 = 6$  Å,  $o_h = -0.80$  eV,  $u_h = 1$  eV,  $\Delta = 1.8$  eV, secondary peak at  $-1.58$  eV; blue:  $n = 11$ ,  $z_0 = 11$  Å).

As evident from the previous analysis, it is not easy to find an overall behavior for the honeycomb phase spectra (on the contrary of what happened for the pinwheel phase, as in Sub-section 3.3.4); tip and adsorbates effects may be related to this fickle behavior. However, in most cases the  $o_h$  and  $u_h$  peaks were observed, with the latter having a broader shape and a higher intensity than the former, even though their positions are variable.

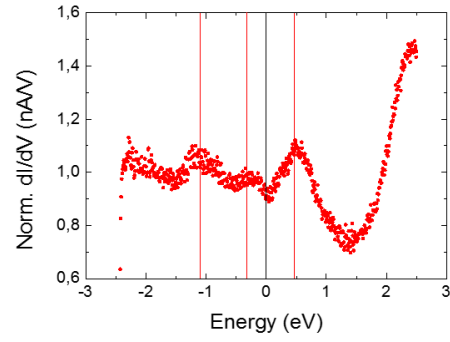
### 3.3.4 Pinwheel

Similarly as the case of Au(111), STS spectra on the pinwheel phase were acquired at low and high coverage, with Cr tips and W ones. At low coverage the analysis was performed as far as possible on the crystallites centers (in this regime, indeed, coalescence still has not begun), in order to prevent edge effects. The results are shown in Figure 3.18. Fig. 3.18(b) shows a spectrum acquired with a Cr tip (its reference image is Fig. 3.18(a)), whereas 3.18(d) refers to the case of W tip (its reference image is Fig. 3.18(c)). In both cases, both  $o_p$  and  $u_p$  are present, as well as secondary peaks; notably,  $u_p$  has almost the same value. In addition, an absolute minimum slightly after 1 eV occurs, but for the spectrum in Fig. 3.18(d) a local minimum at 0 eV is not present, since it is located at slightly higher energy.

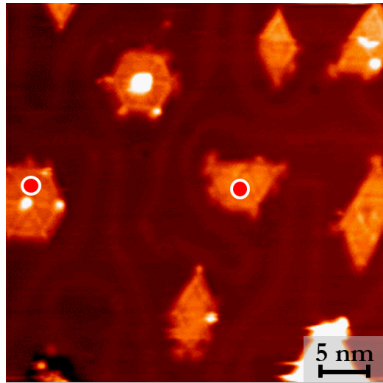
Figure 3.19 shows two examples of the STS analysis of the pinwheel phase at high coverage. Fig. 3.19(b) shows two spectra recorded at 1 MLE with a Cr tip (with Fig. 3.19(a) as reference image) instead of only one; the reason is that the bordeaux spectrum was acquired at the boundary between the pinwheel (on the right) and the



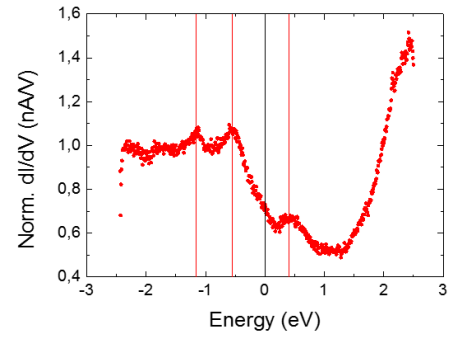
(a) 0.35 MLE, Cr tip



(b) 0.35 MLE, Cr tip



(c) 0.25 MLE, W tip



(d) 0.25 MLE, W tip

**Figure 3.18:** STS of the pinwheel phase at low coverage. 0.35 MLE, Cr tip: (a) reference image ( $40 \times 40 \text{ nm}^2$ ,  $V = 1.4 \text{ V}$ ,  $I = 1.2 \text{ nA}$ ); (b) STS spectrum ( $n = 9$ ,  $z_0 = 5.5 \text{ \AA}$ ,  $o_p = -0.32 \text{ eV}$ ,  $u_p = 0.47 \text{ eV}$ ,  $\Delta = 0.79 \text{ eV}$ , secondary peak at  $-1.1 \text{ eV}$ ). 0.25 MLE, W tip: (c) reference image ( $40 \times 40 \text{ nm}^2$ ,  $V = 1.4 \text{ V}$ ,  $I = 1.2 \text{ nA}$ ); (d) STS spectrum ( $n = 10$ ,  $z_0 = 7.5 \text{ \AA}$ ,  $o_p = -0.55 \text{ eV}$ ,  $u_p = 0.40 \text{ eV}$ ,  $\Delta = 0.95 \text{ eV}$ , secondary peak at  $-1.16 \text{ eV}$ ).

honeycomb (on the left) phases; nonetheless, the spectra show a quite similar behavior, with equal values of both the  $o_p$  and  $u_p$  peaks. Fig. 3.19(d) also shows two spectra; they were acquired at 1.3 MLE with a W tip (the reference image is shown in Fig. 3.19(c)). In this case, the two spectra are slightly shifted relative to one another (the red one at higher energy), the local minimum is not in the  $E = 0$  point and, also, a qualitative difference is present: the red one shows a “shoulder” below  $-1$  eV, which also occurs for the spectrum shown as an example in Fig. 3.13(f), although the latter does not exhibit the  $o_p$  peak. Despite being acquired with the same setpoint voltage and current, this kind of difference in spectra has sometimes occurred (as in Fig. 3.19(d)), so that two distinct “families” of curves have been identified. As a final remark, the purple spectrum shows a secondary peak at about  $-1$  eV, similarly as the spectra at low coverage in Fig. 3.18.

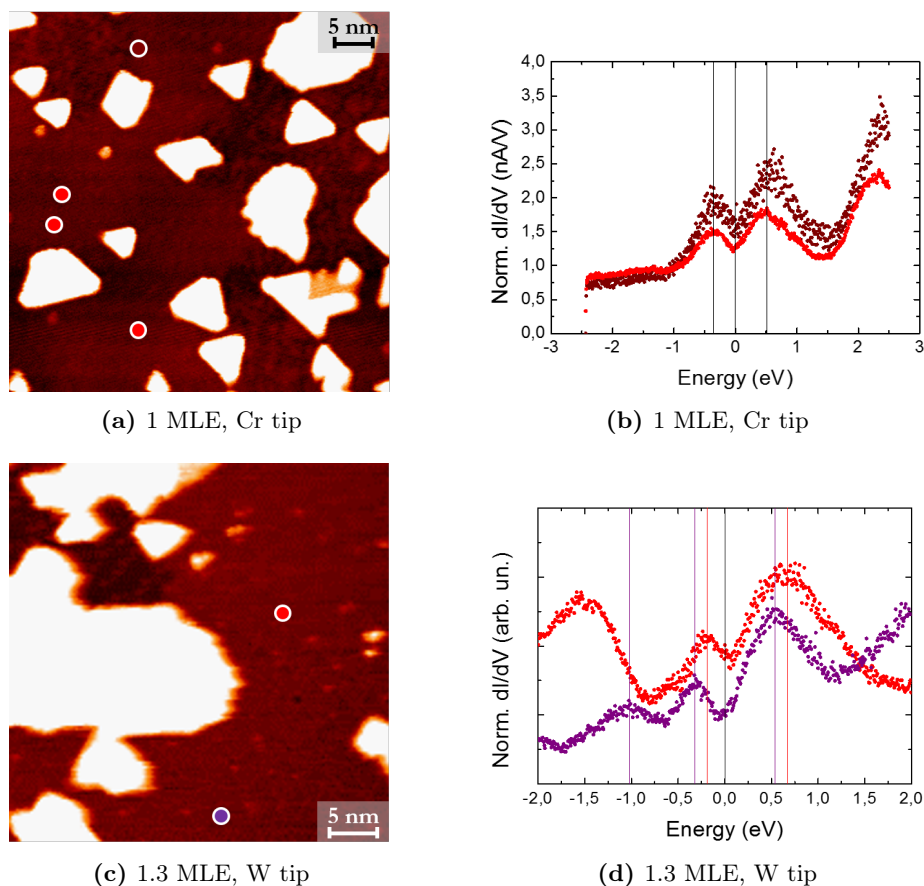


**Figure 3.19:** STS of the pinwheel phase at high coverage. 1 MLE, Cr tip: (a) reference image ( $50 \times 50 \text{ nm}^2$ ,  $V = 0.78 \text{ V}$ ,  $I = 0.58 \text{ nA}$ ), (b) STS spectra (red:  $n = 15$ ,  $z_0 = 7 \text{ \AA}$ ,  $o_p = -0.37 \text{ eV}$ ,  $u_p = 0.51 \text{ eV}$ ,  $\Delta = 0.88 \text{ eV}$ ; bordeaux:  $n = 3$ ,  $z_0 = 7 \text{ \AA}$ ,  $o_p = -0.37 \text{ eV}$ ,  $u_p = 0.51 \text{ eV}$ ,  $\Delta = 0.88 \text{ eV}$ ). 1.3 MLE, W tip: (c) reference image ( $40 \times 40 \text{ nm}^2$ ,  $V = -0.56 \text{ V}$ ,  $I = 0.88 \text{ nA}$ ), (d) STS spectra, acquired with  $V = 0.54 \text{ V}$ ,  $I = 0.36 \text{ nA}$  (red:  $n = 3$ ,  $z_0 = 7 \text{ \AA}$ ,  $o_p = -0.2 \text{ eV}$ ,  $u_p = 0.67 \text{ eV}$ ,  $\Delta = 0.87 \text{ eV}$ ; purple:  $n = 3$ ,  $z_0 = 9 \text{ \AA}$ ,  $o_p = -0.32 \text{ eV}$ ,  $u_p = 0.62 \text{ eV}$ ,  $\Delta = 0.94 \text{ eV}$ , secondary peak at  $-1 \text{ eV}$ ).

Figure 3.20, finally, shows the overall results of the STS analysis at high coverage on the pinwheel phase. In this case, an average between many spectra has been performed, despite the differences in setpoint  $V$  and  $I$ ; this is justified by the fact that these parameters were chosen in a relatively narrow range: for the analysis with Cr tips,

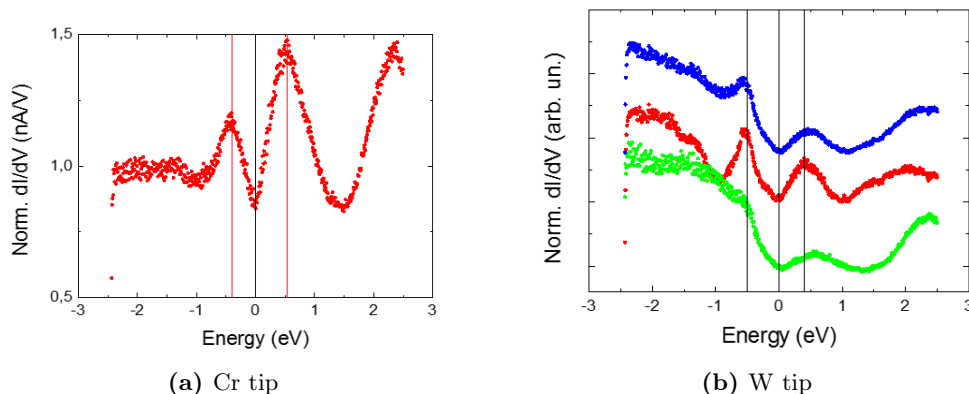


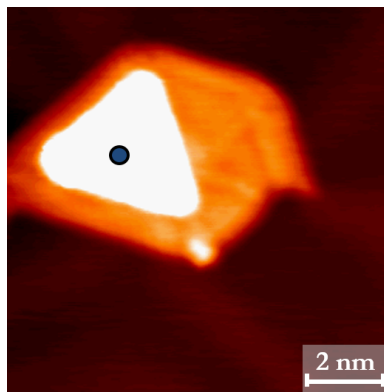
**Figure 3.20:** Comparison between overall averages of spectra acquired with Cr and W tips at high coverage. (a) Cr tip ( $n = 84$ ,  $z_0 = 7 \text{ \AA}$ ,  $o_p = -0.40 \text{ eV}$ ,  $u_p = 0.54 \text{ eV}$ ,  $\Delta = 0.94 \text{ eV}$ ). (b) W tip; blue: total ( $n = 46$ ,  $z_0 = 9 \text{ \AA}$ ,  $o_p = -0.5 \text{ eV}$ ,  $u_p = 0.4 \text{ eV}$ ,  $\Delta = 0.9 \text{ eV}$ ); red: without “shoulder” ( $n = 16$ ,  $z_0 = 7 \text{ \AA}$ ,  $o_p = -0.5 \text{ eV}$ ,  $u_p = 0.4 \text{ eV}$ ,  $\Delta = 0.9 \text{ eV}$ ); green: with “shoulder” ( $n = 30$ ,  $z_0 = 11.5 \text{ \AA}$ ,  $u_p = 0.5 \text{ eV}$ ).

$0.8 \text{ V} \leq V \leq 0.9 \text{ V}$  and  $0.5 \text{ nA} \leq I \leq 0.8 \text{ nA}$ ; with W tips,  $0.5 \text{ V} \leq V \leq 1 \text{ V}$  and  $0.4 \text{ nA} \leq I \leq 0.8 \text{ nA}$ . Fig. 3.20(a) shows the results obtained with Cr tips, while Fig. 3.20(b) shows the ones obtained with W tips. In the first case, the  $o_p$  and  $u_p$  peaks are very well defined and a sort of plateau is present from  $-1 \text{ eV}$  in the negative region. In the second case, three average spectra are shown: the overall one (blue), the one with the “shoulder” (green) and the one without (red). There are some similarities between all the curves, except for the case of the “shouldered” one, which is devoid of the  $o_p$  peak. Also, the behavior in the negative energy region is different as the tip is changed.

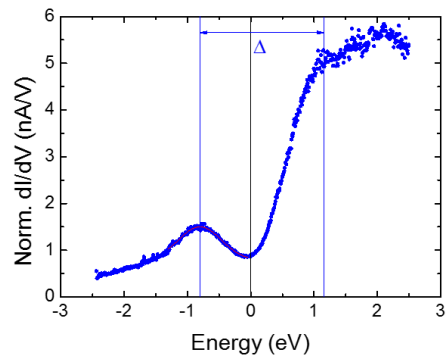
Some common features can be identified from the previous analysis: in all the highlighted cases the  $u_p$  peak is present, whose value is in a neighborhood of  $0.5 \text{ eV}$ ; with Cr tips, both at low and high coverage, the  $o_p$  peak is always distinguishable, whereas this is not the case of the W tip; however, at low coverage both the peaks are less prominent. The peculiar behavior of the “shouldered” spectra with the W tip, accordingly, may be ascribed to some tip electronic configuration, which tends to change during the measurements.

### 3.3.5 Triangular

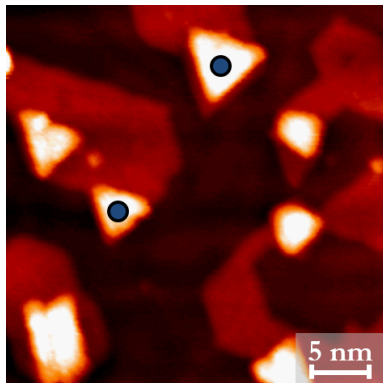
The STS analysis for the triangular phase was also performed at low and high coverage, with Cr and W tips. Figure 3.21 shows the results of the low coverage analysis. Fig. 3.21(b) shows a spectrum acquired with a Cr tip and with a depiction of the quantity  $\Delta$ ; its reference image is Fig. 3.21(a). Fig. 3.21(d), on the other hand, refers to the W tip and to the STM image in Fig. 3.21(c). The two spectra have the same qualitative trend, however some minor differences occur: the second one shows a lower  $\Delta$ , a decrease after  $2 \text{ eV}$  and the local minimum is not centered in 0. For this phase and the row, also, the quantity  $\Delta$  in our analysis has been considered more important for a few reasons: its value is a little higher than for the previous phases (honeycomb and pinwheel), the  $u_t$  peak (or  $u_r$ ) usually is broadened and less defined and, finally, the local minimum at the Fermi energy can assume a zero value, resembling the presence of an actual energy gap in the LDOS.



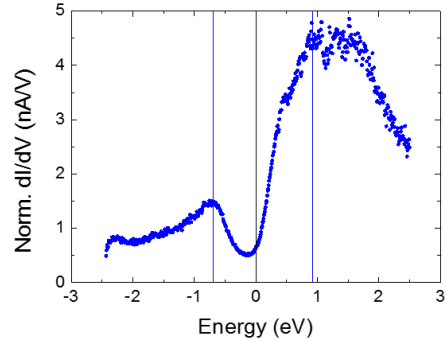
(a) 0.25 MLE, Cr tip



(b) 0.25 MLE, Cr tip



(c) 0.35 MLE, W tip



(d) 0.35 MLE, W tip

**Figure 3.21:** STS of the triangular phase at low coverage. 0.25 MLE, Cr tip: (a) reference image ( $10 \times 10 \text{ nm}^2$ ,  $V = 1 \text{ V}$ ,  $I = 0.8 \text{ nA}$ ), (b) STS spectrum ( $n = 5$ ,  $z_0 = 7.5 \text{ \AA}$ ,  $o_t = -0.8 \text{ eV}$ ,  $u_t = 1.16 \text{ eV}$ ,  $\Delta = 1.96 \text{ eV}$ ). 0.35 MLE, W tip: (c) reference image ( $33 \times 33 \text{ nm}^2$ ,  $V = -0.8 \text{ V}$ ,  $I = 1.1 \text{ nA}$ ), (d) STS spectrum ( $V = 0.9 \text{ V}$ ,  $I = 1.7 \text{ nA}$ ,  $n = 6$ ,  $z_0 = 6 \text{ \AA}$ ,  $o_t = -0.70 \text{ eV}$ ,  $u_t = 0.92 \text{ eV}$ ,  $\Delta = 1.62 \text{ eV}$ ).

The STS analysis at high coverage is summarized in Figure 3.22; here, Fig. 3.22(a) is the reference image for the spectrum in Fig. 3.22(b), acquired with a Cr tip, Fig. 3.22(c)(I) is the reference image of the cyan spectrum in Fig. 3.22(d) and, similarly, Fig. 3.22(c)(II) is the reference image of the purple spectrum in Fig. 3.22(d). These two spectra, both acquired with a W tip, are shifted by 2 nA/V relative to one another for the sake of clarity. The qualitative trend is still the same as previously, with a higher  $u_t$  than  $o_t$  and with a value of  $\Delta$  at most equal to 2 eV. However, the minimum at  $E = 0$  is closer (Fig. 3.22(b)) or even equal (Fig. 3.22(d)) to the 0 value, thus resembling a sort of energy gap; this effect apparently does not occur at low coverage (Figs. 3.21(b) and 3.21(d)). Finally, an attempt to correlate the value of  $\Delta$  with the surface area of the triangular island was performed, but a proportionality was not found.

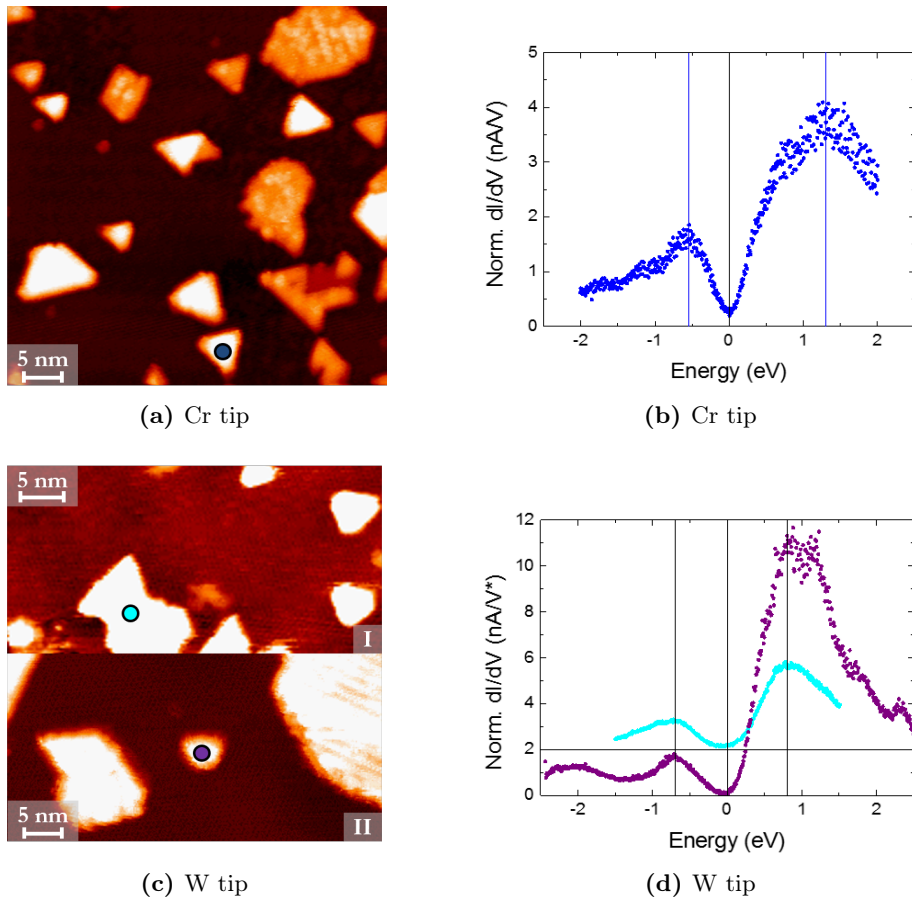


**Figure 3.22:** STS of the triangular phase at high coverage. 1 MLE, Cr tip: (a) reference image ( $50 \times 50 \text{ nm}^2$ ,  $V = 0.78 \text{ V}$ ,  $I = 0.58 \text{ nA}$ ); (b) STS spectrum ( $n = 3$ ,  $z_0 = 13.5 \text{ \AA}$ ,  $o_t = -0.54 \text{ eV}$ ,  $u_t = 1.3 \text{ eV}$ ,  $\Delta = 1.84 \text{ eV}$ ). W tip: (c) reference images; I: 1.1 MLE ( $43 \times 21.5 \text{ nm}^2$ ,  $V = 0.76 \text{ V}$ ,  $I = 0.38 \text{ nA}$ ); II: 1.3 MLE ( $50 \times 25 \text{ nm}^2$ ,  $V = 0.61 \text{ V}$ ,  $I = 0.82 \text{ nA}$ ); (d) STS spectra; the “\*” means that the  $y$  axis for the cyan curve is shifted upwards of 2 nA/V. Cyan curve: reference image (c)I ( $V = 0.3 \text{ V}$ ,  $I = 0.4 \text{ nA}$ ,  $n = 3$ ,  $z_0 = 13 \text{ \AA}$ ,  $o_t = -0.70 \text{ eV}$ ,  $u_t = 0.79 \text{ eV}$ ,  $\Delta = 1.49 \text{ eV}$ ); purple curve: reference image (c)II ( $n = 3$ ,  $z_0 = 12 \text{ \AA}$ ,  $o_t = -0.70 \text{ eV}$ ,  $u_t = 0.94 \text{ eV}$ ,  $\Delta = 1.64 \text{ eV}$ ).

### 3.3.6 Row

The row phase was investigated with the STS technique both with Cr and W tips; the most relevant examples are shown in the following. Figure 3.23 shows the spectra acquired with a Cr tip (Fig. 3.23(a)) and with a W one (Fig. 3.23(b)). Their qualitative trend is the same and it resembles the one of the triangular phase (Sub-section 3.3.5), having a higher LDOS in the unoccupied states rather than in the occupied ones. Notably, the local minimum at  $E = 0$  corresponds with an actual zero value of the normalized  $dI/dV$  and the value of  $\Delta$  goes from 2.18 eV (Fig. 3.23(a)) to 3.06 eV (orange spectrum in Fig. 3.23(b)). Additional features in spectra after 1.5 eV are also present in most cases, whereas in the negative region the curves usually follow a smoother path.

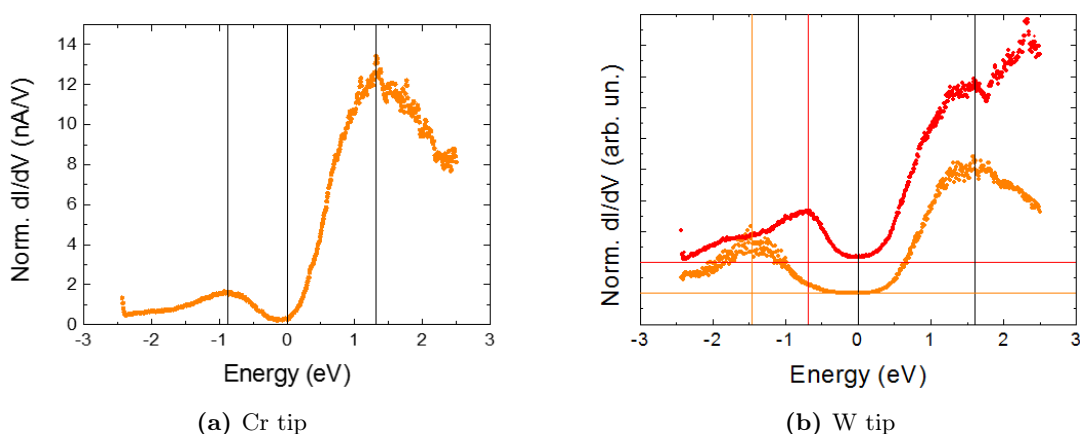


**Figure 3.23:** STS of the row phase. **(a)** STS spectrum at 1 MLE with Cr tip ( $V = 0.9$  V,  $I = 0.8$  nA,  $n = 3$ ,  $z_0 = 10.5$  Å,  $o_r = -0.87$  eV,  $u_r = 1.31$  eV,  $\Delta = 2.18$  eV). **(b)** STS spectra with W tip; the colored horizontal lines represent the zero height for the corresponding curve (orange: 1.3 MLE,  $V = 0.6$  V,  $I = 0.8$  nA,  $n = 6$ ,  $z_0 = 5.25$  Å,  $o_r = -1.47$  eV,  $u_r = 1.59$  eV,  $\Delta = 3.06$  eV; red: 1.3 MLE,  $V = 1$  V,  $I = 0.4$  nA,  $n = 10$ ,  $z_0 = 7.5$  Å,  $o_r = -0.69$  eV,  $u_r = 1.62$  eV,  $\Delta = 2.31$  eV).

Similarly as the honeycomb phase analysis, a more detailed STS study was performed; notably, spectra on the so-called “bright” rows and “dark” ones have been recorded with the help of high-resolution images. The procedure followed is quite similar to the one employed for the “edges” and “holes” of the honeycomb phase. Fig. 3.24(a) shows an STM image of the investigated portion of row phase; only two colored circles are present as examples of “bright” and “dark” rows. Fig. 3.24(b) shows the spectra acquired for these two variations and Fig. 3.24(c) shows the normalized average of all the  $dI/dV$  curves. Contrary to the previous spectra for the same phase, the qualitative trend is very smooth and more regular; two clear  $o_r$  and  $u_r$  peaks are present and the normalized  $dI/dV$  curves go to zero both in their surroundings and in the Fermi energy. In addition, the “dark” rows’ spectrum is slightly shifted towards negative energies with respect to the other one and also shows a higher  $u_r$ . Another difference with respect to the previous row spectra is a slightly lower value of  $\Delta$  (not greater than 2 eV). In addition, Fig. 3.24(c) shows the normalized average of all the STS spectra acquired in this analysis, without discerning between “bright” and “dark” rows; this has the aim to establish a comparison between the previous spectra on the row phase (Figs. 3.23), which also do not imply a different treatment for “bright” and

“dark” rows. However, the difference from those ones is quite clear, since they are more similar to the spectra of the triangular phase from a qualitative point of view (Figs. 3.21-3.22); nonetheless, the peaks’ positions are different from the triangular phase and the value of  $\Delta$  for the spectra in Figs. 3.23 and 3.24 is comparable (in most cases slightly lower than 2 eV). Up to now, no clear explanation of the peculiar trend of the spectra in Fig. 3.24 has been supplied; first of all, the measurement parameters were not different from the other cases; secondly, the crystallite on which the spectra were acquired had similar dimensions and thickness to the previous cases. However, while the previous measurements were performed on a relatively large area of row phase islands, the ones reported in Fig. 3.24 were performed in a very small portion of the crystallite; in the first case, spectra may have been recorded in the surroundings of adsorbates, whereas in the second case they have been acquired with more accuracy; this may be a possible hypothesis on the different behavior of these STS spectra, even if it must be supported by more experimental and/or theoretical data to be confirmed. On the other hand, the slight shift between “bright” and “dark” rows spectra may be ascribed to the structural hypothesis mentioned in Sub-section 3.2.2, that is to say the lack of one Ti atoms row in the “dark” rows. This conclusion, of course, requires a theoretical basis in order to be confirmed.

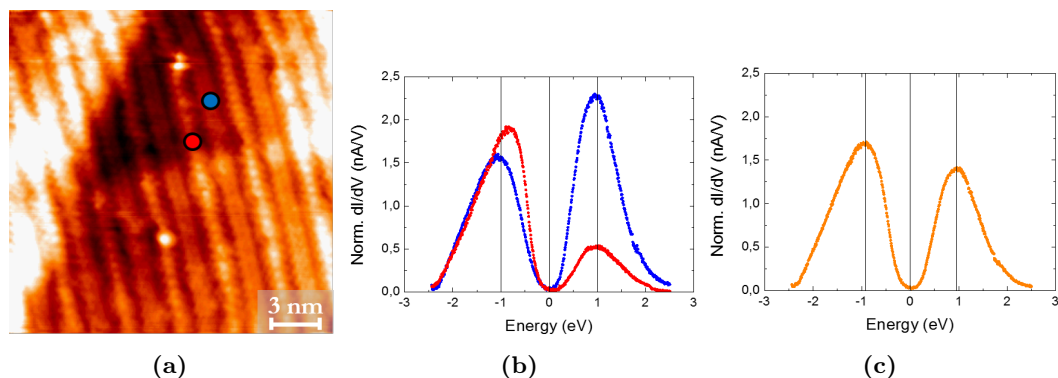


**Figure 3.24:** STS of the row phase with a W tip at 1.3 MLE. (a) Reference image ( $20 \times 20 \text{ nm}^2$ ,  $V = 0.86 \text{ V}$ ,  $I = 1.24 \text{ nA}$ ). (b) STS spectra of the “bright” rows and “dark” rows, both with setpoint  $V = 0.86 \text{ V}$  and  $I = 0.72 \text{ nA}$ ; “bright” rows: red ( $n = 3$ ,  $z_0 = 17 \text{ \AA}$ ,  $o_r = -0.82 \text{ eV}$ ,  $u_r = 0.88 \text{ eV}$ ,  $\Delta = 1.7 \text{ eV}$ ); “dark” rows: blue ( $n = 15$ ,  $z_0 = 17 \text{ \AA}$ ,  $o_r = -1.06 \text{ eV}$ ,  $u_r = 0.95 \text{ eV}$ ,  $\Delta = 2.0 \text{ eV}$ ). (c) Average normalized spectrum ( $n = 18$ ,  $z_0 = 17 \text{ \AA}$ ,  $o_r = -0.92 \text{ eV}$ ,  $u_r = 0.95 \text{ eV}$ ,  $\Delta = 1.88 \text{ eV}$ ).

### 3.3.7 Final comparisons

After the previous detailed analysis, an overview for all the  $\text{TiO}_x$  phases is now beneficial in order to make some final comparisons and considerations. Figure 3.25 shows four STS spectra taken as examples from the ones shown before; they all refer to the high-coverage analysis, since in that case all the phases are present and no substantial differences from the low-coverage situation have come to light; more precisely, for the pinwheel phase at low coverage an absolute minimum is observed in the unoccupied states and the peaks are less intense with respect to the high coverage spectra, whereas for the triangular phase an almost zero value at the Fermi energy is observed only at high coverage. Table 3.2, in addition, collects the STS data presented in the previous sections on the  $\text{TiO}_x$  phases and it can help us finding some general similarities or differences

between them. The spectra can be somehow grouped in first-layer ones (pinwheel and honeycomb, Figs. 3.25(a)-3.25(b) respectively) and second-layer ones (triangular and row, Figs. 3.25(c)-3.25(d) respectively). This is justified by the fact that the former show both (or at least one of) the two  $o_x$  and  $u_x$  peaks in more definite positions (especially regarding the pinwheel phase), have a non-zero value at  $E = 0$  and have a slightly lower value of  $\Delta$ ; the latter also exhibit the  $o_x$  and  $u_x$  peaks, but they have more variable positions and especially  $u_x$  is usually broader; in addition, with a growing coverage these second-layer phases tend to assume a zero value at the Fermi energy, suggesting a minimum of the LDOS in this point. Also for the second-layer phases, however, a clear difference from the bulk energy gap value of  $\text{TiO}_2$  ( $E_g = 3.1$  eV) exists, but they are closer to that situation. An explanation for this effect may be that the pinwheel and honeycomb phases, since they directly grow on the Au(111) surface, are heavily influenced by the electronic properties of the substrate, which obviously does not exhibit any energy gap being a metal; conversely, triangular and row phases do not grow on the Au(111) surface, so they are less affected by its electronic properties. This hypothesis, even though it seems quite reasonable, needs *ab initio* calculations in order to be confirmed.

In addition, a slight difference in the spectra has been observed comparing the ones acquired with Cr tips rather than W tips; however, a deeper study should be carried on in order to ascertain the influence of the tip's electronic structure on the STS measurements on the  $\text{TiO}_x/\text{Au}(111)$  phases.

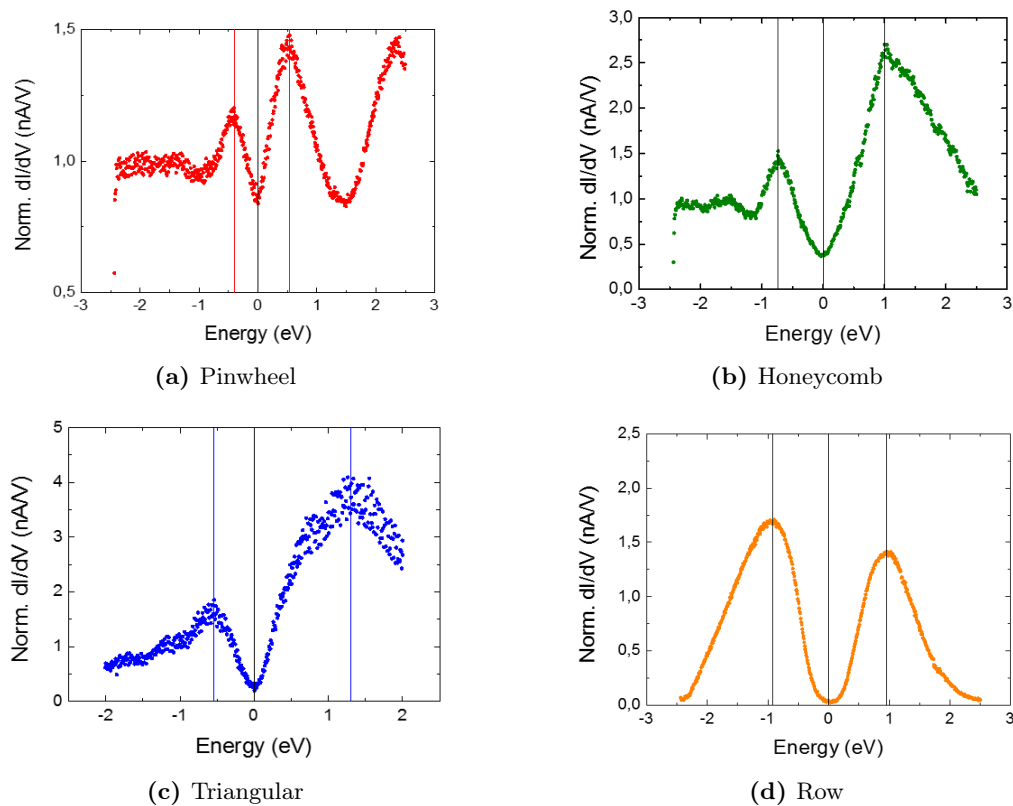


**Figure 3.25:** STS spectra of the different  $\text{TiO}_x$  phases. (a) Pinwheel (same as Fig. 3.19(b)); (b) Honeycomb (from Fig. 3.17(b)); (c) Triangular (same as Fig. 3.22(b)); (d) Row (same as Fig. 3.24(c)).

**Table 3.2:** Summary of the STS data on the  $\text{TiO}_x/\text{Au}(111)$  phases presented in this section.

Source	Phase	Coverage (MLE)	Tip	$V$ (V)	$I$ (nA)	$n$	$o_x$ (eV)	$u_x$ (eV)	$\Delta$ (eV)	Sec. peak(s)
Fig. 3.16(a)		1	Cr	0.9	0.8	24		0.35; 1.13		
Fig. 3.16(b)(1)		1.1	W	0.3	0.4	9	-0.74	0.84	1.58	
Fig. 3.16(b)(2)		1.3	W	0.6	0.8	6	-0.39	0.75	1.09	✓
Fig. 3.17(b)(1)	Honeycomb	1.1	W	0.38	1.37	4	-0.73	1	1.73	✓
Fig. 3.17(b)(2)		1.1	W	0.66	1.37	7				
Fig. 3.17(c)(1)		1.1	W	0.38	1.37	5	-0.8	1	1.8	✓
Fig. 3.17(c)(2)		1.1	W	0.66	1.37	11				
Fig. 3.18(b)		0.35	Cr	1.4	1.2	9	-0.32	0.47	0.79	✓
Fig. 3.18(d)		0.25	W	1.4	1.2	10	-0.55	0.4	0.95	✓
Fig. 3.13(f)		1.3	W	0.6	0.8	22		0.5		
Fig. 3.19(b)(1)		1	Cr	0.78	0.58	15	-0.37	0.51	0.88	
Fig. 3.19(b)(2)		1	Cr	0.78	0.58	3	-0.37	0.51	0.88	
Fig. 3.19(d)(1)	Pinwheel	1.3	W	0.54	1.36	3	-0.2	0.67	0.87	
Fig. 3.19(d)(2)		1.3	W	0.54	1.36	3	-0.32	0.62	0.94	✓
Fig. 3.20(a)			Cr			84	-0.4	0.54	0.94	
Fig. 3.20(b)(1)			W			46	-0.5	0.4	0.9	
Fig. 3.20(b)(2)			W			16	-0.5	0.4	0.9	
Fig. 3.20(b)(3)			W			30		0.5		
Fig. 3.21(b)		0.25	Cr	1	0.8	5	-0.8	1.16	1.96	
Fig. 3.21(d)		0.35	W	0.9	1.7	6	-0.7	0.92	1.62	
Fig. 3.22(b)	Triangular	1	Cr	0.78	0.58	3	-0.54	1.3	1.84	
Fig. 3.22(d)(1)		1.1	W	0.3	0.4	3	-0.7	0.79	1.49	
Fig. 3.22(d)(2)		1.3	W	0.61	0.82	3	-0.7	0.94	1.64	
Fig. 3.23(a)		1	Cr	0.9	0.8	3	-0.87	1.31	2.18	
Fig. 3.23(b)(1)		1.3	W	0.6	0.8	6	-1.47	1.59	3.06	
Fig. 3.23(b)(2)		1.3	W	1	0.4	10	-0.69	1.62	2.31	
Fig. 3.24(b)(1)	Row	1.3	W	0.86	0.72	3	-0.82	0.88	1.7	
Fig. 3.24(b)(2)		1.3	W	0.86	0.72	15	-1.06	0.95	2	
Fig. 3.24(c)		1.3	W	0.86	0.72	18	-0.92	0.95	1.88	

### 3.4 Discussion

From the experimental results about the  $\text{TiO}_x/\text{Au}(111)$  system illustrated in Sections 3.2 and 3.3, some considerations can be made in the present section, following the same order as the previous explanation. Even if, from the morphological and structural point of view, most of the experimental observations in this thesis work have confirmed the previous ones<sup>[13]</sup>, some issues have been solved, so the results will be briefly reviewed also from this point of view considering each observed phase.

LEED measurements have shown a  $(2 \times 2)$  reconstruction for the honeycomb phase, which previously was only hypothesized. Notably, the *kagomé*-like structure has been unexpectedly observed, probably due to a peculiar tip electronic state; this can be considered as an evidence of the atomic model of this phase proposed by Wu *et al.*<sup>[12]</sup>. This structure, thus, turns out to be similar to the *k*- $\text{TiO}_x$  phase observed for the  $\text{TiO}_x/\text{Pt}(111)$  system by the group of Granozzi<sup>[52,54]</sup>; in both cases the stoichiometry is  $\text{Ti}_2\text{O}_3$ , but for the *k*- $\text{TiO}_x$  phase the overlayer is incommensurate with respect to the substrate  $((2.15 \times 2.15)$  reconstruction). This difference may be explained taking into account the argumentation reported by Netzer<sup>[76]</sup>: the substrate affinity towards oxygen and the deposited metal–substrate bond (before oxidation) are crucial factors for the stability of the oxide/metal system. In this framework, since Au is nobler than Pt, it barely binds with oxygen, so a Ti-O-Au stacking is totally unexpected for this system. In addition, since the Au-Ti affinity is quite strong<sup>[10,67]</sup>, it is rather difficult that incommensurate  $\text{TiO}_x$  overlayers can grow, on the contrary of the already mentioned incommensurate phases exhibited by the  $\text{TiO}_x/\text{Pt}(111)$  system<sup>[52,54,56]</sup>.

Considering the pinwheel phase, LEED data have played an important role also in this case, showing the  $(\sqrt{111} \times \sqrt{111})R19.1^\circ$  reconstruction for this phase, while a  $(\sqrt{133} \times \sqrt{133})R17.5^\circ$  reconstruction was previously attributed to it only on the basis of STM data; the unit vector is 30.6 Å long and the interatomic distance is 3.43 Å. The structural model is still based on a Moiré effect interpretation and has been obtained comparing the LEED data to atomically resolved STM images. As already mentioned, however, no information on the position of oxygen atoms is still available, so we did not make any hypothesis about the stoichiometry of this phase. Wu *et al.*<sup>[12]</sup>, on the other hand, conjectured a TiO stoichiometry by comparing this system to the pinwheel structure for the  $\text{VO}_x/\text{Rh}(111)$  case<sup>[72,73]</sup>. Nonetheless, only with accurate theoretical studies an unambiguous solution to this matter can be found.

In the case of the triangular phase, the previous observations have been confirmed<sup>[13]</sup>; in addition, it was already reported in the previous literature<sup>[10,12]</sup> and, notably, Potapenko *et al.*<sup>[10]</sup> identified these crystallites as bulk rutile (100) surface with a  $(1 \times 2)$  reconstruction; on the other hand, Wu *et al.*<sup>[12]</sup> did not make any structural assumption, but measured a  $\text{TiO}_{1.3}$  stoichiometry, thanks to AES data, contrary to the  $\text{TiO}_2$  hypothesis. In our work, no assumption on the stoichiometry and the structure of the triangular phase has been made, since no clear experimental evidences could be found; however, it can be considered as a 3D structure with hexagonal symmetry.

If, on the one hand, atomic resolution for the triangular phase still has not been attained, on the other hand it did for the row phase, showing a rectangular unit cell with dimensions  $(5.7 \pm 0.2) \times (58 \pm 1)$  Å<sup>2</sup>. Nevertheless, no information about the stoichiometry of this phase is available, nor a structural model does, so both AES

measurements and theoretical simulations should provide more information about these aspects. As already mentioned in Sub-section 3.2.1, however, the synthesis of a single  $\text{TiO}_x$  phase was not obtained in our work, which is a requirement for an analysis of the row phase with AES, as well as for all the other phases. Regarding the LEED technique, instead, the presence of a single phase is not strictly required, but at least a comparable quantity with respect to honeycomb and pinwheel phases is needed for the row one to give contribution to the LEED pattern.

STM measurements have also been obtained for the needle phase, which is a sort of “elusive” phase: for example, it was not observed at all in the work of Wu *et al.*<sup>[12]</sup> and we seldom detected it (this is the reason why no STS data have been collected on it, as already mentioned in Section 3.3). Nonetheless, high-resolution images for this phase have been obtained finding a rectangular unit cell also in this case, with dimensions  $(3.2 \pm 0.2) \times (5.2 \pm 0.1) \text{ \AA}^2$ . A peculiar feature of the needle phase, however, is its 3D morphology; this may suggest that it represents a sort of nanowire-like  $\text{TiO}_2$  structure growing on the first  $\text{TiO}_x$  layer.

Except the needle phase, all the other ones have been analyzed with the STS technique, at low coverage (sub-monolayer regime) and relatively high coverage (1–1.5 MLE), with Cr and W tips. As a first-order approximation, we can split them into two families: first-layer ones (pinwheel and honeycomb), with 2D structure, and second-layer ones (triangular and row), with 3D structure, as already mentioned in Sub-section 3.3.7. This is justified not only by the obvious morphological argument, but also by a spectroscopic behavior; indeed, roughly all the spectra exhibit two peaks (one in the occupied states,  $o_x$ , and one in the unoccupied ones,  $u_x$ ), as manifest from Table 3.2, even if for the second-layer phases an absolute minimum of the LDOS at the Fermi energy tends to appear as the coverage is increased. In other words, having defined  $\Delta = u_x - o_x$ ,  $\Delta$  is greater for the second-layer phases with respect to the first-layer ones, although between the triangular and honeycomb phases only a slight difference occurs. This effect may be related to a stronger influence of the metallic substrate for the pinwheel and honeycomb phases, which in turn becomes lower for the triangular and row phases. In the present analysis, moreover, an averaging procedure has usually been performed, considering spectra in equivalent positions of a certain  $\text{TiO}_x$  phase, but in two cases (honeycomb and row) a more detailed analysis has been performed, showing slight local differences in the spectra. A prominent outcome from this analysis is represented by the spectra on the row phase, which show a peculiar and very smooth behavior, differently from all the other spectra, with two very defined  $o_r$  and  $u_r$  peaks which arise from a zero-value background; in addition, a slight shift between the curves corresponding to “bright” rows and “dark” rows has been found. This measurement, however, has not yet a clear explanation, even if, as mentioned in Sub-section 3.3.6, such a local investigation may have permitted to avoid the adsorbates on the surface of the row island, thus obtaining spectra of “better quality”.

This kind of analysis has been previously performed for the Ti/Au(111) system<sup>[67]</sup> but not for the  $\text{TiO}_x/\text{Au}(111)$  one (at least, to this author’s knowledge), so this aspect of the present thesis work may be more deeply investigated, for example performing STS analysis with tips of different materials (e.g. Mo, Co), making a more accurate punctual analysis for each phase, performing the measurements on the needle phase or at very low temperatures (e.g. by means of liquid He).

## Conclusions and perspectives

In this thesis work a study on morphological, structural and electronic properties of 2D and 3D nanostructures of titanium oxide on the Au(111) surface is reported; this has been achieved by means of LEED and mainly STM-STs techniques.

The growth of  $\text{TiO}_x$  on the Au(111) surface has been studied mainly in two coverage regimes, namely around 0.3 MLE and 1–1.5 MLE. This system has been obtained by electron-beam evaporation on the sputtered and reconstructed Au(111) surface, followed by oxygen exposure ( $\sim 500$  L) and by an annealing step at 850 K from 15 to 25 minutes long, depending on the coverage. The study of the growth of  $\text{TiO}_x/\text{Au}(111)$  phases has confirmed the results obtained in a previous thesis work<sup>[13]</sup>: the first  $\text{TiO}_x$  phase, in order of appearance, is the *pinwheel* one ( $\sim 0.2$  MLE), which perturbs the surface reconstruction of Au, leading to a distortion of the discommensuration lines. Afterwards, crystallites of the *triangular* phase grow on the pinwheel ones ( $\sim 0.4$  MLE). After 1 MLE, on the other hand, five different phases appear simultaneously: *pinwheel*, *triangular*, *honeycomb*, *row* and *needle*.

As a starting point for the structural analysis, the LEED measurements have provided information on the symmetry of the surface layers at different coverage, so that, comparing these data to atomically resolved STM image, the structure of some phases have been determined. A  $(\sqrt{111} \times \sqrt{111})R19.1^\circ$  reconstruction, with hexagonal symmetry, has been assigned to the pinwheel phase, on the basis of a Moiré model. This phase is a 2D first-layer phase, as the honeycomb one, which appears after 0.8 MLE; it is, also, characterized by a hexagonal symmetry, with  $(2 \times 2)$  reconstruction, and for this phase the  $\text{Ti}_2\text{O}_3$  stoichiometry has been hypothesized, as first proposed by Wu *et al.*<sup>[12]</sup>. Triangular crystallites, furthermore, can grow on top of both the previous phases and exhibit some kind of 3D structure. The row phase, instead, appears after 1 MLE in the form of large islands (with a typical area of 400-1000  $\text{nm}^2$ ); it shows a multi-layer structure with rectangular symmetry and its unit cell has been identified. Finally, the needle phase appears as a kind of nanowires with a cylindrical shape and rectangular unit cell. The first-layer phases, namely pinwheel and honeycomb, have been observed for the same material on other substrates (*w*- $\text{TiO}_x/\text{Pt}(111)$ <sup>[6]</sup>) and for other transition metal oxides on metallic substrates (such as  $\text{VO}_x/\text{Pd}(111)$ <sup>[57]</sup>).

In addition, STS analysis has been performed on four of these phases for the first

time, to this author's knowledge; the analysis has been undertaken at low and high coverage, both with Cr and W tips, and a normalization procedure (with the Ukraintsev method) has also been applied, in order to directly relate the STS spectra to the local density of states (LDOS) of the sample. STS measurements on the Au(111) surface have shown that its electronic behavior is not substantially perturbed by the presence of the  $\text{TiO}_x$  phases above; on the other hand, spectra on pinwheel, honeycomb, triangular and row phases exhibit two main peaks around the Fermi energy, in which a local (or absolute) minimum is found; for the last two, in particular, this minimum tends to assume a zero value at increasing coverage.

The investigation on the  $\text{TiO}_x/\text{Au}(111)$  system by means of both STM and STS can be further developed in various directions. One of the most important shortcomings in the knowledge of this system is on the theoretical point of view; for example, the location of oxygen atoms in the pinwheel phase is still unclear and the same holds for the origin of the peaks in STS spectra; indeed, DFT simulations of the structural and electronic properties of these phases are being carried on. Another useful analysis may be the Auger spectroscopy, with the aim to understand the stoichiometry of the observed phases. This kind of measurement would be eased in the presence of a single  $\text{TiO}_x$  phase; so, another development could be the identification of a deposition/post-annealing procedure able to isolate a single  $\text{TiO}_x/\text{Au}(111)$  phase. Moreover, the growth at higher coverage can be investigated and it may provide data on the appearance of bulk  $\text{TiO}_2$  structures. The same material on other substrates may be studied, such as ultrathin  $\text{TiO}_x$  films on graphite or Si(111). Finally, the same  $\text{TiO}_x/\text{Au}(111)$  system can be realized with a different experimental technique, such as pulsed laser deposition (PLD), and the STM-STS characterization may unveil its different morphological, structural and electronic properties.

Considering, more precisely, the electronic properties of  $\text{TiO}_x/\text{Au}(111)$ , the analysis reported in this thesis work can be improved by an atomically resolved analysis on each phase, to prove the dependence of STS measurements on the different atomic sites; this can be eased going even at lower temperature than the one employed in this analysis, e.g. with liquid He. Another issue is the analysis with tips made of different materials, such as Mo, Fe, Ta, whose manufacturing is being developed. These materials, indeed, show a higher oxidation resistance than the currently used W and Cr tips and may be beneficial in order to discriminate the influence of the tip on STS spectra of the  $\text{TiO}_x$  phases. Finally, other normalization techniques may be applied in order to recover the LDOS of the  $\text{TiO}_x$  phases in a more satisfactory way; indeed, this kind of investigation is currently being studied.

## Experimental details

The experimental measurements reported in this thesis were performed in the Micro and Nanostructured Materials Laboratory (Nanolab) of Politecnico di Milano, Department of Energy. The experimental apparatus is composed by two ultra-high vacuum (UHV) chambers (base pressure  $\sim 5 \times 10^{-10}$  mbar): an analysis chamber, which contains the measuring system for STM-STS analysis, and a surface preparation chamber with the facilities for surface preparation: the ion gun for surface sputtering and cleaning, a resistive sample heater and a thermal evaporator. In addition, a facility for low-energy electron diffraction (LEED) and Auger electron spectroscopy (AES) is also present. The two chambers are reported in Figure A.1.

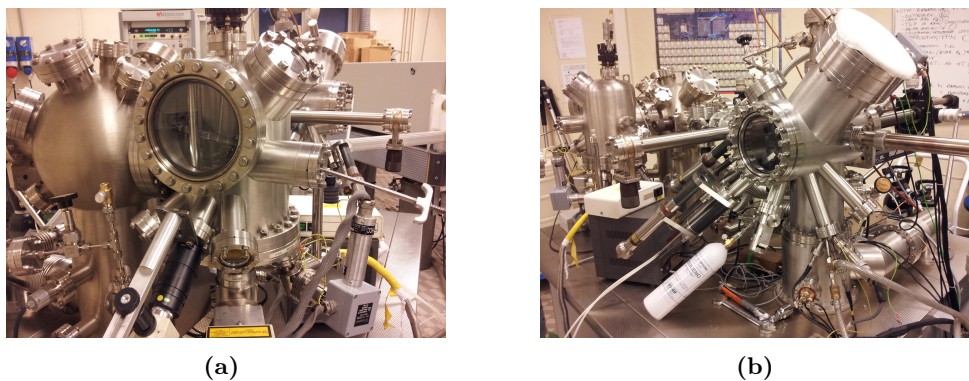


**Figure A.1:** STM apparatus: (a) analysis chamber; (b) preparation chamber.

### A.1 Vacuum system

In the surface analysis the vacuum regime is required to prevent contamination due to gases in the atmosphere that may alter the sample; just think that, according to the kinetic theory of gases<sup>[48]</sup>, the time needed to cover an area of  $1 \text{ cm}^2$  composed of about  $10^{15}$  atoms is given by:

$$t = \frac{10^{15}}{3.513 \times 10^{22}} \frac{\sqrt{MT}}{p} \quad (\text{A.1})$$

where  $p$  is the pressure expressed in Torr,  $M$  is the molar mass (in grams) of the gas and  $T$  is the temperature in Kelvin. Assuming a unitary *sticking* coefficient, the Equation (A.1) shows that at the atmospheric pressure  $t = 3.5 \times 10^{-9}$  s, while at pressure of  $10^{-10}$  mbar this time rises to around 7 hours. For this reason, both the measuring and the deposition chambers are equipped with two separate pumping systems, the first one with the most stringent requirements of vacuum to ensure a sufficient time to analyze the sample.

The measuring chamber is kept in UHV regime and it is provided with four different pumps, each of them able to reach a distinct vacuum level. The first vacuum level is achieved with a rotary pump, also called primary pump, able to pump until  $10^{-2}$  mbar. The operating principle of this pump is mechanical and it is based on gas transfer: a rotary piston removes the gas molecules from the pumped volume and convey them to the external ambient in one or more stages of compression. Rotary pumps are frequently used to produce the minimal vacuum required to operate turbomolecular pumps, which can then attain far lower pressures. Beyond the level reached by the rotary pump there is a change in the gas molecules behavior passing from a fluid-dynamic regime to a molecular one. At this stage, the turbomolecular pump operates: it consists of a structure with rotors and stators designed to capture gas molecules pushing them towards the downstream rotary pump. The turbomolecular pump imparts a preferred direction to molecular motion by impact with a rapidly whirling turbine rotor spinning at rates up to 50000 rpm. The cascade of turbomolecular and rotary pumps can reach a pressure of about  $10^{-9}$  mbar. To get the pressure levels that characterize the ultra-high vacuum ( $10^{-10} \div 10^{-11}$  mbar), the cascade of rotary and turbomolecular pump is replaced with an ion pump and a titanium sublimation pump (TSP). These two pumps have no moving mechanical parts and therefore do not transfer vibrations to the microscope structure. Because of that they are particularly suitable to be used during the STM-STS measurements. The ion pump consists of two electrodes set with a potential difference of several kV; the strong electric field between the two plates extracts the electrons from the cathode (field emission effect) and accelerates them towards the anode; in their path electrons may encounter particles of residual gas which can be ionized by impact. The species created are no longer neutral, thus affected by the electric field and accelerated towards the cathode where they settle. TSP belongs to the class of the so-called *getter pumps*, where the vapor of a reactive material, in this case titanium, captures the residual gas molecules in the chamber and places them on a support where they are trapped, becoming inert. The titanium vapor is obtained by the sublimation of a filament which is periodically passed through a current of 45 A.

It should be noted that, in order to achieve these levels of vacuum, the inside walls of the chamber must disrobe any residual of gas: this is possible thanks to a *baking* process in which the whole system is heated to a temperature of about 150-200°C for 60 hours.

Pressure measurement is carried out by a *Bayard-Alpert* ionization gauge. It is based on the principle that the number of free gas molecules present in the chamber is proportional to the pressure: by ionizing them it is possible to generate a detectable current, that gives a measure of the pressure. The deposition chamber does not require special shrewdness due to the presence of vibrations and the pumping system was designed in order to work in a wide pressure regime, from  $10^{-8}$  mbar to  $10^{-2}$  mbar according to the deposition conditions. Its pumping system is just composed of a turbomolecular pump working coupled with a dry pump (scroll pump).

The pumping rate can be controlled by special valves that regulate the gas flux and allow to maintain the desired background pressure in the deposition chamber.

As a final remark, the materials used for the walls of the chamber can be considered: they are made of electro-polished steel resisting to high temperatures, characterized by low rate of desorption at room temperature.

## A.2 STM-STS apparatus

The characterization system used in this work is an Omicron UHV VT-STM microscope. The head of the microscope, whose theoretical principles of operation have been explained in Chapter 1, is housed in a measurement chamber adjacent to the surface preparation one. It is possible to set the voltage applied to the STM tip from values between  $-10$  V and  $10$  V while the sample is connected to ground. The values of the tunneling current range from  $2$  pA to  $333$  nA.

### A.2.1 STM measurements

As mentioned in Section 1.1.1, two operating modes exist for STM: *constant current mode* and *constant height mode*. In the first case, the electronic system detects the tunneling current and controls three piezoelectric actuators (one for each dimension) that modify the tip position in order to maintain constant the tip-sample distance (Figure A.2). The second method exploits the modulation of the tunneling current to trace the sample profile by disabling this feedback loop, so that the tip is kept at fixed absolute height and, in this case, the tunneling current is measured at any point on the surface. In this thesis work the topographic images were acquired in the constant current mode because it allows to obtain a higher resolution, also in the presence of not atomically flat surfaces.



**Figure A.2:** STM sample stage. The tip is placed on top of a cylindrical piezoelectric that allows the scanning of the sample.

The scanning of the area of interest, which can vary from few nanometres up to one square micrometer, is performed by moving the tip along a line in two opposite directions measuring its position on the  $z$ -axis for a finite number of points, typically 300. This operation is repeated for a number of adjacent lines equal to the number

of acquisition points per line, forming a square grid that corresponds to the image (Figure A.3). Moreover, it is possible to vary the scanning angle moving the tip along every direction in the horizontal ( $xy$ ) plane.

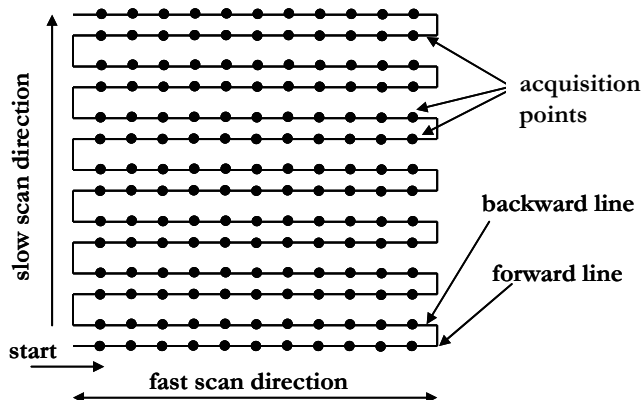


**Figure A.3:** Scheme of tip path during the scanning in the horizontal plane.

The setting of the system is done by a software with a graphic interface reproducing a control panel, which allows to display and modify the parameters involved in the measurement (also for running acquisitions). The most important ones are: the intensity of the tunneling current, the applied voltage between the tip and the sample, the loop gain, the scanner speed and the size of the scan. The correct choice of these parameters is of fundamental importance because they rule several aspects that should be kept under control for a good image acquisition, e.g. the intensity of the tip-surface interaction, the signal to noise ratio and the thermal drift.

The extreme sensitivity of the instrument requires to work in an environment free from mechanical vibrations that can introduce noise, causing variations in the current signal. To overcome this problem, the microscope stage is mounted on a plate almost completely decoupled from the measuring chamber through a damping system consisting of four springs, which maintain the stage suspended inside the chamber and attenuate any external vertical vibration. To ensure stability even on the horizontal plane, the stage is surrounded by a ring of equally spaced copper fins. Between them, small magnets fixed to the walls of the chamber are interposed without direct contact. Any vibration of the suspended stage causes relative motion between the magnets and the copper giving rise to an interaction that prevents the fins vibration and, thus, promotes the system’s mechanical stability. This mechanism can also be disabled by blocking the stage on a suitable support element, e.g. whenever it is necessary to replace the tips, handling specimens or during periods of inactivity of the instrument, in order to avoid the wear of the springs.

Moreover, the apparatus offers the possibility of measurements at different sample temperatures. A special support allows the direct passage of current through the sample, which may be brought to temperatures up to 1500 K. Alternatively, it is possible to reach temperature of 750 K approaching the sample to a resistance in which a current is passed. Conversely, the system cooling is based on the thermal contact between the sample holder and a device called “cold finger”, inside which a stream of helium or liquid nitrogen can flow, depending if the desired minimum temperature is close to 25 K or 90 K.

### A.2.2 STS measurements and lock-in amplifier

As already pointed out in the theoretical discussion on scanning tunneling spectroscopy (STS) (Section 1.2), it is possible to derive information about the electronic structure of the sample through STS and  $dI/dV$  maps. In the employed experimental facility, this task is accomplished by a lock-in amplifier, which applies a modulation to the applied bias between the tip and the sample.

Considering STS measurements, they are obtained on selected positions as follows. First, the tip is positioned on a point of interest on the sample surface; then, the feedback loop on the tunneling current is interrupted and a voltage ramp to the tunneling junction is applied as a function of bias; usually this is a symmetrical voltage ramp with respect to zero whose limits can be chosen by the worker, e.g. in our case ( $-2.5$  V;  $+2.5$  V). This voltage ramp, however, is not continuous, being a digital signal made of equal discrete steps. At each step, after a certain time  $t_{delay}$  necessary to stabilize the system, the tunneling current is acquired as an integral average over a certain acquisition time  $t_{acq}$  useful to lessen the noise. These time intervals can be selected in order to find a good compromise between the need to reduce the noise and the need to have a low measurement time, which allows to minimize drift effects, both thermal and instrumental; a typical value is  $100 \mu\text{s}$  for both. In this way, the  $I(V)$  signal is acquired. The  $dI/dV$  one, instead, is extracted through the lock-in filter: this technique consists in superimposing to the applied bias ( $V_{bias}$ ) a smaller modulated signal ( $V_{mod}$ ), which has a reference frequency  $\omega$  much larger than the cutoff frequency of the dominant pole of the closed loop control system, thus avoiding tip fluctuations at the frequency  $\omega$ :

$$V_{tip} = V_{bias} + V_{mod} \sin(\omega t) \quad (\text{A.2})$$

This produces a tunneling current given by

$$I_{tun} = I + I_{mod} \sin(\omega t + \phi) \quad (\text{A.3})$$

where  $\phi$  is the phase shift introduced by the system. The first term on the right-hand side of the equation ( $I$ ) depends on the fixed tension ( $V_{bias}$ ), while the second one depends on the modulated component. The signal  $I_{tun}$  is sent both to STM electronics, where only the continuous part is revealed, and to the lock-in amplifier. Here the input signal is first filtered, then demodulated through a multiplication with the sinusoidal reference signal, carrying the current component at frequency  $\omega$  in baseband. To obtain the  $dI/dV$  measure the input signal is band-pass filtered at the modulating frequency  $\omega$  and a circuit maximizes the signal to noise ratio resetting the phase shift  $\phi$ . The signal obtained ( $I_{mod}$ ) is converted into a voltage by the low pass filter, which integrates the output signal and divides the result by the integration time, thus obtaining a time average. The signal is amplified and sent to STM electronics and subsequently to the control software.

On the other hand, to obtain  $dI/dV$  maps, the  $dI/dV$  signal is acquired (again with the lock-in amplifier) while the tip is scanning onto the surface in constant current mode. In this way, differential conductance  $xy$  maps ( $dI/dV$  maps) at the imposed bias  $V_{bias}$  are obtained.

In this thesis work a Perkin-Elmer 5209 lock-in amplifier was employed. The reference signal (modulating) can be generated internally or externally. Usually the

first option was preferred and the sinusoidal signal had 30 mV amplitude and frequency of 8 kHz.

### A.3 Tip preparation method

The geometrical features of an ideal tip employed for STM-STS measurements must meet three requirements:

1. low aspect ratio between length and diameter of the body section of the tip; this allows the tip to avoid vibration phenomena during the surface scanning;
2. very high symmetry, which is mandatory in order not to obtain distorted images due to the different tunneling conditions of the tip in the three spatial dimensions;
3. very low apex curvature radius ( $\leq 50$  nm), necessary to obtain a high resolution.

Generally speaking, STM tips are made from thin metal wires (such as tungsten, iridium-palladium, gold or chromium) through several procedures, such as cutting, sputtering, evaporation, electrochemical etching and many others<sup>[77]</sup>. In order to obtain magnetic tips, generally a thin iron or chromium layer (50 ML) is applied to another metal, or a bulk magnetic material is employed<sup>[68]</sup>. For STM-STS measurements reported in this thesis, W and Cr tips have been used.

Regarding the production of W tips, it occurs by means of electrochemical etching in a 2M NaOH solution into which a thin tungsten wire is dipped, which works as anode, positioned in the middle of a gold ring, which works as cathode and which is on the free surface of the solution. This is illustrated in Figure A.4.

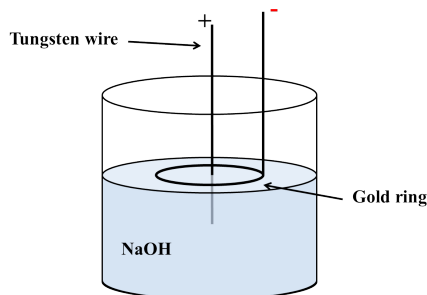
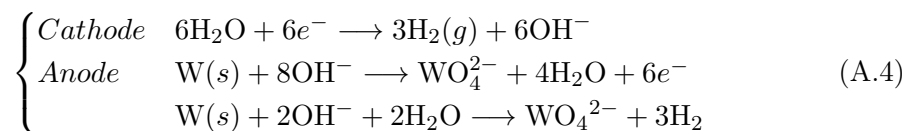


**Figure A.4:** Scheme of a W tip production.

By applying a potential difference (such as 5–6 V), the following reaction occurs:



This process causes an erosion of the W wire in the proximity of the solution's free surface and, after a suitable time, the subsequent detachment of the dipped part (*drop-off*). The latter produces a change in the electrical resistance of the circuit, which stops the current and, thus, the erosion process.

Regarding Cr tips<sup>[68]</sup>, first a rod of polycrystalline Cr with a nearly square cross section is obtained by cutting a 99.99% Cr foil. The etching procedure can be divided

into two steps: in the first, the so-called *pre-etching* (Fig. A.5(a)), a direct current voltage in the 5–7 V range is applied by means of a gold ring, similarly as the previous case, in order to reduce the cross-section; in the second step (Fig. A.5(b)), a voltage in the 3–4 V range is applied until the drop-off is reached. Both NaOH and KOH 1.5 M solutions can be used with satisfactory results.

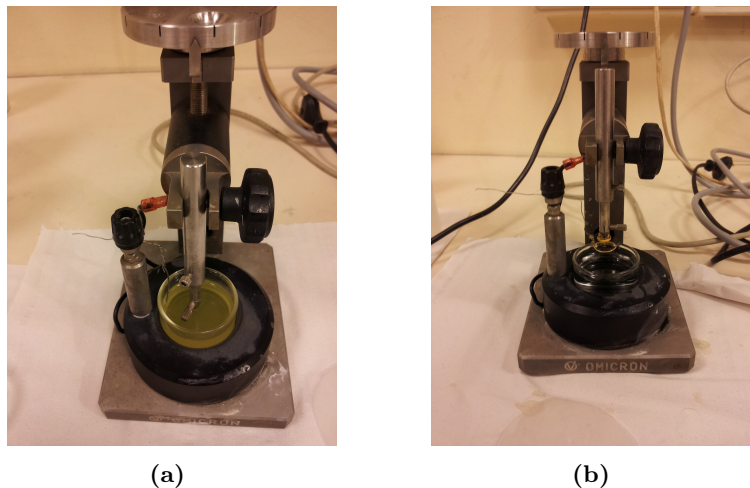


**Figure A.5:** Production of a bulk Cr tip. (a) First step (pre-etching). (b) Second step.

At the end of the etching process, both W or Cr tips must be cleaned from surface impurities, such as NaOH/KOH crystals or oxidized clusters, in an ultrasonic bath, first in distilled water, secondly in isopropyl alcohol. An inspection of the produced tips can be performed with scanning electron microscope (SEM), but during this procedure the tip apex may change, such as by adsorption of an oxide cluster. For this reason, during this measurement some standard techniques to “clean” the tip are periodically adopted, such as the application of a voltage ramp or a series of voltage pulses, in order to promote the detachment of impurities on the tip apex.

## A.4 Surface and sample preparation facilities

The sample preparation is performed into the preparation chamber, communicating with the analysis one. It is possible to transfer the sample from the former to the latter, and *vice versa*, by means of a completely internal system based on a moving transfer rod, which can be driven from the outside by means of a magnet.

The preparation chamber is provided with the following facilities: a sample heater, an ion gun (Fig. A.6(a)), to perform the surface sputtering, and the evaporator (Fig. A.6(b)), for the deposition of a material on a substrate. During the preparation operations the sample is supported by a manipulator, which allows its movement into the three directions ( $x$ ,  $y$  and  $z$ ) and the azimuthal rotation. In addition, a repository system, consisting of a carousel and the aforementioned manipulator, is also present.

The sample heater allows to perform the annealing cycles necessary both for gas desorption (outgassing) and for the reconstruction of the surface structures, e.g. the Au(111) ( $22 \times \sqrt{3}$ ). The heating is possible in two ways: resistive or direct heating. In the first case the increase of temperature (until  $\sim 1000$  K, depending on the sample

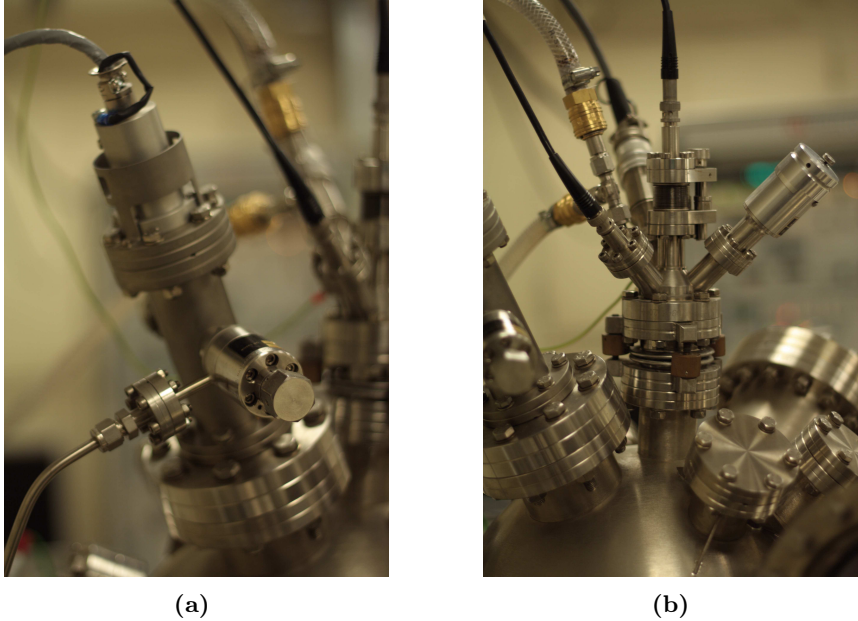


**Figure A.6:** External view of the sample preparation facilities. (a) Ion gun. (b) Thermal evaporator.

material) is reached through an electrical resistance just below the sample, whereas, in the second case, a sample holder allows the direct passage of a current in the sample itself and the consequent heating by Joule effect. In this way it is possible to reach higher temperatures, up to 1500 K.

The ion gun allows to clean the surfaces so that it is possible to re-use the substrates: argon ions ( $\text{Ar}^+$ ) accelerated toward the sample originates the sputtering of the upper surface layer and the removal of the material previously deposited. The Ar gas, coming from an external source, enters in a small cavity where a differential vacuum is created. In this area the gas molecules are ionized by the electrons emitted by a metal filament thanks to the thermoionic effect. The charged molecules speed up thanks to a negative polarized grid and the beam is focused passing through a magnetic field. By regulating the filament current, the magnetic field responsible of the beam deflection and the potential of the grid, it is possible to control the beam shape and the kinetic energy of the ions hitting the sample surface.

The evaporator offers the possibility to deposit many types of materials, such as alloys, metals with low vapor pressure, insulators, thermal and electrical conductors, compounds and pure elements. The evaporating material may be in the form of a rod or it can be contained within a crucible, in case it is not a good electrical conductor. The evaporant is housed in a copper cylindrical shroud (Fig. A.7) and surrounded by a tungsten filament in which a current flows (typically of some mA). Emitted electrons are accelerated by a potential difference of 600–1000 V applied between the filament and the evaporant. The electron bombardment causes a localized temperature increase, and the evaporation of neutral atomic species and ions starts. The beam is addressed towards the substrate with a divergence angle of  $3^\circ$ ; by varying the sample-evaporator distance it is, therefore, possible to control the size of the circular spot on the substrate from 4 to 15 mm diameter. During the deposition process even the evaporator structure

undergoes a rise of temperature and, to avoid the accidental evaporation of copper (contaminating the deposition), the shroud is cooled by a continuous flux of cold water flowing through small capillaries within its walls.



**Figure A.7:** Thermal evaporator, model EFM EVC300. It is visible the copper shroud surrounding the evaporant and the filament.

In the experimental activity presented in this thesis, the Au(111) surface, coming from either a monocrystalline Au sample or Au film deposited on mica, was employed as substrate. The “cleaning” procedure of this surface involves firstly a degas phase, during which the sample temperature is brought up to 800 K, in order to promote the desorption of contaminants. Secondly, an  $\text{Ar}^+$  ions sputtering is carried out, with 1 keV energy and for 15–20 minutes, keeping the sample temperature at 800 K. Finally, in order to promote the surface reconstruction, an annealing step at 850 K for 1 hour is performed. When the cooling sample reaches the room temperature, Ti is deposited by the  $e$ -beam evaporator. The Ti source is a rod with 1 mm diameter and 99.99% purity. During the evaporation, the ionic current is kept constant at 5 nA. Subsequently, in order to obtain the  $\text{TiO}_x/\text{Au}(111)$  sample, oxygen exposure is performed, in our case at room temperature. Oxygen is allowed to enter the preparation chamber with a high-precision valve and it comes from a molecular  $\text{O}_2$  source with an impurity degree of  $1/10^6$ . The sample preparation procedure is explained in detail at the beginning of Chapter 3 (Section 3.1).

## A.5 Low energy electron diffraction (LEED)

The low-energy electron diffraction (LEED) technique makes use, as a probe, of an electron beam of a certain energy incident on the sample surface and it aims to detect the diffracted electrons as spots on a fluorescent screen. Indeed, the diffraction spots visible in the LEED pattern are a representation of the reciprocal space; this means that the distance between adjacent points in the LEED pattern is inversely proportional to the distance between the corresponding points in the direct lattice (which is the real surface unit mesh)<sup>[78]</sup>. In other words, this technique provides information about the surface layers of a material. This is due to the fact that, at low energies (10–100 eV), electrons penetrate only very short distances into the surface, thus their diffraction pattern reflects the atomic spacings in the surface layer<sup>[79]</sup>. The mean free path of electrons in solids for many materials is shown in Figure A.8 and it clearly exhibits a minimum between 50 and 100 eV.

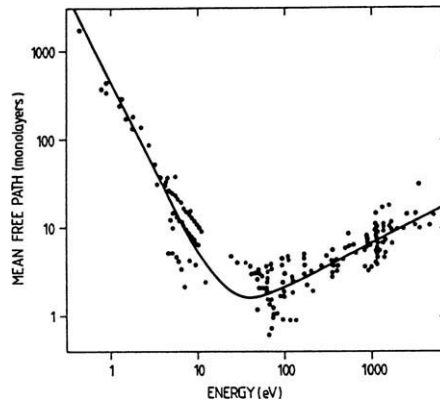


**Figure A.8:** Mean free path of electrons in solids as a function of their energy; a compilation of a variety of experimental data<sup>[80]</sup>.

The LEED apparatus in our laboratory is contained in the preparation chamber and electrons are produced by thermoionic emission from a Ir-Th filament; then, the beam is focused by a series of electrostatic lenses. The measurements are typically performed with a beam current from 0.5 to 1  $\mu\text{A}$ . The electron beam hits the sample's surface and elastically backscattered electrons are detected on a fluorescent screen, on which the diffraction spots appear, which give information about the reciprocal lattice of the surface (as already mentioned). The LEED detector contains three hemispherical concentric grids and a phosphor screen or other position-sensitive detectors. The grids are used for screening out the inelastically scattered electrons. A view of the inner chamber of the LEED instrumentation is shown in Figure A.9.

The ion gun is able to produce an electron beam with primary energy comprised between 5 and 1000 eV. In the measurements reported in this thesis work, the value of about 50 eV was chosen. The action of the lenses can be controlled by varying the voltage between them (from 0 to 1000 V) until an optimum focusing of the diffraction image is obtained. The images, finally, have been acquired by means of a camera.



**Figure A.9:** Inner view of the LEED apparatus.

## A.6 Auger electron spectroscopy (AES)

The Auger electron spectroscopy (AES) is a surface analysis spectroscopic technique able to provide the sample's elemental composition. It employs a high-energy electron beam (about some keV) in order to probe the surface layers ( $\sim 20\text{--}30 \text{ \AA}$ ) of the sample under inspection. This technique is based on the Auger effect: when an atom is excited by a collision with a highly-energetic electron, a core electron (e.g. with energy  $E_1$ ) from that atom can be thrown out, ionizing that core level; this is subsequently filled by an electron from an outer level (e.g.  $E_2$ ). This transition corresponds to an energy  $\Delta E = E_1 - E_2$ , which is transferred to a third electron of the same atom at another level ( $E_3$ ). This electron can reach the vacuum level and escape from the surface of the material thanks to its kinetic energy. If the analyzer is in good contact with the sample holder, that is to say they have the same Fermi energy, the kinetic energy of the Auger electron can be found<sup>[78]</sup>:

$$E_{XYZ} = E_1(Z) - E_2(Z + \delta) - E_3(Z + \delta) - \Phi_A \quad (\text{A.5})$$

where  $Z$  is the atomic number of the element,  $\Phi_A$  is the work function of the analyzer; the Auger transition is labeled with three letters (XYZ) corresponding to the energy levels involved in the process (e.g. KLL); the quantity  $\delta$  (between 0 and 1) is introduced since the electronic levels are shifted towards higher binding energies after the ionization of the atom by the primary electron. Figure A.10 shows a schematic picture of the process.

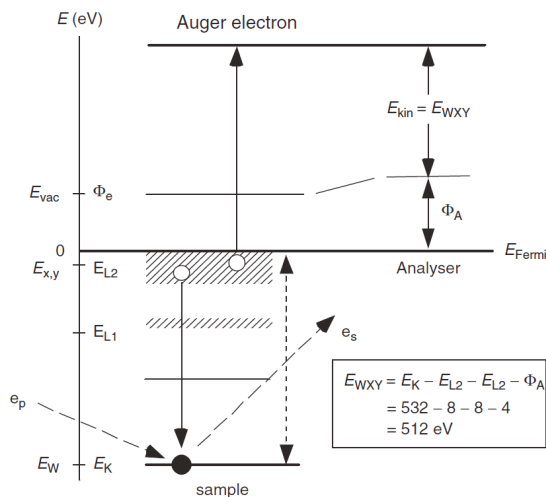


**Figure A.10:** Auger process:  $E_F$  is the Fermi level, while  $\Phi_e$  and  $\Phi_A$  are the work functions of the sample (e) and analyzer (A), respectively<sup>[78]</sup>.

The electron gun employed for the AES in our facility is the same as the one for the LEED instrumentation. However, in this case the electron beam can reach higher energies (typically 3 keV) in order to generate the Auger effect. It should be noted that, nevertheless, this spectroscopic analysis has not been performed in this thesis work and it has been described for a complete highlight of the experimental facilities available in the laboratory.

## Bibliography

- (1) Kubacka, A.; Fernández-García, M.; Colón, G. *Chem. Rev.* **2012**, *112*, 1555–1614.
- (2) Wu, C.-G.; Chao, C.-C.; Kuo, F.-T. *Catal. Today* **2004**, *97*, 103–112.
- (3) Zheng, H. Y.; Qian, H. X.; Zhou, W. *Appl. Surf. Sci.* **2008**, *254*, 2174–2178.
- (4) Grätzel, M. *Nature* **2001**, *414*, 338–344.
- (5) Fujishima, A.; Zhang, X.; Tryk, D. A. *Surf. Sci. Rep.* **2008**, *63*, 515–582.
- (6) Wu, Q.-H.; Fortunelli, A.; Granozzi, G. *Int. Rev. Phys. Chem.* **2009**, *28*, 517–576.
- (7) Sauvage, F.; Di Fonzo, F.; Li Bassi, A.; Casari, C. S.; Russo, V.; Divitini, G.; Ducati, C.; Bottani, C. E.; Comte, P.; Grätzel, M. *Nano Lett.* **2010**, *10*, 2562–2567.
- (8) Freund, H.-J.; Pacchioni, G. *Chem. Soc. Rev.* **2008**, *37*, 2224–2242.
- (9) Diebold, U. *Surf. Sci. Rep.* **2003**, *48*, 53–229.
- (10) Potapenko, D. V.; Osgood, R. M. *Nano Lett.* **2009**, *9*, 2378–2383.
- (11) Biener, J.; Farfan-Arribas, E.; Biener, M.; Friend, C. M.; Madix, R. J. *J. Chem. Phys.* **2005**, *123*, 094705.
- (12) Wu, C.; Marshall, M. S. J.; Castell, M. R. *J. Phys. Chem. C* **2011**, *115*, 8643–8652.
- (13) Tumino, F. “Microscopia e spettroscopia a effetto tunnel di film ultrasottili di titanio e ossido di titanio su Au(111)”, Laurea Specialistica, Politecnico di Milano, 2012.
- (14) Binnig, G.; Rohrer, H.; Gerber, C.; Weibel, E. *Phys. Rev. Lett.* **1982**, *49*, 57–61.
- (15) Michael Schmid *The Scanning Tunneling Microscope*, Institut für Angewandte Physik, [http://www.iap.tuwien.ac.at/www/surface/stm\\_gallery/stm\\_schematic](http://www.iap.tuwien.ac.at/www/surface/stm_gallery/stm_schematic).
- (16) Besenbacher, F. *Rep. Prog. Phys.* **1996**, *59*, 1737.
- (17) Chen, C. J., *Introduction to scanning tunneling microscopy*, 2nd ed.; Oxford University Press: New York, 2008.
- (18) Bardeen, J. *Phys. Rev. Lett.* **1961**, *6*, 57–59.
- (19) Tersoff, J.; Hamann, D. R. *Phys. Rev. Lett.* **1983**, *50*, 1998–2001.
- (20) Tersoff, J.; Hamann, D. R. *Phys. Rev. B* **1985**, *31*, 805–813.
- (21) Chen, C. J. *Phys. Rev. Lett.* **1990**, *65*, 448–451.
- (22) Chen, C. J. *Phys. Rev. B* **1990**, *42*, 8841–8857.
- (23) Ohnishi, S.; Tsukada, M. *Solid State Comm.* **1989**, *71*, 391–394.

- (24) Tsukada, M.; Kobayashi, K.; Ohnishi, S. *J. Vac. Sci. Technol. A* **1990**, *8*, 160–165.
- (25) Tsukada, M.; Kobayashi, K.; Isshiki, N.; Kageshima, H. *Surf. Sci. Rep.* **1991**, *13*, 267–304.
- (26) Doyen, G.; Koetter, E.; Vigneron, J. P.; Scheffler, M. *Appl. Phys. A* **1990**, *51*, 281–288.
- (27) Duke, C. B., *Tunneling in Solids*; Academic Press: 1969.
- (28) Appelbaum, J. A.; Brinkman, W. F. *Phys. Rev.* **1969**, *186*, 464–470.
- (29) Stroschio, J. A.; Feenstra, R. M.; Fein, A. P. *Phys. Rev. Lett.* **1987**, *58*, 1668–1671.
- (30) Ukraintsev, V. A. *Phys. Rev. B* **1996**, *53*, 11176–11185.
- (31) Koslowski, B.; Dietrich, C.; Tschetschetkin, A.; Ziemann, P. *Phys. Rev. B* **2007**, *75*, 035421.
- (32) Passoni, M.; Donati, F.; Li Bassi, A.; Casari, C. S.; Bottani, C. E. *Phys. Rev. B* **2009**, *79*, 045404–1–045404–11.
- (33) Nilius, N. *Surf. Sci. Rep.* **2009**, *64*, 595–659.
- (34) Sebastian, I.; Heiler, M.; Meinel, K.; Neddermeyer, H. *Appl. Phys. A* **1998**, *66*, S525–S528.
- (35) Wöll, C.; Chiang, S.; Wilson, R. J.; Lippel, P. H. *Phys. Rev. B* **1989**, *39*, 7988–7991.
- (36) Harten, U.; Lahee, A. M.; Toennies, J. P.; Wöll, C. *Phys. Rev. Lett.* **1985**, *54*, 2619–2622.
- (37) Barth, J. V.; Brune, H.; Ertl, G.; Behm, R. G. *Phys. Rev. B* **1990**, *42*, 9307–9318.
- (38) Bulou, H.; Goyhenex, C. *Phys. Rev. B* **2002**, *65*, 045407.
- (39) Casari, C. S.; Foglio, S.; Siviero, F.; Li Bassi, A.; Passoni, M.; Bottani, C. E. *Phys. Rev. B* **2009**, *79*, 195402.
- (40) Lüth, H., *Solid Surfaces, Interfaces and Thin Films*, 5th ed.; Springer: 2010.
- (41) Kevan, S. D.; Gaylord, R. H. *Phys. Rev. B* **1987**, *36*, 5809–5818.
- (42) Schouteden, K.; Lievens, P.; Van Haesendonck, C. *Phys. Rev. B* **2009**, *79*, 195409.
- (43) Davis, L. C.; Everson, M. P.; Jaklevic, R. C.; Shen, W. *Phys. Rev. B* **1991**, *43*, 3821–3830.
- (44) Chen, W.; Madhavan, V.; Jamneala, T.; Crommie, M. F. *Phys. Rev. Lett.* **1998**, *80*, 1469–1472.
- (45) Batzill, M.; Katsiev, K.; Gaspar, D. J.; Diebold, U. *Phys. Rev. B* **2002**, *66*, 235401.
- (46) Sakai, Y.; Ehara, S. *Jpn. J. Appl. Phys.* **2000**, *39*, 3789–3792.
- (47) Cao, G.; Wang, Y., *Nanostructures and Nanomaterials: Synthesis, Properties, and Applications*, 2nd ed.; World Scientific: Singapore, 2011.
- (48) Ohring, M., *Materials Science of Thin Films*, 2nd ed.; Academic Press: San Diego, CA, 2001.
- (49) Ibach, H., *Physics of Surfaces and Interfaces*; Springer: 2006.
- (50) Pacchioni, G.; Valeri, S., *Oxide ultrathin films: science and technology*; Wiley-VCH: Weinheim, 2012.
- (51) Wollschläger, J.; Erdös, D.; Goldbach, H.; Höpken, R.; Schröder, K. M. *Thin Solid Films* **2001**, *400*, 1–8.
- (52) Sedona, F.; Rizzi, G. A.; Agnoli, S.; Llabrés i Xamena, F. X.; Papageorgiou, A.; Ostermann, D.; Sambì, M.; Finetti, P.; Schierbaum, K.; Granozzi, G. *J. Phys. Chem. B* **2005**, *109*, 24411–24426.
- (53) Sedona, F.; Agnoli, S.; Granozzi, G. *J. Phys. Chem. B* **2006**, *110*, 15359–15367.
- (54) Barcaro, G.; Agnoli, S.; Sedona, F.; Rizzi, G. A.; Fortunelli, A.; Granozzi, G. *J. Phys. Chem. C* **2009**, *113*, 5721–5729.

- (55) Barcaro, G.; Cavaliere, E.; Artiglia, L.; Sementa, L.; Gavioli, L.; Granozzi, G.; Fortunelli, A. *J. Phys. Chem. C* **2012**, *116*, 13302–13306.
- (56) Barcaro, G.; Sedona, F.; Fortunelli, A.; Granozzi, G. *J. Phys. Chem. C* **2007**, *111*, 6095–6102.
- (57) Surnev, S.; Vitali, L.; Ramsey, M. G.; Netzer, F. P.; Kresse, G.; Hafner, J. *Phys. Rev. B* **2000**, *61*, 13945–13954.
- (58) Kresse, G.; Surnev, S.; Ramsey, M. G.; Netzer, F. P. *Surf. Sci.* **2001**, *492*, 329–344.
- (59) Surnev, S.; Kresse, G.; Sock, M.; Ramsey, M. G.; Netzer, F. P. *Surf. Sci.* **2001**, *495*, 91–106.
- (60) Surnev, S.; Sock, M.; Kresse, G.; Andersen, J. N.; Ramsey, M. G.; Netzer, F. P. *J. Phys. Chem. B* **2003**, *107*, 4777–4785.
- (61) Zhang, L. P.; van Ek, J.; Diebold, U. *Phys. Rev. B* **1998**, *57*, R4285–R4288.
- (62) Zhang, L. P.; van Ek, J.; Diebold, U. *Phys. Rev. B* **1999**, *59*, 5837–5846.
- (63) Potapenko, D. V.; Hrbek, J.; Osgood, R. M. *ACS Nano* **2008**, *2*, 1353–1362.
- (64) Lauwaet, K.; Schouteden, K.; Janssens, E.; Van Haesendonck, C.; Lievens, P. *Phys. Rev. B* **2011**, *83*, 155433.
- (65) Ragazzon, D.; Schaefer, A.; Farstad, M. H.; Walle, L. E.; Palmgren, P.; Borg, A.; Uvdal, P.; Sandell, A. *Surf. Sci.* **2013**, *617*, 211–217.
- (66) Song, Z.; Hrbek, J.; Osgood, R. *Nano Lett.* **2005**, *5*, 1327–1332.
- (67) Carrozzo, P.; Tumino, F.; Passoni, M.; Bottani, C. E.; Casari, C. S.; Li Bassi, A. *Surf. Sci.* **2014**, *619*, 77–82.
- (68) Li Bassi, A.; Casari, C. S.; Cattaneo, D.; Donati, F.; Foglio, S.; Passoni, M.; Bottani, C. E.; Biagioni, P.; Brambilla, A.; Finazzi, M.; Ciccacci, F.; Duò, L. *Appl. Phys. Lett.* **2007**, *91*, 173120.
- (69) Passoni, M.; Bottani, C. E. *Phys. Rev. B* **2007**, *76*, 115404.
- (70) Ramana Murty, M. V.; Curcic, T.; Judy, A.; Cooper, B. H.; Woll, A. R.; Brock, J. D.; Kycia, S.; Headrick, R. L. *Phys. Rev. B* **1999**, *60*, 16956–16964.
- (71) Hommrich, J.; Hümann, S.; Wandelt, K. *Faraday Discuss.* **2002**, *121*, 129–138.
- (72) Schoiswohl, J.; Sock, M.; Eck, S.; Surnev, S.; Ramsey, M. G.; Netzer, F. P.; Kresse, G. *Phys. Rev. B* **2004**, *69*, 155403.
- (73) Schoiswohl, J.; Surnev, S.; Sock, M.; Eck, S.; Ramsey, M. G.; Netzer, F. P.; Kresse, G. *Phys. Rev. B* **2005**, *71*, 165437.
- (74) Ulrich, S.; Nilus, N.; Freund, H.-J.; Martinez, U.; Giordano, L.; Pacchioni, G. *Chem. Phys. Chem.* **2008**, *9*, 1367–1370.
- (75) Ulrich, S.; Nilus, N.; Freund, H.-J.; Martinez, U.; Giordano, L.; Pacchioni, G. *Surf. Sci.* **2009**, *603*, 1145–1149.
- (76) Netzer, F. P. *Surf. Rev. Lett.* **2002**, *09*, 1553–1563.
- (77) Melmed, A. J. *J. Vac. Sci. Technol., B* **1991**, *9*, 601–608.
- (78) Vickerman, J. C.; Gilmore, I., *Surface Analysis: The Principal Techniques*, 2nd ed.; John Wiley & Sons: 2011.
- (79) Poole, C. P. J.; Owens, F. J., *Introduction to Nanotechnology*; John Wiley & Sons: 2003.
- (80) Seah, M. P.; Dench, W. A. *Surf. Interface Anal.* **1979**, *1*, 2–11.

# Ringraziamenti

Sono molte le persone che vorrei ringraziare concludendo questo lavoro di tesi. Prima di tutto (e di tutti), la mia famiglia; ai miei genitori, grazie per tutto ciò che mi avete dato, per il vostro supporto, per i valori che mi avete trasmesso e per il vostro affetto incondizionato; a mio fratello Carlo, grazie per le discussioni con te, sempre interessanti e divertenti, e per tutto ciò che condividiamo. Anche tu hai intrapreso un percorso scientifico (in realtà, più del mio) e stai raggiungendo (ma soprattutto raggiungerai) dei traguardi importanti. Sono fiero di te. Il ringraziamento va esteso a tutti i miei familiari in senso generale, vicini e lontani; grazie per il vostro affetto e per avermi sempre fatto sentire parte di una grande famiglia serena.

Un grande ringraziamento spetta al Prof. Andrea Li Bassi, che non solo mi ha consentito di svolgere questo lavoro di tesi, ma mi ha sempre consigliato e aiutato per compierlo al meglio, con grande disponibilità, competenza e simpatia. Ringrazio ovviamente Paolo, che ha appena concluso il suo dottorato: fin da subito sei stato non solo un semplice “tutor”, ma un amico; grazie per tutti i tuoi consigli, il tuo aiuto, la tua allegria e la tua buona cucina! Grazie anche a Francesco, che si è dimostrato fin da subito un collega amichevole, pronto a rispondere a tutte le mie domande (basta che non gli si chieda che giorno è). Voglio ringraziare, poi, tutto il personale del CesNEF: i Dott.ri Carlo Casari e Matteo Passoni, per aver supportato la mia attività di tesi in maniera meno diretta ma non meno significativa; i Proff. Carlo Bottani e Marco Beghi, per essere dei docenti esemplari, capaci di creare interesse e curiosità per ciò che spiegano; tutti i ragazzi che lavorano (o hanno lavorato) come assegnisti o dottorandi in questo gruppo di ricerca, i quali hanno reso più leggere le lunghe giornate in laboratorio: Alessandro (Zani), Alessandro (“Maffo”), Andrea (“Andreino”), Andrea (“Usel”), Edoardo, Lorenzo, Paolo (“Budoni”), Piero; infine, la Dott.ssa Anna Facibeni, Antonio Mantegazza, il Dott. David Dellasega e la Dott.ssa Valeria Russo, che si sono sempre dimostrati gentili e socievoli pur non collaborando direttamente con me.

Ritengo giusto dare un po’ di spazio a tutte le maestre, professoresse e professori che in tutti questi anni mi hanno insegnato qualcosa e hanno svolto il loro lavoro con grande passione. Queste persone non hanno solo contribuito alla mia crescita intellettuale, dandomi gli strumenti per arrivare fino a qui, ma mi hanno anche dato un esempio positivo.

Ringrazio anche le persone che, in modo indiretto, hanno contribuito alla scrittura di questa tesi; in particolare, chi ha lavorato (come tesista o dottorando) nel laboratorio dell'STM prima di me e chi ha scritto le varie guide a L<sup>A</sup>T<sub>E</sub>X che ho consultato.

Voglio ringraziare le persone che hanno frequentato con me questi cinque anni di università; a tutti voi, grazie per la vostra compagnia nelle lunghe giornate di lezione e in bocca al lupo per il vostro futuro; in particolare, spero che l'amicizia maturata con alcune di queste persone (Federico "Regi", Federico "Pulvi", Roberta e Novella) possa perdurare a lungo, anche ora che le nostre strade iniziano a prendere direzioni diverse.

Questa tesi ha richiesto un grande lavoro e una grande dedizione, vale a dire, tanto tempo; ringrazio, quindi, i miei amici, che mi sono stati vicini benché il mio tempo per loro fosse spesso limitato. Voglio menzionare, in particolare: Andrea, che condivide con me l'interesse per i motori e molte altre cose (principalmente degne di un vero "turbo-nerd"); Francesca, che, nonostante la distanza inter-continentale, non si sottrae mai a un parere tennistico o musicale e si tiene informata su come vanno le cose; Luca, che è mio amico da una vita e, tra l'altro, ha realizzato un semplice programma risparmiandomi qualche ora di lavoro nell'analisi dati; Silvio, degnissimo interlocutore in discussioni più o meno scientifiche e, soprattutto, degno avversario o alleato nelle epiche partite ad Halo.

Come ringraziamento finale, non potrei non menzionare Martina (a proposito di persone che avrebbero passato volentieri più tempo con me); il tuo affetto, la tua stima per me e la tua dolcezza fuori dal comune mi hanno incoraggiato e reso più sereno. Grazie di cuore.